Properties of undoped and doped spin-$\frac{1}{2}$ ladders at finite temperature

Continuous unitary transformation combined with
a mean field approach and
inelastic neutron scattering results for the cuprate family

Dissertation
zur Erlangung des Grades eines
Doktors der Naturwissenschaften

Der Fakultät Physik
der Technischen Universität Dortmund
vorgelegt von

Isabelle Désirée Exius
aus Dortmund

November 2010

Tag der mündlichen Prüfung: 03.12.2010

Vorsitzender: Prof. Dr. B. Spaan
Erster Gutachter: Prof. Dr. G. Uhrig
Zweiter Gutachter: Prof. Dr. A. Tennant

Meinen Eltern, Annegret und Dieter Exius

Contents

Abstract

Antiferromagnetic spin-$\frac{1}{2}$ ladders have been studied in theoretical and experimental physics for several years. The spin ladder is a good model to bridge between theory and experiment, because it is realized in the copper oxide family $Sr_{14-x}(La,Ca)_x Cu_{24}O_{41}$. These copper oxides consist of alternating layers of edge-sharing chains and ladders. The insulating mother compound $Sr_{14}Cu_{24}O_{41}$ is hole doped in the chains as well as slightly in the ladders. The hole content in the $Sr_{14}Cu_{24}O_{41}$ ladders is reduced, if La^{3+} is substituted for Sr^{2+} resulting in a pure antiferromagnetic spin ladder given by $La_4 Sr_{10}Cu_{24}O_{41}$.

In this thesis such spin ladders are studied by an amalgamated approach of theoretical work and experiments. For the $La_4 Sr_{10}Cu_{24}O_{41}$ ladder the temperature development is investigated using scattering techniques as well as computer modelling. At zero temperature the spin ladder has already been well described by effective models computed via perturbative continuous unitary transformations (PCUTs). These PCUT results are now combined with a mean field approach allowing for incorporation of temperature induced conditional excitations via vertex corrections. The vertex correction results in a decreasing one-triplon spectral weight upon increasing temperature. This effect is studied by inelastic neutron scattering (INS) on $La_4 Sr_{10}Cu_{24}O_{41}$ crystals by measuring the scattering amplitude at various temperatures. Convincing agreement is found within the experimental and theoretical error bars. Additionally the coupling constants found in Ref. [1] could be confirmed.

The importance of an inter-ladder coupling J_{inter} between isolated ladders in the plane is investigated by combination of the PCUT with a mean field approach. This calculation is undertaken for the square and the trellis lattice. The difference to the existing calculations [2], [3] and [4] is the partial inclusion of the hardcore interaction for neighbouring

ladders. At zero temperature we reveal the effect of quantum fluctuations on the spin gap. In the case of the square lattice we find the closure of the spin gap at a critical inter-ladder coupling enlarged by $3 - 4\%$. In the case of the trellis lattice, the spin gap decreases also as a function of inter-ladder coupling. In this case we find an enlarged critical inter-ladder coupling up to 21%. In additon, the theoretically predicted shift of the spectral weight by Uhrig and Schmidt could experimentally be confirmed.

Substituting Ca^{2+} for Sr^{2+} results in hole doped ladders, such as $Sr_{2.5}Ca_{11.5}Cu_{24}O_{41}$ and $Sr_8Ca_6Cu_{24}O_{41}$, where the hole doping depends on the substituted Ca^{2+} content. The magnetic spectra of these two doped ladders are measured by INS and compared with the undoped ladder $La_4Sr_{10}Cu_{24}O_{41}$. The comparison reveals new features tracing back to the presence of holes. At low temperature in both compounds scattering below the gap of the undoped ladder is found resulting in a subgap[1] state at about 8meV. The subgap broadens at high temperature so much that the closing of the subgap results. Additionally for both dopings and at low and high temperature a hole-pair captured by triplons is found with a fixed energy gap at 23meV. The new features are qualitatively explained in terms of resonant valence bond theory (RVB) as well as stripe ordering theory.

---

[1]The term *subgap* is commonly used by experimentalists.

Chapter 1

Introduction to high T_c superconductors

In 1911 Heike Kamerlingh Onnes discovered the superconducting phase in Mercury cooled to the temperature of liquid Helium. Two years later, in 1913 he received the *Nobel* prize for his

investigations on the properties of matter at low temperatures which led, inter alia, to the production of liquid helium [5].

The key features of superconductivity are the sudden disappearing resistence of electric current below a critical temperature and the Meissner-Ochsenfeld effect. Conventional low temperature superconductors are rather conventional metals at high temperatures. The superconducting phase in metals is well understood by the BCS-theory developed by John Bardeen, Leon N. Cooper und John R. Schrieffer in 1957. Within BCS theory the superconducting phase is induced by an attractive electron-electron interaction mediated by a phonon between states of opposite spin and momentum k resulting in the formation of a so called *Cooper pair*. The Cooper pairs are spin-zero bound states of two electrons. A fluid of delocalized Cooper pairs forms the basis of superconductivity [6].

The mechanism behind high-temperature superconductivity in cuprates is still a challenging open question. In 1986 Bednorz and Müller discovered a superconducting

phase in $La_{5-x}Ba_xCu_5O_{5(3-y)}$ [7]. A few month later it was found that doping with Sr instead of Ba raised the superconducting critical temperature [8]. The high T_c materials were in striking contrast to conventional superconductors as they were derived from the hole doping of insulators and were relatively bad conductors above the superconducting temperature with anomalous thermal properties. For cuprates a maximal critical temperature of up to 145K occurs upon hole doping [6], making the cuprates interesting for technical applications.

1.1 Key features of high T_c superconductors

The characteristic structural element of high T_c superconducting cuprates are layers of CuO_2 [9]. These layers are believed to play an important role for the understanding of superconductivity in two dimensional high T_c superconductors.

The crystal structure suggests that the Cu^{2+} atoms are in $S = \frac{1}{2}$ states, that strongly hybridize with the surrounding p-levels of the oxygen atoms. The configuration of Cu-O-Cu bonds determines the structure of the cuprate [9]. In high T_c superconducting cuprates the Cu-O-Cu bonds possess an angle of $180°$. These bonds are mutually orthogonal forming a square lattice layer as sketched in Fig. 1.1.1. The insulating parent compound of two dimensional high T_c superconducting cuprates is La_2CuO_4 [9]. It is an example of a planar spin-$\frac{1}{2}$ Heisenberg antiferromagnet with isotropic and predominantly nearest neighbor coupling [8] with very high exchange energy [10]. This model predicts a constant but finite spin-spin correlation with increasing spin distance. The non zero spin-spin correlation indicates the established antiferromagnetic long ranged order in this spin system [11]. In contrast to band theory calculations experimental investigations show that the parent compound La_2CuO_4 is insulating, though the Cu atoms possess a single electron in the d-shell. Such insulating materials are called Mott-insulators. Hole doping causes the compound to become superconducting. It is believed, that the additional charges introduced upon doping pair with the single d-electrons to superconducting cooper pairs.

1.2 Phase diagram for a doped high T_c-superconductor

When La_2CuO_4 is doped for example with Sr a rich phase diagram is found [8]. Such
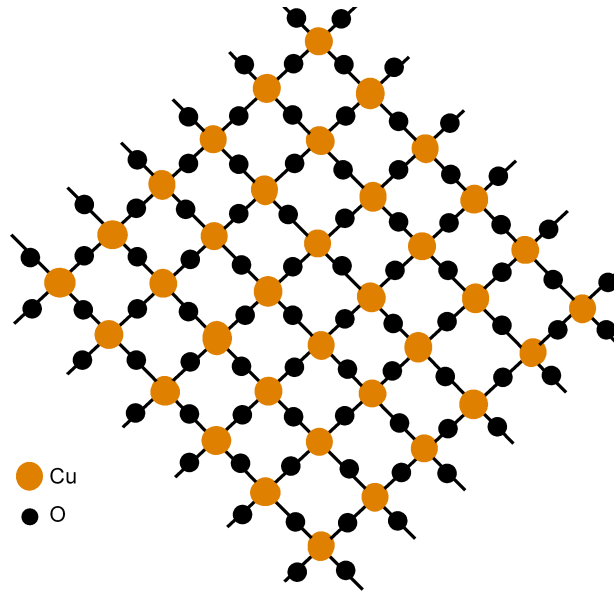
Figure 1.1.1: Bond configuration in a single CuO_2 layer of two dimensional high-temperature superconducting cuprates such as La_2CuO_4. The $180°$ Cu-O-Cu bond configurations are mutually orthogonal resulting in a square lattice layer.

a phase diagram of a hole doped high T_c-superconductor is presented in Fig. 1.2.1. The phases are sketched as a function of temperature T and doping level δ. At very low doping the antiferromagnetic (AF) phase is dominant from low to high temperatures. The superconducting phase (SC) is found for dopings $0.05 \lesssim \delta \lesssim 0.25$ at low temperature. Optimal doping δ_{op} is given when the critical temperature becomes maximal. The regimes below δ_{op} is the underdoped and above δ_{op} the overdoped regime. At low temperatures the AF and SC regimes are bridged by the spin glass regime (SG), where magnetism survives locally and superconductivity is not established yet. Furthermore there are the pseudogap PG, the non-Fermi-liquid NFL and the Fermi-liquid FL regimes, that are not separated from each another by phase transitions but by crossovers indicated by the dotted lines in Fig. 1.2.1.

1.3 Theoretical descriptions

A full theoretical description of high T_c superconductors is not achieved, yet. However, there are two candidates of theoretical description that allow for identifying some fea-
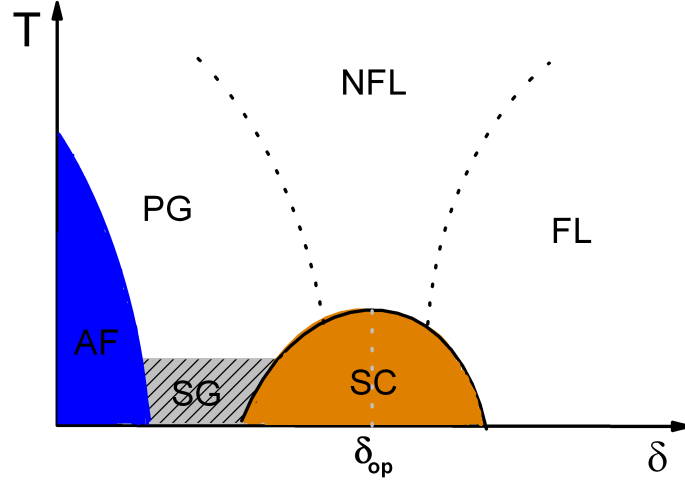
Figure 1.2.1: Schematic phase diagram showing the typical phases of a hole-doped T_c-superconductor in dependence of temperature T and doping level δ. The true phases showing a phase transition are the antiferromagnetic phase AF and the superconducting dome (SC). At low temperatures both are bridged by the spin glass regime (SG) representing a phase with local magnetism and a not yet established superconductivity. Optimal doping δ_{op} is reached at the maximum critical temperature T_c. The system is underdoped below δ_{op} and overdoped above δ_{op}. The dotted lines indicate the crossover (not the phase transitions) between the other regimes, that are the pseudogap PG, the non-Fermi-liquid NFL and the Fermi-liquid FL regime.

tures of high T_c materials measured in experiments.

In 1973 Anderson introduced the so called *resonating valence bond* (RVB) state based upon the idea that pairs of electrons, occupying bonds between adjacent lattice sites i in a crystal are able to carry out (partially) unsynchronized resonances. The RVB state is a mixture of singlet pairings of electrons in a specific way [12]. It is a precise singlet without long range order [12]. The ground state is given by the product of such RVB states, which is a fluid in that it has quantum transport of spin excitation [12]. Doping of La_2CuO_4 in the RVB state results in boson hole exciations [12], where the holes in the RVB state are almost free.

A realistic theoretical approach was undertaken by Kotliar et al. They combined the local density approximation with the dynamical mean-field theory (LDA+DMFT) to study intermediate energy properties of $La_{2-x}Sr_xCuO_4$ [13]. Kotliar et al. find convincing quantitative agreement with optical conductivity measurements supporting the view that the hole doped cuprates are above but not very far from the metal charge-transfer

insulator transition [13].

In another approach the holes are believed to self-organize into *stripes* that alternate with antiferromagnetic (insulating) regions within copper oxide planes [14, 3]. This situation is described by the so called *Luther - Emery* [15] model which describes one-dimensional fermions with gapless charge and gapped spin degrees of freedom [16]. This model applies to one-dimensional Mott insulators or superconductors because they are characterized by such a gapless and a gapped degree of freedom [16]. For example Vojta and Ulbricht computed spin excitation spectra in a bond centered stripe state with long range magnetic order using a two dimensional spin-only model [17]. They employed a bond operator formalism, that captures dimerization and broken spin symmetry. Their results on stripe ordering describe well the neutron scattering data on $La_{1.875}Sr_{0.125}CuO_4$ measured by Tranquada et al. [18].

1.4 Relation to ladder systems

In the stripe model the coupling between the two antiferromagnetic regions in a hole doped CuO_2 layer is weakened by the stripes of holes in-between. Thus the two dimensional hole doped high T_c superconductors are related to the one dimensional two-leg ladder systems.

Many members of the lanthanum cuprate family of high-temperature superconductors exhibit strong singularities in the doping dependence of various interesting low-temperature properties at $\delta = \frac{1}{8}$; together, these phenomena are referred to as the $\frac{1}{8}$ *anomaly* [14]. For example, in $La_{2-x}Ba_xCuO_4$ and $La_{1.62-x}Nd_{0.4}Sr_xCuO_4$, there is a deep minimum in $T_c(\delta)$; further common properties are summarized in Ref. [14]. Following the discovery of stripe order in $La_{1.62-x}Nd_{0.4}Sr_xCuO_4$ by Tranquada et al. [18] this $\frac{1}{8}$ anomaly is associated with stripe ordering [14].

A two-leg spin ladder is antiferromagnetic because of the superexchange J between neighbouring spins [18]. However, there is no static order at any temperature. This fluctuating, correlated state is said to be quantum disordered [18]. Furthermore, the spin ladder exhibits an energy gap from the ground state to the first excited state, which is of the order of the coupling J. The dispersion of this excitation is mainly directed along the ladder, making it possible to regard the spin ladder as one dimensional. Besides the possible theoretical derivation of the 1D two-leg spin ladder from the 2D CuO_2 layer by stripe order considerations, spin ladders are realized in some cuprates as described
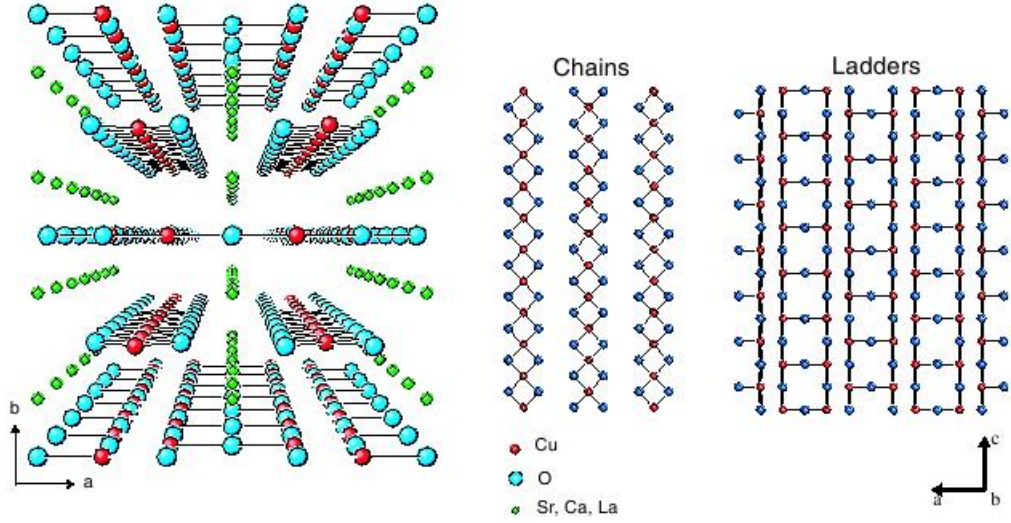
Figure 1.5.1: The structure (left) of the cuprate family $Sr_{14-x}(La,Ca)_xCu_{24}O_{41}$ (taken from [19]). These cuprates consist of alternating layers of edge-sharing chains (middle) and ladders (right). The intra-chain and intra-ladder couplings are presented by the black solid lines. Layers of the constituents (Sr^{2+}, La^{3+}, Ca^{2+}) alternate with the chain and the ladder layers.

below.

1.5   Ladder cuprates

The parent compound of the ladder copper oxide family investigated within this work is $Sr_{14}Cu_{24}O_{41}$. It is an insulator. Substitution of Sr^{2+} for La^{3+} or Ca^{2+} enlarges the family members to $(La,Ca)_xSr_{14-x}Cu_{24}O_{41}$.

A schematic view of the structure of these cuprates (also called the telephone number compounds because of their stoichiometry) is depicted in Fig. 1.5.1 (taken from Ref. [19]). The ladder cuprates are composed of alternating planes of edge-sharing CuO_2 chains and planes of weakly coupled Cu_2O_3 spin ladders, where the copper Cu and oxygen O atoms form a square lattice. Both substructures are orientated along the crystallographic c-axis. The planes are separated from each other by the constituents (Sr^{2+}, La^{3+}, Ca^{2+}).

In these cuprates the spins $\frac{1}{2}$ are again given by the unpaired electrons in the planar $3d_{x^2-y^2}$ orbitals of the Cu atoms. Hybridisation of the $2p_x$ or $2p_y$ oxygen orbitals with

the $3d_{x^2-y^2}$ Cu orbitals allows for the superexchange [20]. While the coupling within the ladder is strong due to the angle of $180°$, the coupling between two ladders is much weaker because the superexchange via the Cu-O-Cu path is significantly decreased for an angle of $90°$ [20, 21]. Furthermore, the inter-ladder coupling in the plane is highly frustrated, because neighbouring ladders are displaced by $\frac{c}{2}$, so that each spin on a rung of a ladder is coupled to both adjacent spins of the left or the right neighboring ladder equally, which in turn are coupled antiferromagnetically with the second spin on the left and right rung respectively. This fact causes the system to be more or less one dimensional along the ladder direction and justifies the treatment of isolated spin ladders in these cuprates [4].

The parent compound $Sr_{14}Cu_{24}O_{41}$ is intrinsically hole doped in both the chains and the ladders with six holes per unit cell in total. Data from X-ray absorption spectroscopy show, however, that the holes are mainly located in the chains (on average 5.2 holes per unit cell) resulting in an only very slightly doped ladder (on average 0.6 holes per unit cell) [22, 23]. This result is explained by the higher electronegativity in the chains [24]. Substituting La^{3+} for Sr^{2+} reduces the total number of holes in the system, so that $La_4Sr_{10}Cu_{24}O_{41}$ represents a spin ladder with nearly no holes. The remaining holes reside in the chains. The compound $La_6Sr_8Cu_{24}O_{41}$ has no holes at all. In the compounds $La_xSr_{14-x}Cu_{24}O_{41}$ with $x \geqslant 1$ the holes reside exclusively on chains [25]. A substitution with an equivalent constituent such as Ca^{2+} leaves the number of holes in the system constant, but it results in the transfer of holes from the chains to the ladders due to the smaller ionic radius of Ca^{2+} [26, 24]. Compounds containing hole doped ladders can exhibit a superconducting phase below a critical temperature and when pressurized. This is the case for $Sr_{2.5}Ca_{11.5}Cu_{24}O_{41}$ [27].

1.6 Purpose of this work

The purpose of this work is to study the ladder substructure within the ladder cuprates both theoretically and experimentally. Spin ladder calculations have been done using different methods, among them are the method of continuous unitary transformation [28, 29, 30] and mean field theory [31, 32]. These calculations concentrate on zero temperature. However, the phase diagram discussed suggests an interesting temperature dependence of magnetic excitations of hole doped superconductors and therefore

on the chains and ladders. Further, experimental validations require an appropriate consideration of temperature effects. Hence, for the undoped spin ladder $La_4Sr_{10}Cu_{24}O_{41}$ a theory at finite temperature is developed.

On the theoretical side an efficient Hamiltonian for the ladder is determined from perturbated continuous unitary transformations (PCUT) [33, 34]. As usual in this theory, the obtained transformations allow physical quantities to be determined in an effective fashion such as the dynamical structure factor. In this thesis the PCUT method is combined with a mean field approach, that considers the hardcore feature of the excitations. From that, the contribution of the conditional one-triplon excitation due to thermal fluctuations to the one-triplon weight for finite temperatures is deduced. It is shown, that the one triplon spectral weight diminishes with increasing temperature affecting directly the dynamical structure factor.

On the experimental side, neutron scattering experiments have been undertaken on different members of the ladder cuprate family described above. INS experiments were performed at different temperatures revealing the intensity decrease of the dynamical structure factor with increasing temperature. Convincing agreement is found for $La_4Sr_{10}Cu_{24}O_{41}$ between theory and experiment.

Though the interladder coupling is weak its influence has to be accounted for within a certain level of accuracy. Several methods have been used for investigation of the inter-ladder coupling of such systems [35, 36, 37, 38]. Calculations using PCUTS have been done in Refs. [2, 3, 4], where the hardcore constraint along the neighboring ladders is neglected. Within this work the significance of the inter-ladder coupling for the square and the trellis lattice is studied including the hardcore feature partially in the calculations. As for the temperature treatment for the isolated ladder, the inter-ladder coupling is also carried out on the mean field level. At zero temperature we find that the closing of the gap is only slightly affected by quantum fluctuations for the square lattice. For the trellis lattice the closing of the spin gap is stronger affected resulting in an enlarged critical inter-ladder coupling. For the trellis lattice, which is relevant for the compounds employed in the experiments, the shift in the dispersion along q_l reported in Ref. [4] is compared with the experimental results.

Finally we investigate the influence of hole doping at different temperatures on the magnetic spectrum for the doped ladders $Sr_8Ca_6Cu_{24}O_{41}$ and $Sr_{2.5}Ca_{11.5}Cu_{24}O_{41}$. The

spectrum of the undoped ladder $La_4Sr_{10}Cu_{24}O_{41}$ is used as a reference in order to conclude, which features arise from the presence of holes. The features of the hole doped ladders can be qualitatively explained with resonating valence bond theory RVB [39] or with stripe formation [15, 16]. Similarities to ARPES [40, 41] measurements on $Sr_{2.5}Ca_{11.5}Cu_{24}O_{41}$ and to an INS measurement [42] are found.

1.7 Set-up of this work

Profiting from synergies of both theoretical and experimental work this thesis is organized as follows: In Chapter 2 the experimental set-up for inelastic neutron scattering (INS) is described. To this end the most important quantities concerning scattering theory such as the partial differential scattering cross section are introduced in Chapter 2. This quantity is measured directly in an inelastic neutron scattering experiment. The complete set-up of such an experiment is also presented in Chapter 2, starting from the production of neutrons up to the detection of the scattered neutrons.

To build a bridge between notions predominantly employed by theorists and experimentalists, a brief introduction to the different terms for magnetic excitations is given in Chapter 3 explaining the differences of notions such as *magnons* and *triplons*.

Then the theoretical methods, such as PCUT and mean field theory, used within this thesis to calculate the physical quantities of interest are introduced briefly in Chapter 4. The temperature influence on the dynamical structure factor for the isolated spin ladder is presented in Chapter 5 as well as the comparison to an INS experiment.

The coupling of such isolated spin ladders is the topic of investigation in Chapter 6, where both the square lattice and the trellis lattice, which are realistic to cuprates, are taken into account. The zero temperature limit of the inter-ladder coupling is discussed, as well as the finite temperature behavior.

Chapter 7 contains purely experimental results giving new insight in the magnetic spectra of doped spin ladders $Sr_{2.5}Ca_{11.5}Cu_{24}O_{41}$ and $Sr_8Ca_6Cu_{24}O_{41}$. A comparison to the spectrum of the undoped ladder $La_4Sr_{10}Cu_{24}O_{41}$ shows new features that trace back to the presence of holes.

Conclusions of this thesis and an outlook to future work are given in Chapter 8.

Chapter 2

Introduction to neutron scattering

Neutron scattering is a powerful and versatile technique for investigations in condensed matter science. The de Broglie wavelength of thermal neutrons is comparable to the interatomic length in solids, and therefore neutrons will be diffracted by crystals. The two most important features of the neutron are the zero net charge and its magnetic moment.

Due to its zero net charge there is no Coulomb potential to overcome, and hence, it interacts only weakly with matter permitting a deep penetration into the sample. This particularily allows for a direct interaction with the nucleus of an atom. The interaction, however, of a neutron and a nucleus is known to be of very short range ($\sim 10^{-13}$cm $=$ 1fm). Since this length is much smaller than the neutrons' de Broglie wavelength the interaction between a neutron and a nucleus can be considered nearly pointlike.

The neutrons' second feature, its magnetic moment, facilitates an interaction with the unpaired electron spins in magnetic atoms and offers therefore to gain information on distributions of magnetic moments. The energy of thermal neutrons is of the same order as the excitation energies in magnetic systems.

Hence the neutron is a powerful probe to investigate both the nuclear and magnetic structure and the dynamics of the solid state systems.

2.1   The scattering cross-section

In this section the most important properties and formulas concerning neutron scattering will briefly be summarized. Neutron scattering is elaborated in detail by many authors

including Squires [43], Lovesey [44] and Shirane et al. [45].

In a neutron scattering experiment incident neutrons with wave vector **k** and energy E are scattered by the sample at an angle θ with a wave vector **k'** and energy E' as it is illustrated in Fig. 2.1.1. The scattered neutrons are collected with angular resolution in a distance d by the detector.

  If energy is transferred by the scattering process, whether from the neutron to the
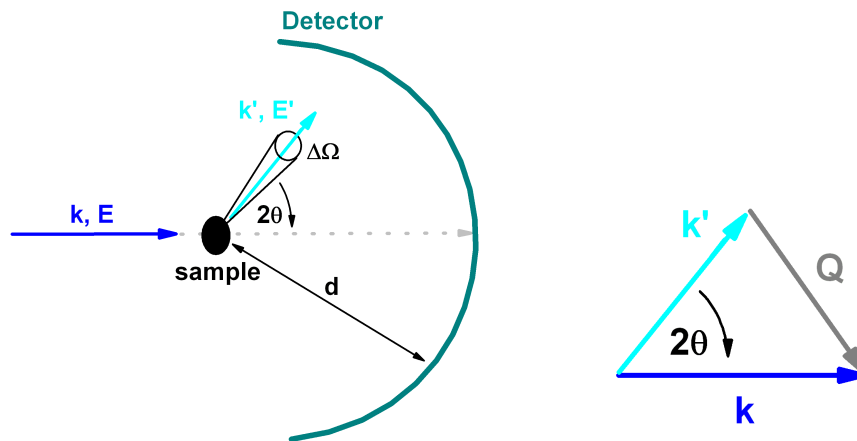
Figure 2.1.1: a) Sketch of a scattering process. An incoming neutron with wave vector **k** and energy E is scattered by the sample at an angle 2θ resulting in a neutron with wave vector **k'** and energy E'. The scattered neutrons **k'** are detected at an angle of 2θ by the detector at a distance d. b) The scattering triangle reveals the meaning of the wave vector transfer **Q**. It is the difference between the incomming **k** and the scattered **k'** wave vector.

sample or from the sample to the neutron, the neutron energy is changed by

$$\hbar\omega = E - E' = \frac{\hbar^2 (\mathbf{k}^2 - \mathbf{k'}^2)}{2m}, \tag{2.1.1}$$

where m is the neutron mass, ω the angular frequency and $\hbar$ the Planck constant divided by 2π. If energy is absorbed by the the sample, $\hbar\omega$ will be positive, and if energy is absorbed by the neutron, $\hbar\omega$ will be negative. The change in momentum is given by the wave vector transfer **Q**, illustrated in the scattering triangle in Fig. 2.1.1(b). It is calculated by

$$\mathbf{Q} = \mathbf{k} - \mathbf{k'}. \tag{2.1.2}$$

In the case of *elastic* scattering, there is no energy transfer, so that $\hbar\omega = 0$ holds, yielding $|\mathbf{k}| = |\mathbf{k'}|$. However the direction between $\mathbf{k}$ and $\mathbf{k'}$ can be changed resulting in a wave vector transfer $\mathbf{Q}$ only dependent on the scattering angle θ. In the case of *inelastic* scattering, there is energy transfer with $\hbar\omega \neq 0$.

Considering a monoenergetic beam of neutrons with the wave vector dependent flux $\varphi(\mathbf{k}_i)$ hitting a target, the rate at which the neutrons are scattered is defined by the product of the initial neutron flux $\varphi(\mathbf{k}_i)$ times a quantity known as the cross section σ. The cross section itself gives the total number of neutrons scattered per second divided by the neutron flux $\varphi(\mathbf{k}_i)$. The intensity I of neutrons scattered at a certain solid angle $\Delta\Omega$ with a final energy between E' and $E' + \Delta E'$ is related to the neutron flux $\varphi(\mathbf{k}_i)$ by the *partial differential cross section* $\frac{d^2\sigma}{d\Omega dE'}$ according to

$$I = \varphi(\mathbf{k}_i) \left(\frac{\mathrm{d}^2\sigma}{\mathrm{d}\Omega \mathrm{d}E'} \right) \Delta\Omega\Delta E'. \tag{2.1.3}$$

The *partial differential cross section* is a measure of the number of neutrons scattered per second into a solid angle $\Delta\Omega$ with a final energy between E' and $E' + \Delta E'$ divided by the flux, the range of scattered energy and the solid angle. The *partial differential cross section* is the quantity measured directly in an inelastic neutron scattering experiment. Therefore it will be derived in detail.

2.1.1 Partial differential cross section

The neutron interacts with condensed matter either by scattering via the nuclear force or via its magnetic moment interacting with other magnetic moments present in the material. As mentioned in the introduction this is a consequence of its zero net charge. Scattering via the nuclear force is called *nuclear scattering* and will be presented first. The magnetic scattering due to its spin will be introduced thereafter.

2.1.2 Nuclear scattering

In a scattering process with condensed matter a neutron acts as a weak perturbation of the scattering system. As a consequence the partial differential cross section can be derived from *Fermi's Golden Rule* leading to

$$\frac{\mathrm{d}^2\sigma}{\mathrm{d}\Omega_f \mathrm{d}E_f}\big|_{\lambda_i \to \lambda_f} = \frac{|\mathbf{k}_f|}{|\mathbf{k}_i|} \left(\frac{m_n}{2\pi\hbar^2} \right)^2 |\langle \mathbf{k}_f\lambda_f|V|\mathbf{k}_i\lambda_i\rangle|^2 \delta\left(\hbar\omega + E_i - E_f \right), \tag{2.1.4}$$

where the λ_i, λ_f represent the initial and the final state with energies E_i, E_f, $\mathbf{k}_i$, and $\mathbf{k}_f$ the respective momenta and m_n the neutron mass. The potential describing the single neutron-nucleus interaction as required for *Fermi's Golden Rule* is realized by the so called Fermi pseudopotential

$$V(\mathbf{r}) = \frac{2\pi\hbar^2 b}{m}\delta(\mathbf{r}), \tag{2.1.5}$$

that is short range and proportional to the nuclear scattering length b. A derivation of this potential can be found for example in Ref. [43].

A crystal represents an assembly of nuclei with positions $\mathbf{R}_j$. To take lattice vibrations into account, $\mathbf{R}_j$ has to be considered as a function of time. The nuclear interaction of a neutron with such an ensemble is therefore given by the superposition

$$V(\mathbf{r}) = \frac{2\pi\hbar^2}{m}\sum_j b_j\delta(\mathbf{r} - \mathbf{R}_j), \tag{2.1.6}$$

where $\mathbf{r}$ is the neutron's position and b_j the nuclear scattering length of the jth nucleus in the assembly, that can vary even for monoatomic samples, because isotopes of the same element have different scattering lengths. In a scattering experiment a statistical distribution of initial states $P(\lambda_i)$ of the magnetic moments is given and summation over all final states of the magnetic moments is required. Representing the δ-distribution by a Fourier-integral one finally obtains the partial differential cross section as a sum of coherent and incoherent parts

$$\begin{aligned}\frac{\mathrm{d}^2\sigma}{\mathrm{d}\Omega_f\mathrm{d}E_f} &= \left(\frac{\mathrm{d}^2\sigma}{\mathrm{d}\Omega_f\mathrm{d}E_f}\right)_{\mathrm{coh}} + \left(\frac{\mathrm{d}^2\sigma}{\mathrm{d}\Omega_f\mathrm{d}E_f}\right)_{\mathrm{inc}}\\ &= \frac{|\mathbf{k}_f|}{|\mathbf{k}_i|}\frac{N}{4\pi}\left(\sigma_{\mathrm{coh}}S(\mathbf{Q},\omega) + \sigma_{\mathrm{inc}}S_i(\mathbf{Q},\omega)\right).\end{aligned} \tag{2.1.7}$$

The quantities σ_{coh} and σ_{inc} are the coherent and the incoherent cross sections respectively. The coherent scattering cross sections σ_{coh} results from scattering processes common to all atoms in the sample. Thus, σ_{coh} only depends on one averaged nuclear scattering length $\langle b\rangle^2$. In contrast, the incoherent scattering cross sections σ_{inc} depends on the deviation from this average $\langle b^2\rangle - \langle b\rangle^2$. Further, N is the number of nuclei.

The two function $S(\mathbf{Q},\omega)$ and $S_i(\mathbf{Q},\omega)$ are the correlation and the self-correlation function respectively given by

$$S(\mathbf{Q},\omega) = \frac{1}{2\pi\hbar N}\sum_{jj'}\int_{-\infty}^{\infty}\langle e^{-i\mathbf{Q}\mathbf{R}_{j'}(0)}e^{i\mathbf{Q}\mathbf{R}_j(0)}\rangle e^{-i\omega t}\mathrm{d}t \tag{2.1.8}$$

and

$$S_i(\mathbf{Q}, \omega) = \frac{1}{2\pi\hbar N} \sum_j \int_{-\infty}^{\infty} \langle e^{-i\mathbf{Q}\mathbf{R}_j(0)} e^{i\mathbf{Q}\mathbf{R}_j(0)} \rangle e^{-i\omega t} dt. \tag{2.1.9}$$

Both functions only depend on the momentum and energy transfer from a neutron to the sample.

As a consequence of translational invariance the incoherent scattering given by $S_i(\mathbf{Q}, \omega)$ results in an isotropic background in wave vector for the neutron experiments undertaken within this thesis.

In general, the coherent part provides information about the collective effects among different atoms such as elastic Bragg scattering or inelastic scattering by phonons or triplons and magnons, whereas the incoherent part provides information about the time correlation of an atom with itself as well as information about individual particle motion such as diffusion [45].

2.1.3 Magnetic scattering

Due to its magnetic dipole moment the neutron interacts with the magnetic moments of the ions in a crystal. A neutron's magnetic moment equals to

$$-\gamma \mu_N \boldsymbol{\sigma}, \tag{2.1.10}$$

where $\mu_N = \frac{e\hbar}{2m_p}$ is the nuclear magneton, that is correlated the the proton mass m_p and the electron charge e. The gyromagnetic ratio is $\gamma = 1.913$ and $\boldsymbol{\sigma}$ is the Pauli spin operator for the neutron with eigenvalues ± 1. In general each electron of an atom, at position $\mathbf{R}_i$ that has a spin and an orbital angular momentum, creates a magnetic field $\mathbf{B}_i$ given by the *Biot-Savart* law

$$\mathbf{B}_i = -\frac{\mu_0}{2\pi} \mu_B \left(\nabla \times \left(\frac{\mathbf{S}_i \times \mathbf{R}_i}{R_i^3} \right) + \frac{\mathbf{L}_i \times \mathbf{R}_i}{R_i^3} \right). \tag{2.1.11}$$

The operators $\mathbf{S}_i$ and $\mathbf{L}_i$ are the spin and orbital angular momenta of the ith electron. The Bohr magneton is defined by $\mu_B = \frac{e\hbar}{2m_e}$ with the electron mass m_e. The total field created by an ion is given by the sum over all electrons, where $\mathbf{S}_i$ and $\mathbf{L}_i$ are replaced by the total spin $\mathbf{S}$ and the total angular momentum $\mathbf{L}$ of the ion.

For the cuprate compounds, $La_4Sr_{10}Cu_{24}O_{41}$ and $Sr_{2.5}Ca_{11.5}Cu_{24}O_{41}$, studied within this thesis the total angular momentum is zero ($L = 0$) due to orbital quenching and

the total spin equals $S = \frac{1}{2}$. This means, that for the magnetic partial differential cross section only the spin has to be considered.

Eq. 2.1.4 has now to be modified such that the change of the spin state from σ to σ' due to an interaction of the neutron with the ion is also taken into account. The magnetic interaction potential of the jth ion is given by

$$V = -\gamma \mu_n \boldsymbol{\sigma} \cdot \mathbf{B}_j, \qquad (2.1.12)$$

where $\mathbf{B}_j$ is the total magnetic field created by the total spin $\mathbf{S}_j$ (and in the general case including the total $\mathbf{L}_j$) of the jth ion. Inserting this potential into Eq. 2.1.4 results in a partial differential cross section for a compound with only one type of magnetic ion (within this thesis it is Cu^{2+})

$$\frac{\mathrm{d}^2\sigma}{\mathrm{d}\Omega_f \mathrm{d}E_f} = (\gamma r_0)^2 N \frac{|\mathbf{k}_f|}{|\mathbf{k}_i|} \left(\frac{g}{2} F(\mathbf{Q})\right)^2 \exp\left(-2WQ\right) \sum_{\alpha\beta} \left(\delta_{\alpha\beta} - Q_\alpha Q_\beta\right) S^{\alpha\beta}\left(\mathbf{Q}, \omega\right),$$

$$(2.1.13)$$

where $(\gamma r_0) = 5.29\mathrm{fm}$ is constant, g is the Landé factor for the magnetic ion and $F(\mathbf{Q})$ its magnetic form factor. The magnetic form factor is the Fourier transform of the normalized unpaired spin density on a single magnetic atom and is rapidly falling off with $|\mathbf{Q}|$. The Debye-Waller factor $\exp\left(-2WQ\right)$ is neglected in most cases, because it falls off slower with $|\mathbf{Q}|$ than the form factor. The term $\left(\delta_{\alpha\beta} - Q_\alpha Q_\beta\right) S^{\alpha\beta}\left(\mathbf{Q}, \omega\right)$ results from the magnetic interaction potential. Only the component of $\mathbf{S}$ perpendicular to $\mathbf{Q}$ contributes to the scattering amplitude. The quantity $S^{\alpha\beta}\left(\mathbf{Q}, \omega\right)$ is the Fourier transform of the dynamical spin correlation function, which is given by

$$S^{\alpha\beta} = \frac{1}{2\pi N} \sum_{ij} \exp\left(i\mathbf{Q} \cdot (\mathbf{R}_i - \mathbf{R}_j)\right) \int_{-\infty}^{\infty} \exp(\mathrm{i}\omega t) \langle S_i^\alpha(0) S_j^\beta(t)\rangle \mathrm{d}t, \qquad (2.1.14)$$

where $S_j^\beta(t)$ is the time dependent spin component of the jth magnetic ion.

The magnetism of the materials treated within this thesis can be well described by the Heisenberg Hamiltonian, that will be introduced in detail in Chapter 4. Within the Heisenberg Hamiltonian the total z component of the spin is conserved resulting in

$$S^{\alpha\beta}(\mathbf{Q}, \omega) = 0, \qquad (2.1.15)$$

if $\alpha \neq \beta$ and only

$$S^{\alpha\alpha}(\mathbf{Q}, \omega) \neq 0 \qquad (2.1.16)$$

with $\alpha = \{0 \pm 1\}$. At zero temperature and zero external magnetic field the dynamical spin correlation function is given by

$$S^{\alpha\alpha}(\mathbf{Q}, \omega) = \sum_{\lambda_i \lambda_f} |\langle \lambda_f | S_{\mathbf{Q}}^\alpha | \lambda_i \rangle|^2 \delta \left(\hbar\omega - E_f + E_i \right) \qquad (2.1.17)$$

where the Fourier transform of the spin operator is

$$S_{\mathbf{Q}}^\alpha = \frac{1}{\sqrt{N}} \sum_j S_j^\alpha \exp \left(i\mathbf{Q}\mathbf{R}_j \right) \qquad (2.1.18)$$

and λ_i and λ_f are the initial and the final state respectively. The quantity in the absolute value in Eq. 2.1.17 is defined as the spectral weight. The one-particle spectral weight in particular will be of interest for the temperature dependency investigated within this work.

2.2 Experimental setup

In this section the typical experimental setup for neutron scattering experiments is presented. Though focus is laid on the particular setup related to this thesis, some possible variations are also briefly discussed.

A complete arrangement of an inelastic neutron scattering experiment is sketched in Fig. 2.2.1. The setup can be divided into three parts: i) the production of high energy neutrons, ii) moderation of the neutrons to the thermal level and iii) the scattering experiment itself.

At the very beginning electrons are produced by thermal emission and they are accelerated by a voltage device towards hydrogen gas. By the collision of the electrons with the gas molecules free protons H^+ are produced, because the valence electrons are removed from the hydrogen atoms during the collision. The free protons then are accelerated by further voltage devices up to 70MeV and guided by magnets towards the synchroton, where the protons are finally accelerated up to 800MeV. In Fig. 2.2.1 a color code is applied as will be described in what follows. All blue lines indicate that hydrogen is involved.

By the use of kicker magnets bunches of high energy protons are removed from the synchroton and guided towards a target, where spallation takes place. The target consists of a heavy metal such as for example Pb, U, Hg or Ta. The fast protons hitting the
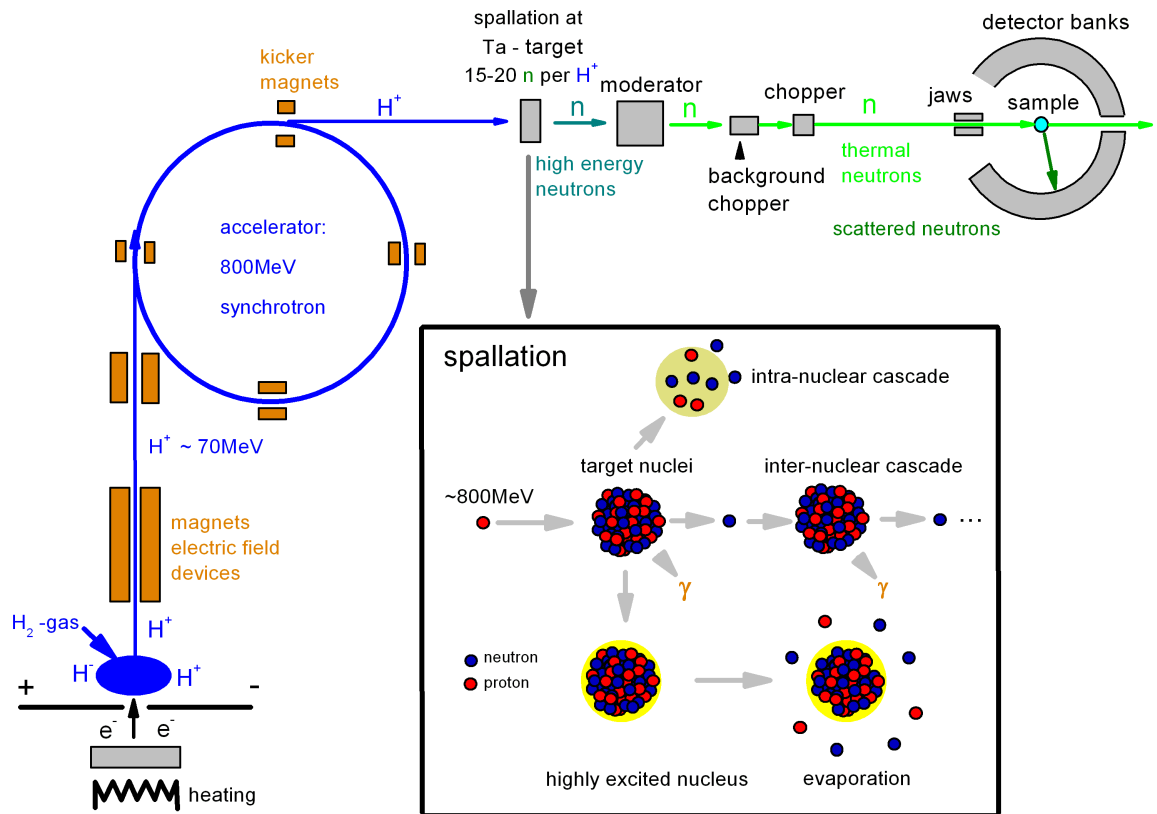
Figure 2.2.1: Experimental setup as used for example at the ISIS facility. Using an accelerator high energy protons are produced, that are guided to a heavy target of Tantalum for example. At the Ta-target the spallation process takes place, which releases high energy neutrons with a wide range of energies. These high energy neutrons are cooled down in the moderator resulting in thermal neutrons with a wide range of lower energies. The thermal neutrons are monochromized by chopper devices towards the sample. The scattered neutrons then are detected with angular and position resolution by huge detector banks composed of Helium tubes.

target interact with the heavy nuclei of the target, which in turn release free high energy neutrons (dark green line) by spallation. Spallation will be explained in more detail in the Section 2.3.

To make the released neutrons usable for neutron scattering experiments, they are decelerated in the moderator to the thermal level in order to increase the scattering probability and hence the cross section. To study magnetic excitations, water is the best choice as will be explained in detail in Section 2.3.1. The thermalized neutrons (light green line)

leaving the moderator possess a wide energy distribution in the meV range. With the use of a chopper device monochromatic neutrons with a sharp well defined energy distribution are selected and directed towards the sample under study.

The neutrons scattered (olive green) at the sample are measured with angular and position resolution by huge helium detector banks. A data aquisition device generates an intensity map in reciprocal space, that allows for investigation of the magnetic features of the sample in dependence of momentum and energy transfer.

In the following the various stages building the core of scattering experiments will be explained step by step in more detail. They can be skipped by the experienced reader. Starting with neutron sources, where spallation and fission are compared, aspects of the moderation will be discussed thereafter. Two types of instrumental setups will be discussed in more detail. Finally the calibration of neutron intensities, the sample growth and its preparation are debated.

2.3   Neutron sources

High energy neutrons are produced either by fission or by spallation. These two different ways of neutron production will be explained next.

- **Reactor Source**

   When neutrons are produced in a nuclear reactor, they arise from fission of ^{235}U according to

$$n + {}^{235}_{92}U \rightarrow {}^{236}_{92}U \rightarrow {}^{144}_{56}Ba + {}^{89}_{36}Kr + 3n + 177 MeV. \qquad (2.3.1)$$
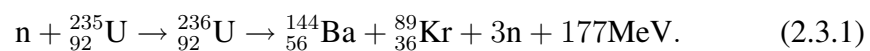
   The process is illustrated in Fig. 2.3.1. A slow neutron hits a $^{235}_{92}$U atom and it is absorbed by it resulting in $^{236}_{92}$U. The absorption of the neutron excites the uranium nucleus, which in turn decays into $^{144}_{56}$Ba and $^{89}_{36}$Kr, where three neutrons and γ rays are additionally released. These highly energetic neutrons then collide with other nuclei, that decay analogously.

   In this chain reaction the neutrons are produced continuously in time with a typical flux of about $\sim 10^{15}$ neutrons / cm^2 s. The neutron flux in the core of a reactor obeys a Maxwellian distribution in neutron velocities.
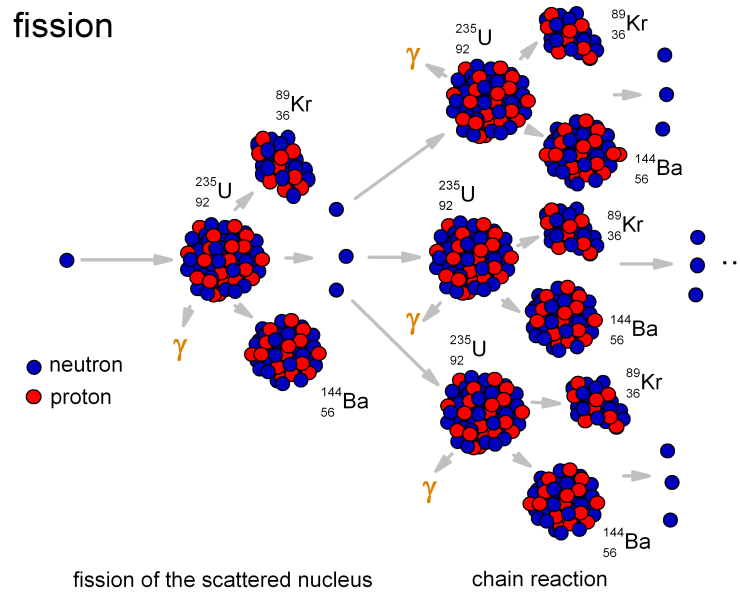
Figure 2.3.1: In reactors the fission process of uranium leading to a chain reaction is used to produce a continuous beam of neutrons.

- **Spallation Source**

  At a spallation source neutrons are produced by bombarding high energy protons from a synchroton on a heavy target such as U, W, Ta, Pb or Hg. The spallation process is illustrated in Fig. 2.3.2 An internuclear cascade is activated by the collision of the protons with the heavy nuclei of the target. Individual nuclei are promoted into a highly excited state. These excited nuclei in turn evaporate protons and mainly neutrons in order to release energy. Some of the free neutrons and protons then trigger new reactions while others leave the target. On average each proton hitting the target produces about 15-20 neutrons [46].

  In this reaction the produced neutron flux appears in bursts of about 10^{14} neutrons with an initial pulse width of 1μs at frequencies between 10 and 50 Hz depending on the proton accelerator. The energy spectrum of the spallation source differs slightly from that of a reactor.

However, in both cases the produced neutrons possess too high energies making them inefficient for inelastic scattering experiments. Therefore the neutrons have to be moderated as will be explained in the following.
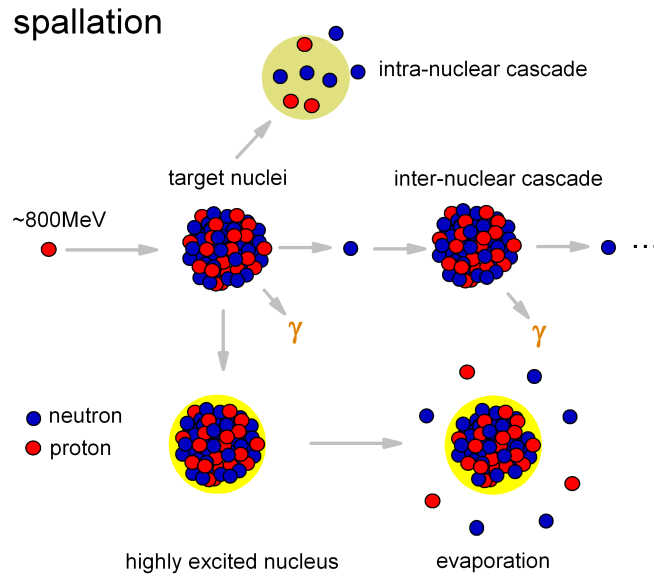
Figure 2.3.2: In the spallation process neutrons are produced by bombarding high energy protons on a heavy target. The collision of a heavy nucleus in the target with the proton excites the nucleus leading to evaporation of neutrons and protons.

2.3.1 Moderation of neutrons

Typically magnetic excitations in solids lie in the meV range. In order to use neutrons for magnetic excitation studies, the scattering neutrons have to possess a kinetic energy of the order of the magnetic excitation energy which lies between 5-1000 meV.

Before the produced high energy neutrons (MeV) from the spallation can be used for such neutron scattering experiments on crystals, the neutrons have to be decelerated to the thermal energy range (meV). This is done in the moderator already introduced in Fig. 2.2.1. The moderator consists of a medium that has an atomic mass of the same order as the neutron mass allowing for an efficient moderation. The chosen moderator medium determines the moderator temperature, which in turn determines the spectral energy distributions of the produced neutrons.

Various media are in use, among them are liquid hydrogen H_2 operating at 20K, liquid methane operating at 100K and water H_2O operating at 316K. The latter is used in all experiments carried out in this thesis. The resulting spectral energy distributions of the moderated neutrons using the diverse media is schematically sketched in Fig. 2.3.3.

For the studies on the cuprates within this thesis water was used to moderate the neu-

trons, because only water as moderator allows for selecting neutrons up to an energy of $100 - 1000$meV (see Fig. 2.3.3), though the neutron flux is highly reduced at these energies.
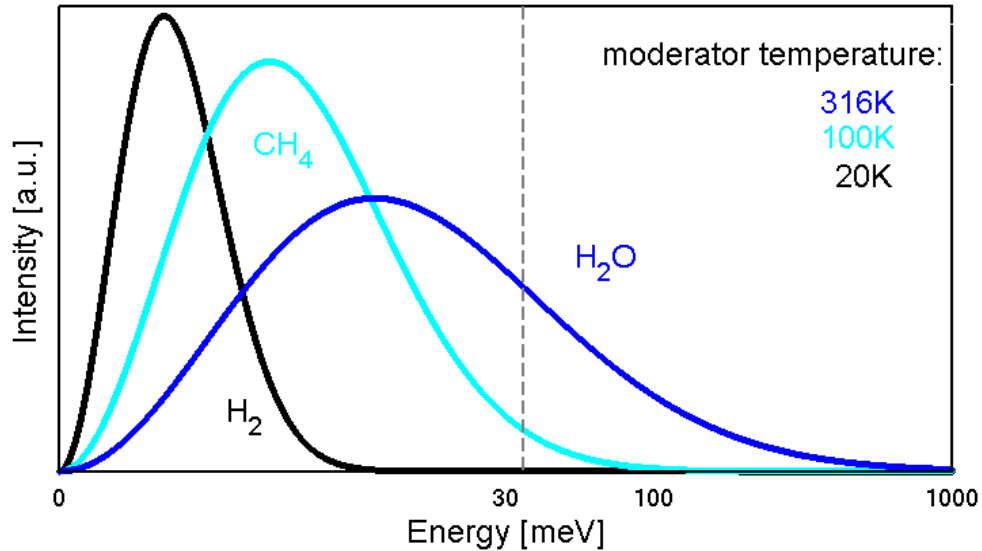
Figure 2.3.3: To moderate high energy neutrons down to the thermal level various moderators such as liquid hydrogen H_2 (20K), liquid methane CH_4 (100K) or water H_2O (316K) can be used. The temperature of the chosen moderator determines the energy distribution of the thermalized neutrons. The figure shown here is purely schematic and is not based on measurements.

2.4   Neutron detection and measurement

To gain information about magnetic excitations in the sample, both the energy and the momentum of the scattered neutrons have to be measured. Therefore several devices to determine the neutron rates and energies are employed such as, e.g., the neutron spin-echo spectrometer, the backscattering spectrometer, the triple axis spectrometer and the time-of-flight spectrometer.

In this thesis, a time-of-flight (TOF) spectrometer is employed to measure the distribution of the scattered neutrons. Neutron detection itself is carried out by a Helium-3 detector bank, which allows for an angular resolved detection of the incoming scattered neutrons. From the time-of-flight and from the scattering angle of a scattered neutron both energy and momentum transfer can be deduced.

2.4.1 Helium-3 detector

Because of the zero net charge of the neutron, it cannot produce ionisation in a detector directly. It has to interact with a nucleus to produce a secondary charged particle before, which then in turn can be detected. The most common reaction for the detection of thermal neutrons as utilized in Helium-3 tubes is given by

$$n + {}^3He \rightarrow p^+ + {}^3H^+ + 765keV, \tag{2.4.1}$$

where the proton and the triton are detected both by a gas filled proportional counter using ${}^3He$ fill gas. Quench gas is added to control the ionisation process [47].

2.4.2 Calibrating neutron intensities

As mentioned in the preceding section, Helium-3 tubes only measure secondary ionisation. Hence, measured data have to be related to the intensity of the incoming flux of scattered neutrons. To this end, all Helium-3 tubes have to be calibrated before and/or after the scattering experiment. Calibration is carried out by means of the so called *white beam*. This white beam offers an isotropic well-defined intensity distribution of scattered neutrons. It is produced by a cylindrical vanadium standard, that is placed in the sample position. With this vanadium standard a measurement is undertaken at the neutron energy and the chopper frequency that are used for the proper experiment. The vanadium scatters the neutrons isotropically due to its large and dominant incoherent scattering [45], allowing for calibrating all helium tubes consistently.

2.4.3 Time-of-flight spectrometer

The main principle of the time-of-fight spectrometer (TOF) is to measure the time, the scattered neutrons need to reach the detector, gaining information on the velocities and thus on the energies of the scattered and detected neutrons. Using large arrays of position sensitive detectors facilitates to measure a large range of energy transfers $\hbar\omega$ as well as momentum transfers Q at the same time.

However, there are two slightly different setups for the time-of-flight method. The first one employs the so called *direct geometry* and the second one the so called *indirect geometry*.

Figure 2.4.1: A sketch of a time-of-flight spectrometer with a direct geometry. The incoming neutrons possess a fixed energy and after the scattering process all scattered neutrons are measured with angular resolution. The choice of the chopper determines the energy resolution.

Direct geometry

In the setup of direct geometry sketched in Fig. 2.4.1 the incoming neutrons are monochromatic, which means that they possess the same kinetic energy before they are scattered at the sample. The scattered neutrons are detected by tall position sensitive Helium-3 detectors. The energy resolution is determined by the choice of the monochromating chopper.

The neutrons are monochromized by a so called *Fermi chopper*. The Fermi chopper consists of a rotating disc with slits in a cylinder, which is about 10 cm in diameter. To avoid friction a magnetic rotor bearing is used.

Indirect geometry

In the setup of indirect geometry sketched in Fig. 2.4.2 the incoming neutrons are polychromatic. Only neutrons with one fixed energy are detected after the scattering process by means of an analyser crystal. Hence, only neutrons whose wave length fulfill the Bragg condition will be detected.
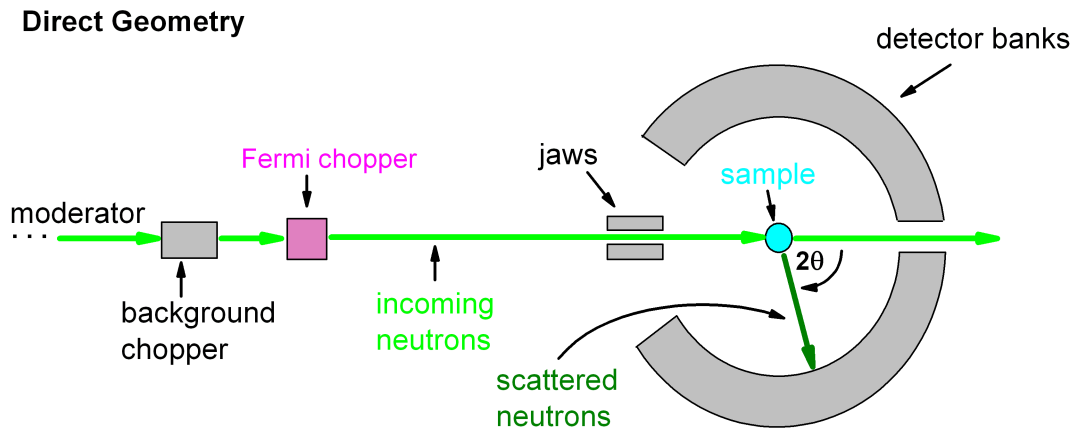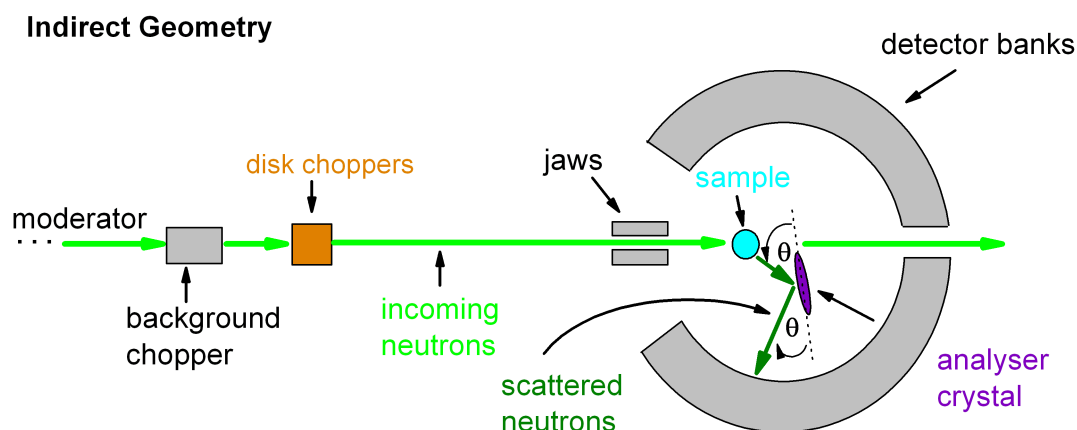
Indirect Geometry

Figure 2.4.2: A sketch of a time-of-flight spectrometer with an indirect geometry. The incoming neutrons possess a broad range of energy and after the scatter process only scattered neutrons with a certain final energy are measured. The selection of one final energy is done by means of an analyser crystal fulfilling Bragg's condition.

2.5 Sample growth and preparation

The compounds studied within this thesis are in particular the cuprates $La_4Sr_{10}Cu_{24}O_{41}$, $Sr_{2.5}Ca_{11.5}Cu_{24}O_{41}$ and $Sr_8Ca_6Cu_{24}O_{41}$. For each compound single crystals were grown by the *travelling solvent floating zone method* (TSFZ). This method is used because of the peritectic melting point of the parent compound $Sr_{14}Cu_{24}O_{41}$ [48]. It allows to grow a monocrystalline sample from a polycrystalline rod of up to 7cm centimeters in length [48]. The grown crystals are elliptical in cross section (5mm x 4mm) [49]. X-ray studies determined that the shorter axis of the ellipse is along the b-axis and the longer along the a-axis [49].

For the neutron experiment several crystals of each compound were mounted as shown for $Sr_{2.5}Ca_{11.5}Cu_{24}O_{41}$ in figure 2.5.1. The sample consists of a four $Sr_{2.5}Ca_{11.5}Cu_{24}O_{41}$-crystal array (see also Fig. 2.5.1 for more details). The crystals are aligned on an aluminium gadget parallel to each other, but different in height. The alignment was performed on the four-circle-diffractometer E5 with better than 2 degrees accuracy at the HZB (Helmholtz Zentrum Berlin). For the experiment on $Sr_{2.5}Ca_{11.5}Cu_{24}O_{41}$ and $La_4Sr_{10}Cu_{24}O_{41}$, a closed cycle cryostat was used, allowing cooling for the sample without being in danger of an additional scattering background due to ice building on the
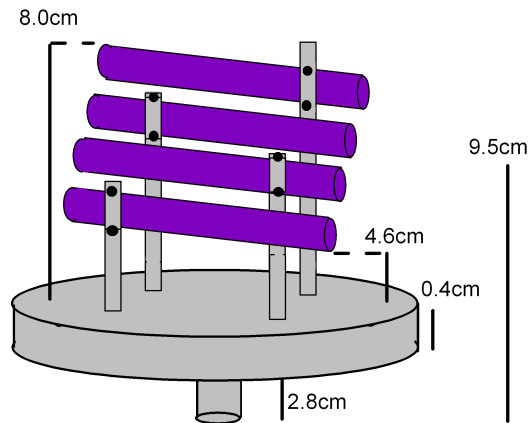
Figure 2.5.1: Four $Sr_{2.5}Ca_{11.5}Cu_{24}O_{41}$-crystal array, whose crystals are parallel to each other, but arranged at different heights.

sample.

Throughout this thesis the MAPS (**M**ultiple **A**ngle **P**osition **S**ensitive) spectrometer at ISIS, Rutherford Appelton Laboratory, U.K. was used representing a spectrometer with direct geometry. The neutron source at ISIS is a spallation source using a Ta target.

Chapter 3

Magnetic excitations and quasi-particles

During the last years, theoretical studies have led to a classification of different types of magnetic excitations in spin systems. While intensity plots only indicate the presence of some kind of magnetic excitation, depending on the underlying theoretical model the kind of magnetic excitation is different. Thus one has to distinguish between *spinons*, *magnons* and *triplons*. All terms will be explained in the following.

3.1 Quasi-particle

In many-body systems the low lying excited states above the system's ground state are the *elementary excitations* of the system. Quantized energy excitations are attributed to *quasi-particles*. The term quasi-particle corresponds to a single *particle*, whose motion is influenced by its surroundings and other particles, respectively. These *particles* are no real particles, as for example a neutron, though they exhibit typical particle features of definite momentum and energy and therefore they are called *quasi-particles*. However, also a quasi-particle is often just called particle for abbreviation.

3.2 Spinon and holon

Spin and charge are inseparable traits of an electron, but in one-dimensional solids, theory predicts their separation into collective modes as independent excitation quanta

37
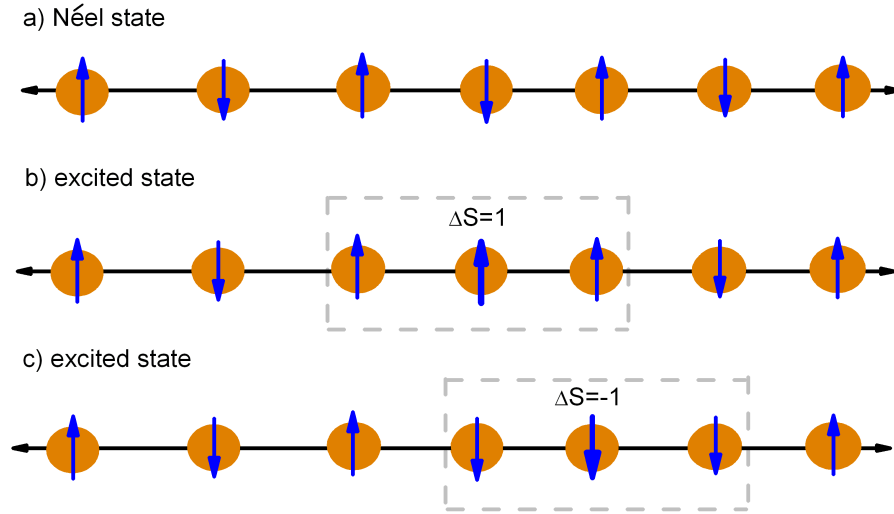
Figure 3.2.1: a) The Néel state of an antiferromagnet. A spin flip results in a magnon excitation with spin $\Delta S = \pm 1$ excitation in b) and c).

(or particles) called spinons and holons [50]. Thus the spinon presents a quasi-particle with zero charge and spin $\frac{1}{2}$, whereas the holon presents a quasi-particle with zero spin and charge e.

3.2.1   Magnon

A magnon is a magnetic boson with usually $S = 1$ [10]. The ground state of an $S = \frac{1}{2}$-antiferromagnet is given by the Néel state consisting of alternating directions of spins. This is sketched in Fig. 3.2.1. Spin waves in an antiferromagnet are magnons which are semi-classical spin waves, oscillations in the ordered state [10]. The term magnon, however, has also been applied to distinctly spin one magnetic bosons in dimerized systems with a singlet ground state, e.g. TlCuCl$_3$ or CuGeO$_3$ [10] until recently. To more clearly differentiate from spin waves, this class of excitation is now generally termed *triplon* coming from the triplet nature due to the SU(2) symmetry [10]. For the purpose of this thesis we restrict ourselves to the terms triplet and triplon.

3.2.2 Triplet and triplon

To introduce the terms triplet and triplon in more detail, the underlying model within this thesis - the antiferromagnetic spin-$\frac{1}{2}$ two leg ladder - will briefly be presented first.
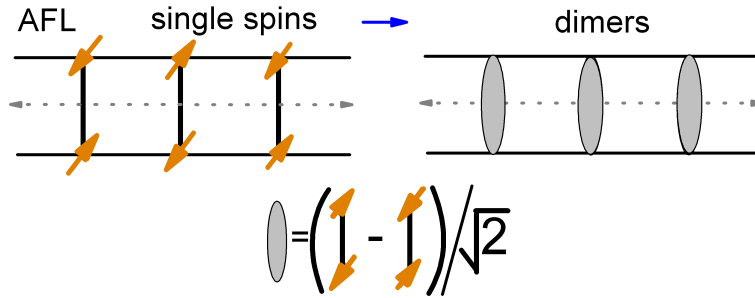
Figure 3.2.2: Schematic drawing of a dimer: On the left side an antiferromagnetic spin ladder (AFL) is sketched, whose spins indicated by orange arrows are aligned in an antiparallel fashion. Each pair of spins sitting on a rung form a dimer (grey ellipse on the right side) when coupled. The dotted centerline in each ladder indicates its continuation.

Dimer as basic building block

A spin-$\frac{1}{2}$ two leg ladder is presented in Fig. 3.2.2. On each rung two spin-$\frac{1}{2}$ are located antiparallely (left side of Fig. 3.2.2). Assuming the coupling along each rung $J_\perp$ to be much stronger than along the ladder $J_\parallel$ and much stronger than the cyclic exchange J_{cyc} (that decribes the interaction of four spins on a plaquette), each pair of spins on one rung form one unit, the *dimer* (grey ellipse at the bottom of Fig. 3.2.2). The spins on each dimer pair into a valence bond singlet, leading to a paramagnetic state which preserves spin rotation invariance and all lattice symmetries [32]. Each pair of spins on a rung pairs into a $S = 0$ state, the dimer's ground state $|s\rangle$ which is given by

$$|s\rangle = \frac{1}{\sqrt{2}} \left(|\uparrow\downarrow\rangle - |\downarrow\uparrow\rangle \right).$$

This dimer can be excited, resulting in a *triplet*. If a non-zero coupling along the ladder is assumed ($J_\parallel \neq 0$) the triplet becomes a *triplon*. Both the triplet and the triplon preserve all symmetries of the SU(2). The nature of the excitation depends on the underlying Hamiltonian. Therefore two parameters x and x_{cyc} are introduced and defined

by the ratio of the coupling constants.

$$x := \frac{J_{\parallel}}{J_{\perp}} \qquad \text{and} \qquad x_{\text{cyc}} := \frac{J_{\text{cyc}}}{J_{\perp}}. \tag{3.2.1}$$

Triplet
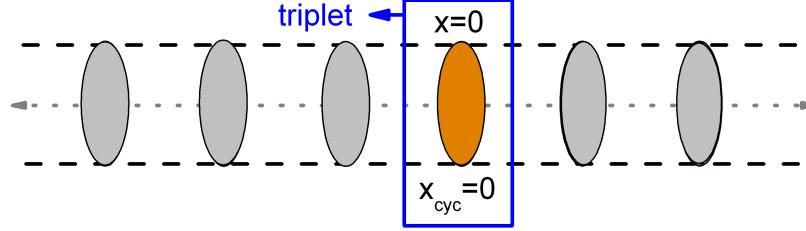
Figure 3.2.3: In the case of zero coupling ($x = 0$ and $x_{cyc} = 0$) among the dimers the excitation of a dimer results in a triplet (orange ellipse), that is spatially restricted to its rung. As the word triplet indicates, this excitation has a degeneracy of three. The dotted centerline indicates the continuation.

In the case $x = 0$ and $x_{cyc} = 0$ the ladder consists of a set of decoupled dimers. When a dimer is excited by breaking a valence bond, this leads to a threefold degenerated energy state with a total spin $S = 1$ represented by

$$|t\rangle = \left\{ |\uparrow\uparrow\rangle; \frac{1}{\sqrt{2}} \left(|\uparrow\downarrow\rangle + |\downarrow\uparrow\rangle \right); |\downarrow\downarrow\rangle \right\}.$$

This energy state is called *triplet*, when it is confined to its rung. Since in the case of decoupled dimers the triplet does not affect the surrounding dimers by exciting them, it is a confined excitation. We can consider it as a quasi-particle. In terms of spinons the triplet can be interpreted as a *bound spinon pair*.

Triplon

In the case $x \neq 0$ and $x_{cyc} \neq 0$ with $J_{\perp} \gg J_{\parallel}$ the ladder consists of weakly coupled dimers. Then an excited dimer is no longer confined to its rung, but it can hop locally to its neigbouring dimers as it is indicated by the three orange colored ellipses in Fig. 3.2.4. The triplon can be regarded as a kind of a dispersive triplet, which we take as the elementary excitation. The origin of the name triplon is therefore obvious. The

correlation between different dimers decays exponentially with distance along the ladder direction, because we assumed only weakly interacting dimers.The correlation length of a triplon is short due to its finite spin gap [9]. The triplon is not specific to the ladder model, but it is specific to the pairing of two spins to a $S = 1$ excitation.
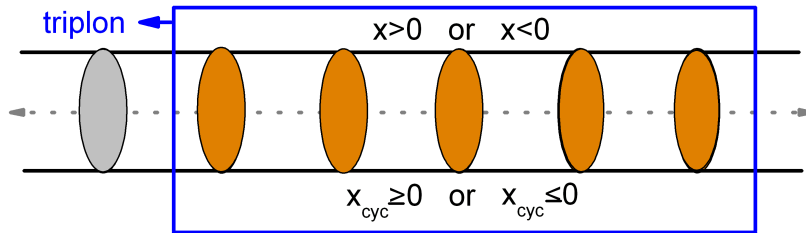
Figure 3.2.4: If the coupling among dimers is non-zero $x \neq 0$ and/or $x_{cyc} \neq 0$, the excitation of one dimer is not restricted to its rung, but it can evolve spatially, as it is indicated by the five orange colored ellipses.

Within this thesis we consider triplets as the elementary excitations. We call these quasi-particles triplons. In the next chapter the theoretical description of the antiferromagnetic spin-$\frac{1}{2}$ two leg ladder will be presented in more detail.

Chapter 4

Introduction to the theory of spin ladders

The theoretical methods employed in this thesis are a combination of continuous unitary transformation in its perturbative fashion and mean-field theory. In this context the evolution of the single-mode, i.e., one-triplon, contribution of a two-leg $S = \frac{1}{2}$ spin-ladder to the dynamical structure factor at finite temperature is treated. Furthermore the influence of the coupling exchange for weakly coupled ladders is investigated. Therefore each method will briefly be summarized in the following. Then the combination of both methods will be presented in Chapters 5 and 6 applying them to the problems considered. This combination is favored by the fact that both methods rely on a quasi-particle description of the excitations.

4.1   Continuous unitary transformation - CUT

Diagonalizing a Hamiltonian is a main concern in the study of many particle systems in quantum mechanics. Besides several other methods, such as, e.g., exact diagonalization (ED) [51, 52] or density matrix renormalization group (DMRG) techniques [52, 53, 54, 55] the method of continuous unitary transformation (CUT) is a promising technique to extract the physical properties of a many particle system.
A Hamiltonian can be diagonalized in general by the use of an appropriate unitary transformation. However, for complex systems it is often difficult to find such an appropriate unitary transformation. Thus, instead of applying successively a sequence of unitary

transformations to the Hamiltonian under study, a family $U(l)$ of continuously varying unitary transformations depending on the so called flow parameter $l \in \mathbb{R}$ can be applied. This method is called continuous unitary transformation (CUT) [56]. The CUT method was invented independently by Wegner [57] and Głazek and Wilson [58, 59] in 1994. It is briefly summarized in the following.

The Hamiltonian under study is interpreted as a function of the so called *flow* parameter $l \in \mathbb{R}$. The original Hamiltonian, that has to be transformed into a diagonal Hamiltonian in the optimal case, is defined by $H(l = 0) = H_0$. In the next step a unitary transformation

$$H(l) = U(l)H(0)U^{\dagger}(l) \tag{4.1.1}$$

with $U(l)$ dependent on l is introduced, so that $H(l = \infty)$ is a diagonal operator. The unitary transformation can be stopped at any arbitrary value of the flow parameter l [60]. The anti-Hermitian generator $\eta(l)$ of the transformation $U(l)$ is defined by

$$\eta(l) = \frac{\partial U(l)}{\partial l}U^{\dagger}(l), \tag{4.1.2}$$

which has to be anti-Hermitian, so that U is unitary. The derivative of H with respect to the flow parameter l is now given by the so-called *flow equation*

$$\partial_l H(l) = [\eta(l), H(l)] \tag{4.1.3}$$

defining the CUT method. The transformation stops automatically when the commutator $[H(l), \eta(l)]$ vanishes, which is generically the case for $l \to \infty$ [60]. The final form of the effective Hamiltonian $H_{\text{eff}} = H(l = \infty)$ depends on the form of the infinitesimal generator $\eta(l)$, which in turn determines the transformation $U(l)$. This will be discussed in the following section.

Other operators, e.g., observables O, that have to be considered in order to gain information on the spectral properties of the system under study such as the dynamical structure factor $S_T(k, \omega)$, have to be transformed by the same CUT as the Hamiltonian. Hence the same generator $\eta(l)$ as in Eq. (4.2.1) is used

$$\partial_l O(l) = [\eta(l), O(l)]. \tag{4.1.4}$$

4.2 Choice of generators

As mentioned before the form of the generator $\eta(l)$ influences the resulting form of the effective Hamiltonian. Wegner originally proposed the generator

$$\eta(l) = [H_d(l), H(l)] , \qquad (4.2.1)$$

where $H_d(l)$ denotes the diagonal part of the Hamiltonian $H(l)$ under study with respect to a particular basis [57]. For $l = 0$ the commutator 4.2.1 does not vanish. During the flow $H(l)$ changes its appearance. The flow is stopped when the commutator 4.2.1 vanishes, this is when H has reached a block diagonal form [61].

However, the construction of the generator is not unique. Finding an appropriate generator is an intuitive task [61]. The construction of the generator depends on the physics of the system under study. Criteria for the choice of a generator can be, e.g., the conservation of a band structure in the original Hamiltonian during the flow (e.g. Ref. [62]) or the creation of (quasi)particle number conserving effective many-body Hamiltonians (Refs. [33, 34]) as achieved by Knetter and Uhrig. If, e.g, quasiparticles with a finite lifetime are studied, a generator leading to ground states with finite lifetime may be advantageous. This was the starting point for the construction of new generators by Fischer et al. [63]. Further, in Ref. [63] a detailed discussion of construction principles for various generators as well as of their advantages and disadvantages is presented. Other examples are considered in Ref. [60].

4.3 Perturbative CUT

In order to apply the CUTs in their perturbative version the Hamiltonian H has to consist of at least two parts according to

$$H = H_0 + xV, \qquad (4.3.1)$$

where the unperturbed part is given by H_0 and the perturbed part by xV. The expansion parameter is x, that has to be small representing a small perturbation of the unperturbed system.

Furthermore we assume, that the energy spectrum of the unperturbed part H_0 is equidistant with a lower boundary meaning that the eigenenergies are proportional to the number of elementary excitations and hence to the particle number [56, 34]. Secondly we

assume, that the perturbation term decomposes into a sum of operators T_n

$$V = \sum_{n=-N}^{N} T_n \qquad N \in \mathbb{N}, \tag{4.3.2}$$

each of which changes the number of particles by n. The Hamiltonian can now be written as

$$H = H_0 + x \sum_{n=-N}^{N} T_n. \tag{4.3.3}$$

To this Hamiltonian the flow equation is applied. Hence, the flow parameter is introduced in the Hamiltonian according to

$$H(l) = H_0 + x \sum_{n=-N}^{N} T_n(l). \tag{4.3.4}$$

The transformation only acts on the perturbative part of the Hamiltonian, because the unperturbed Hamiltonian H_0 is chosen to be already diagonal. Since (quasi-) particle conserving CUTs (for a detailed description see Refs. [62, 33, 34, 63]) are applied, the generator required creates particle number conserving effective Hamiltonians. Such a generator is defined by

$$\eta_{ij}^{\mathrm{pc}}(l) = \mathrm{sgn}(q_i - q_j) H_{ij}(l), \tag{4.3.5}$$

in an eigenbasis $|q_i\rangle$ of the particle-number operator Q with eigenvalues $q \in \mathbb{N}_0$. The index i in the eigenvectors is an additional index necessary due to the degeneracy of the eigenvalues. The term H_{ij} denotes the transition from state j to state i. This choice of the generator results in the effective Hamiltonian H_{eff} being block-diagonal. Due to the perturbative treatment H_{eff} is obtained as a high-order series expansion in the parameter x.

Because the perturbative treatment is realized based on an expansion about $x = 0$, the results for $x > 0$ deteriorate rapidly. However applying extrapolation schemes such as Padé approximation [64], permit to determine a small range of x with reliable results.

Further detailed information on the PCUT method can be found in the literature. In [29], [28] the PCUT based on the particle conserving generator η^{pc} is presented in detail. For zero temperature it is often sufficient just to treat the lowest lying excitation to describe the physics of the system properly. However, for finite temperatures the higher

lying excitations need to be included, which typically results in operator terms with more than two operators leading to a more difficult situation. In this case a mean field approach may help as introduced in the following.

4.4 Mean-field decoupling - MFD

Many-particle systems are usually difficult to treat exactly. Here, mean-field theory offers a viable method based on a suitable approximation. Instead of dealing with the original n-particle system, the problem is reduced to treating only a one-particle system in an effective field. This external field is given by the possible interactions with the other $(n-1)$-particles. This method allows for gaining insight into some physical properties of the system relatively quickly. However, a correct consideration of the possible interactions is challenging such as for instance the correct calculation of a system's partition function.

In the realm of quantum mechanics a mean field approach means to replace operators t by their mean values $\langle t \rangle$, which in turn results in neglecting quantum fluctuations, which may be important in some cases.

A mean field approach is well suited to describe averaged quantities in statistical processes, such as, e.g., thermal effects. Being interested in the statistics of populated states it is appropriate to introduce the hardcore constraint on the level of averaged quantities rather than on the level of individual excitations itself. Furthermore, this offers a simplified approach.

Within this thesis we restrict ourselves to the lowest lying excitation and thus the system under study is based locally on a four dimensional Hilbert space. This space is spanned by four states building a basis for it. These states are produced by applying the creation operators $s^\dagger, t_{-1}^\dagger, t_0^\dagger, t_{-1}^\dagger$ to the vacuum state $|0\rangle$. The creation operators fulfill the so called *hardcore* constraint

$$\mathbb{1} = s^\dagger s + \sum_\alpha t_\alpha^\dagger t_\alpha, \quad \alpha \in \{-1, 0, 1\} \tag{4.4.1}$$

for *hardcore* bosons, which implies particle-number conservation in terms of singlets *and* triplets. This constraint builds the fundamental equation for the mean field treat-

ment. Replacing the operators by their averages gives

$$1 = \langle s^\dagger s \rangle + 3 \langle t^\dagger t \rangle, \qquad (4.4.2)$$

where the factor three arises from the fact, that the average $\langle t^\dagger t \rangle$ is independent of α. This is the case because we do not apply an external field so that no spontaneous symmetry breaking appears. For the theory at finite temperature excitations have to be included that are proportional to multi-operator terms. These are difficult to treat and therefore the mean field approach is applied. Here, Wick's theorem will play an important role allowing for the approximative simplified representation

$$t_1^\dagger t_2^\dagger t_3 \approx t_1^\dagger \langle t_2^\dagger t_3 \rangle + t_2^\dagger \langle t_1^\dagger t_3 \rangle. \qquad (4.4.3)$$

The averages $\langle t^\dagger t \rangle$ are computed and inserted into Eq. 4.4.2 in order to solve this equation self-consistently for the mean field parameter s. Detailed information is presented in Chapter 5. A similar approach is applied to the inter-ladder coupling as well presented in more detail in Chapter 6.

Chapter 5

Temperature evolution in the isolated spin ladder

In this chapter we combine the results of perturbative continuous unitary transformations with a mean-field calculation to determine the evolution of the single-mode, i.e., one-triplon, contribution to the dynamical structure factor of a two-leg $S = 1/2$ ladder on increasing temperature from zero to a finite value. The temperature dependence is induced by two effects: (i) no triplon can be excited on a rung where a thermally activated triplon is present; (ii) conditional excitation processes take place if a thermally activated triplon is present. Both effects diminish the one-triplon spectral weight upon heating. It is shown that the second effect causes an important vertex correction in the calculation of the dynamic structure factor. The matrix elements describing the conditional triplon excitation in the two-leg Heisenberg ladder with additional four-spin ring exchange are calculated up to order 9 in perturbation theory. The calculated results are compared to those of an inelastic neutron scattering experiment on the cuprate-ladder compound $La_4Sr_{10}Cu_{24}O_{41}$ showing convincing agreement for established values of the exchange constants.

5.1 Model of the isolated ladder

The system we are investigating in particular is a single two-leg ladder with localized $S = 1/2$ at each vertex as it is depicted in Fig. 5.1.1, see Ref.[65] and references therein. The ground state has zero spin and the elementary excitations are of triplet character (see

Section 3.2.2), i.e., $S = 1$. Thus we dub them triplons [66] in order to distinguish them from the elementary spin wave excitations of systems with magnetic long-range order (see Chapter 3). The centers of the triplons can be seen to sit on the rungs of the ladder. The model is characterized by Heisenberg exchange couplings on the rungs $J_\perp$ and on
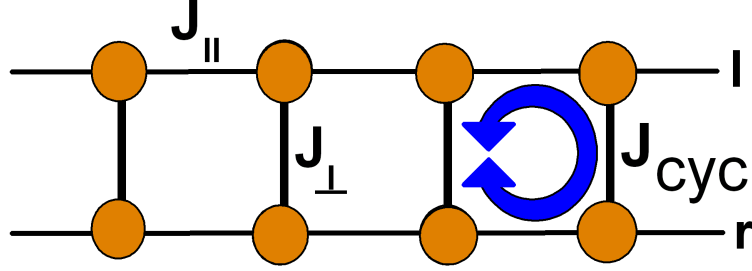

Figure 5.1.1: Sketch of the two-leg spin ladder. Circles indicate spins with $S = 1/2$. Solid lines represent the two-spin exchange couplings on the rungs $J_\perp$ and on the legs $J_\parallel$. The four-spin cyclic exchange is denoted by J_{cyc}.

the legs $J_\parallel$ of the ladder as well as by a four-spin cyclic exchange J_{cyc}. The corresponding Hamiltonian in units of $J_\perp$ reads

$$
\begin{aligned}
\frac{H}{J_\perp} &= H_\perp + \frac{J_\parallel}{J_\perp} H_\parallel + \frac{J_{\mathrm{cyc}}}{J_\perp} H_{\mathrm{cyc}} \\
&= \sum_i \vec{S}_{i,l} \cdot \vec{S}_{i,r} + x \sum_{i;\tau} \vec{S}_{i,\tau} \cdot \vec{S}_{i+1,\tau} + x_{\mathrm{cyc}} H_{\mathrm{cyc}},
\end{aligned} \tag{5.1.1}
$$

where i denotes the rungs and $\tau \in \{l, r\}$ the left and right leg of the ladder (see Fig. 5.1.1). The quantities x and x_{cyc} are defined by

$$
x \;\; := \;\; J_\parallel/J_\perp \tag{5.1.2a}
$$

$$
x_{\mathrm{cyc}} \;\; := \;\; J_{\mathrm{cyc}}/J_\perp, \tag{5.1.2b}
$$

which will be the small expansion parameters for the PCUT. The four-spin ring exchange is given by

$$
\begin{aligned}
H_{\mathrm{cyc}} &= \sum_i \left[\left(\vec{S}_{i,l} \cdot \vec{S}_{i+1,l} \right) \left(\vec{S}_{i,r} \cdot \vec{S}_{i+1,r} \right) + \left(\vec{S}_{i,l} \cdot \vec{S}_{i,r} \right) \left(\vec{S}_{i+1,l} \cdot \vec{S}_{i+1,r} \right) \right. \\
&\qquad \left. - \left(\vec{S}_{i,l} \cdot \vec{S}_{i+1,r} \right) \left(\vec{S}_{i+1,l} \cdot \vec{S}_{i,r} \right) \right].
\end{aligned}
$$

These four-spin terms constitute the most important correction to the commonly considered nearest neighbor Heisenberg exchange. By now, this is established for planes

[67, 68, 69, 70] and ladders [71, 72, 73, 74, 65]. The size of J_{cyc} in cuprate ladders was found to be of the order 0.2-0.25 $J_{\perp}$ [75, 76, 77]. Further corrections like the two-spin interaction over the diagonal are almost one order of magnitude smaller [72] so that they are neglected in the following.

The physics of spin ladders is well understood in the limit of isolated rungs $\{x = 0, x_{\text{cyc}} = 0\}$. In this limit the ground state is the product state of singlets and the excitations are completely local triplets. The elementary excitations at finite values x and x_{cyc} are dressed triplets which are called triplons [66]. Triplon excitations are gapped and have a total spin one. In the following we will consider triplets on the rungs as local triplons.

It is natural to represent the rung states in terms of bond operators [78, 79, 80], because it has the advantage of making the connection to the lattice degree of freedom most direct [81]. In addition, the bond operator approach yields already a ground state and excitations with the correct quantum numbers using mean field theory [81], which allows to neglect strong fluctuation to capture the proper physics. Within this representation, the four-dimensional Hilbert space of each rung i of the ladder is given by the singlet

$$s_i^\dagger |0\rangle_i = |s\rangle_i = \frac{1}{\sqrt{2}} \left(|\uparrow\downarrow\rangle - |\downarrow\uparrow\rangle \right) \tag{5.1.4}$$

and the three triplet states

$$t_{-1,i}^\dagger |0\rangle_i = |t_{-1}\rangle_i = \frac{-1}{\sqrt{2}} \left(|\uparrow\uparrow\rangle - |\downarrow\downarrow\rangle \right) \tag{5.1.5}$$

$$t_{0,i}^\dagger |0\rangle_i = |t_0\rangle_i = \frac{i}{\sqrt{2}} \left(|\uparrow\uparrow\rangle + |\downarrow\downarrow\rangle \right) \tag{5.1.6}$$

$$t_{+1,i}^\dagger |0\rangle_i = |t_{+1}\rangle_i = \frac{1}{\sqrt{2}} \left(|\uparrow\downarrow\rangle + |\downarrow\uparrow\rangle \right). \tag{5.1.7}$$

The state $|0\rangle = \prod_i |0\rangle_i$ represents the completely empty system. This is actually an unphysical state which is needed here only for formal reasons.

The physically most important state is the ground state at $\{x = 0, x_{\text{cyc}} = 0\}$ which will be used as a reference state $|\text{ref}\rangle$ for our calculation. It is given by the product of singlets on all rungs

$$|\text{ref}\rangle := \prod_i |s\rangle_i. \tag{5.1.8}$$

One can also interpret $|\text{ref}\rangle$ as a singlet condensate, i.e. singlet operators can be replaced by unity $s = 1 = s^\dagger$. Physically, $|\text{ref}\rangle$ is the triplon vacuum, i.e., the state without any excitation.

The operator $t^\dagger_{\alpha,i}$ with $\alpha \in \{0, \pm 1\}$ creates an elementary excitation with $S^z = \alpha$ (flavor) when applied to a singlet state on rung i. Each rung is either occupied by a singlet or by a triplon, resulting in the so called *hardcore* constraint on all rungs i

$$\mathbb{1} = s^\dagger_i s_i + \sum_\alpha t^\dagger_{\alpha,i} t_{\alpha,i} \quad \alpha \in \{-1, 0, 1\} \tag{5.1.9}$$

for *hardcore* bosons, which implies particle-number conservation in terms of singlets *and* triplons.

In previous work [3, 2] the unitary transform of the spin operator components $S^{\mathrm{r}}_{i,\alpha}$ and $S^{\mathrm{l}}_{i,\alpha}$ is deduced from the PCUT method resulting in

$$\begin{aligned} S^{\mathrm{eff,r}}_{i,\alpha} &:= U^\dagger S^{\mathrm{r}}_{i,\alpha} U = \sum_m a_m(r) \left(t^\dagger_{i+m,\alpha} + t_{i+m,\alpha} \right) + \cdots \\ S^{\mathrm{eff,l}}_{i,\alpha} &:= U^\dagger S^{\mathrm{l}}_{i,\alpha} U = \sum_m a_m(r) \left(-t^\dagger_{i+m,\alpha} - t_{i+m,\alpha} \right) + \cdots , \end{aligned} \tag{5.1.10}$$

where the dots indicate that the normal-ordered quadratic and higher terms in bosonic operators have been neglected. Moreover only for this linear level in bosonic t-operators, the antisymmetry $S^{\mathrm{eff,l}}_{i,\alpha} = -S^{\mathrm{eff,r}}_{i,\alpha}$ holds because the triplet represents an odd excitation relative to the rung singlet with respect to reflection around the centerline of the ladder.

The Hamiltonian (5.1.1) can be reformulated in terms of the above bond operators. One finds

$$H = H_\perp + T_0 + T_{-2} + T_2 \tag{5.1.11}$$

where the index n in T_n indicates the change of the total triplon number, e.g., $T_{+2} \propto t^\dagger t^\dagger ss$ are pair creation processes and $T_{-2} \propto tts^\dagger s^\dagger$ are pair annihilation processes. In contrast, T_0 does not change the number of triplons in the system. This term includes triplon hopping processes $t^\dagger t s^\dagger s$ and two-triplon interactions $t^\dagger t^\dagger tt$. Note that we have omitted the spatial and flavor index here in order to keep the notation light. Finally, the operator $H_\perp$ counts the total number of triplons in the system.

The low-energy spectrum of spin ladders has been studied intensively [82, 38, 83, 84, 85, 86, 87, 88, 89, 90, 65]. All excitations can be classified by the parity with respect to reflections about the centerline of the spin ladder: an odd number of triplons has odd parity and an even number of triplons has even parity.

5.1.1 (P)CUTs

As already mentioned in Chapter 4 we apply the CUT in its perturbative version using the particle conserving generator η^{pc} from equation (4.3.5), i.e., the effective Hamiltonian for the two-leg ladder is obtained as a high-order series expansion in the small parameters x and x_{cyc}.

For the two-leg ladder we choose $Q = \frac{H_\perp}{J_\perp}$ giving an effective Hamiltonian which conserves the number of triplons, i.e., $[H_\perp, H_{\mathrm{eff}}] = 0$. Consequently, the effective Hamiltonian H_{eff} decomposes into a sum of *irreducible* n-triplon operators H_n

$$H_{\mathrm{eff}} = \sum_{n=0}^{\infty} H_n, \tag{5.1.12}$$

and each n-triplon block can be treated separately (see Ref.[28] for details).

The essential one-triplon dispersion $\omega(k)$ has already been determined earlier [65, 28]. The one-triplon hopping amplitudes ν_m have been calculated up to order 11 in both perturbative parameters. Various extrapolation schemes can be applied successfully [91]. Especially the low-energy part of the dispersion including the one-triplon gap can be determined very reliably up to realistic values $x \approx 1.25 - 1.5$ and $x_{\mathrm{cyc}} \approx 0.2 - 0.25$.

In order to calculate spectral properties of the system such as the dynamical structure factor $S_T(k, \omega)$ one has to transform observables O by the same CUT as the Hamiltonian. Hence the same generator η^{pc} in (4.3.5) is used in the flow equation

$$\partial_l O(l) = [\eta^{\mathrm{pc}}(l), O(l)]. \tag{5.1.13}$$

The relevant observable $O(r)$ with odd parity for the dynamical structure factor [65] is given locally on rung r by

$$O(r) = S^z_{r,1} - S^z_{r,2} = t^\dagger_{0,r} s_{0,r} + t_{0,r} s^\dagger_{0,r}. \tag{5.1.14}$$

The bare observable creates or destroys a single triplon with flavor 0 on rung r. After the CUT, the effective observable $O^{\mathrm{eff}}(r)$ comprises many channels reflecting the complicated nature of the interacting triplon problem. One finds

$$O^{\mathrm{eff}}(r) = U^\dagger O(r) U = \sum_{n,m} O^{\mathrm{eff}}_{n,m}(r) \tag{5.1.15}$$

where $O_{n,m}^{\text{eff}}(r)$ stands for a process where m triplons are annihilated and n are created. Thus $n, m \in \mathbb{N}_0$ with the constraint that the difference $n-m$ is an odd number reflecting the odd parity of the observable. At zero temperature, no triplons are present so that only the terms $O_{n,0}$ with n odd are relevant.

In first approximation we need the most relevant one-triplon contribution $O_{1,0}$ which is defined by the one-triplon spectral weights $a^2(k)$. The corresponding real space amplitudes have been calculated earlier up to order 10 [65]. Extrapolations of the low-energy part close to $k = \pi$ are reliable up to realistic values of x and x_{cyc}. The contributions $O_{n,0}$ with $n \geq 3$ are significantly smaller in weight than $O_{1,0}$.

At finite temperatures, also contributions $O_{n,m}$ with $m > 0$ matter. These contributions give rise to vertex corrections. We will argue below that the most relevant vertex correction for the finite temperature physics at low energies of the spin ladder is the contribution $O_{2,1}$. It comprises processes where a second triplon is created assuming another triplon is already present in the system due to thermal fluctuations. Thus we refer to these processes as *conditional excitation* processes.

We have determined this contribution up to order 9 in the perturbative parameters. For extrapolation, we used the method of internal variables [64]. Unfortunately, no reliable Padé or DlogPadé resummation on top of this extrapolation scheme succeeded, in contrast to the extrapolation of the one-triplon dispersion and the one-triplon spectral weights. Certainly, this fact reflects the more complicated nature of conditional excitations. Nevertheless, the extrapolation still yields reasonable quantitative values for the physical processes up to realistic values of x and x_{cyc}.

The most relevant low-energy excitation has odd parity corresponding to a single triplon. It is completely characterized by the one-triplon dispersion

$$\omega(k) = \nu_0 + 2 \sum_{m=1} \nu_m \cos(mk), \tag{5.1.16}$$

where k is the momentum along the ladder and the ν_m are the one-triplon hopping amplitudes, that have been determined via the PCUT. The dispersion takes a minimum at $k = \pi$ defining the one-triplon gap Δ. For the temperature evolution we are solely interested in one-triplon energies. Therefore, we do not discuss channels with more triplons. But we note that there are interesting interaction effects present in two-leg ladders leading to two-triplon bound and anti-bound states as well as pronounced continua in their response functions, for details see Ref.[65] and references therein.

The dynamical structure factor $S_T^{\alpha,\beta}(k,\omega)$ is the quantity of interest for inelastic neutron scattering experiments as already presented in Chapter 2. It is given by

$$S_T^{\alpha,\beta}(k,\omega) = \frac{1}{1 - e^{-\frac{\omega(k)}{T}}} \operatorname{Im} \chi_T^{\alpha,\beta}(k,\omega) \quad , \tag{5.1.17}$$

where

$$\chi_T^{\alpha\beta}(k,\omega) = i \int_{-\infty}^{\infty} e^{i\omega t} \sum_r e^{-ikr} \langle [S_r^\alpha(t), S_0^\beta(0)] \rangle \theta(t) \tag{5.1.18}$$

denotes the retarded dynamical susceptibility and the superscripts $\alpha, \beta \in \{\pm 1, 0\}$ correspond to the components of the spin. Since our model is SU(2) invariant, the only finite components of the dynamical structure factor are the diagonal ones ($\alpha = \beta$). We define

$$S_T(k,\omega) = S_T^{0,0}(k,\omega). \tag{5.1.19}$$

The dynamical structure factor at zero temperature is dominated by the one-triplon contribution [90, 65]. Theoretically, the general form of the one-triplon contribution (or more generically of any single mode (SM) approximation) reads

$$S_{T=0}^{\mathrm{SM}}(k,\omega) = a^2(k)\delta(\omega - \omega(k)), \tag{5.1.20}$$

where the prefactor $a^2(k)$ defines the one-triplon spectral weight as already introduced in Chapter 2 and which is known to be strongly peaked at the gap momentum $k = \pi$ [3].

5.2 Finite temperature approach

The effects of thermal fluctuations on the one-triplon contribution to the dynamical structure factor of the spin ladder are investigated. Physically, one expects that the triplon acquires a finite life-time upon heating. Then the δ-functions at zero temperature are replaced by resonances which are found to show asymmetric line-shapes [92].

Our approach is complementary. We do not describe the decay of triplons due to scattering with other thermally excited triplons, but we develop an effective single-mode approximation. That means that the one-triplon contribution to the dynamical structure factor is still given by a δ-function, but with temperature-dependent spectral weight. On the level of the triplon dynamics, this is less sophisticated than the approach by Essler and collaborators [93, 92, 94]. In contrast, we are able to efficiently incorporate vertex

corrections which are also relevant at finite temperatures. This leads to a temperature-dependent one-triplon spectral weight in our theory.

Now we concentrate on the vertex corrections which are relevant for the single-mode description of the finite-temperature dynamical structure factor. They give access to the effective temperature-dependent description of the dynamical structure factor at low energies.

5.2.1 Effective single-mode approximation

Our temperature-dependent theory results in an effective single-mode approximation. A single-mode contribution to the dynamical structure factor (see Eq. (5.1.20)) depends solely on the dispersion and on the spectral weight. The general expression reads

$$S_T^{\text{SM}}(k, \omega) = \frac{1}{1 - e^{-\frac{\omega_T(k)}{T}}} \, a_T^2(k) \, \delta(\omega - \omega_T(k)). \tag{5.2.1}$$

First, we discuss the temperature effects in the effective dispersion $\omega_T(k)$. Second, we incorporate vertex corrections in the spectral weights $a_T^2(k)$.

5.2.2 Effective dispersion

The one-triplon contribution is characterized at zero temperature by $\omega(k)$. In the PCUT calculation the fully-condensed singlet state $|\text{ref}\rangle$ with $\langle s^\dagger s \rangle = 1$ is used as the reference state. Hence no parameter $s < 1$ for the singlet occupation needs to be introduced as it was used previously to take the hardcore constraint into account [80, 38]. The CUT takes the hardcore constraint into account.

At finite temperatures, however, the situation is different. Even after applying the CUT there will be a finite occupation of triplons which lowers the singlet occupation. In analogy to the previous studies at zero temperature, we take this effect into account by introducing the mean-field parameter $s(T)$ defined as the condensate value $\langle s^\dagger \rangle = s$ with $s \in [0, 1]$. We stress the difference to previous studies [80, 38] where $s < 1$ was used to consider quantum fluctuations while we use this concept to consider thermal fluctuations. More complex expressions such as $s_j^\dagger s_i$ are reduced to s^2 which only takes their c-number part into account. Any operator effects are neglected.

Then the s-dependent effective one-triplon dispersion reads

$$\omega_T(k, s) = \nu_0 + s^2(T) 2 \sum_{m=1} \nu_m \cos(mk) \tag{5.2.2}$$

because each non-local hopping $t_{\alpha,j}^\dagger t_{\alpha,i}$ with $j \neq i$ implies the transfer of a singlet $s_i^\dagger s_j$. The local processes $t_{\alpha,j}^\dagger t_{\alpha,j}$ do not require such a renormalization.

To determine the temperature-dependent mean field parameter $s(T)$ it is inserted in the hardcore constraint Eq. (5.1.9) yielding

$$1 = s^2(T) + 3 \left\langle t^\dagger t \right\rangle (T). \tag{5.2.3}$$

Due to the spin symmetry the expectation values $\left\langle t_\alpha^\dagger t_\alpha \right\rangle (T)$ with $\alpha \in \{-1, 0, 1\}$ are independent of α resulting in the factor 3. So the average triplon occupation $\left\langle t^\dagger t \right\rangle (T)$ determines $s(T)$.

The average triplon occupation can be calculated by summing over all modes $\langle t_k^\dagger t_k \rangle$ in momentum space. At finite temperatures one has

$$\left\langle t_k^\dagger t_k \right\rangle = \frac{1}{Z} \text{Tr} \left(t_k^\dagger t_k e^{-\frac{H}{T}} \right) = \frac{\partial F}{\partial \omega_k} \tag{5.2.4}$$

where k is the triplon momentum. The free energy F is defined via the partition function Z by

$$F = -T \ln(Z) \tag{5.2.5}$$

where the Boltzmann constant k_{B} is set to unity. Integration over the whole Brillouin zone yields the wanted local triplon density

$$\left\langle t^\dagger t \right\rangle (T) = \int_{-\pi}^{\pi} \frac{\left\langle t_k^\dagger t_k \right\rangle}{2\pi} dk. \tag{5.2.6}$$

If the triplons were bosons without constraint $\left\langle t_k^\dagger t_k \right\rangle$ would be given by the standard bosonic occupation $(\exp(\omega(k)/T) - 1)^{-1}$. Unfortunately, there is no equivalent rigorous expression for hardcore bosons. For an approximate treatment we follow the arguments of Troyer et al. [95] to reweight the partition function Z yielding

$$\begin{aligned} Z &= Z_\omega^N \\ Z_\omega &:= 1 + \frac{3}{2\pi} \int_{-\pi}^{\pi} e^{-\frac{\omega_T(k,s)}{T}} dk \end{aligned}$$

where N is the number of rungs. Consequently, the free energy becomes

$$F = -NT \ln \left(1 + \frac{3}{2\pi} \int_{-\pi}^{\pi} e^{-\frac{\omega_T(k,s)}{T}} dk \right). \tag{5.2.8}$$

Combining Eqs. (5.2.8, 5.2.6, 5.2.3) yields

$$s^2(T) = 1 - \frac{3}{2\pi} \frac{1}{Z_\omega} \int_{-\pi}^{\pi} e^{-\frac{\omega_T(k,s)}{T}} dk. \tag{5.2.9}$$

Due to the dependence of the dispersion $\omega_T(k, s)$ on s the above equation defines s only implicitly. Hence, it has to be evaluated self-consistently. A study of the limits of $s(T)$ is given in Section 5.2.3.

For completeness, we mention another effect which implies a renormalization of the effective dispersion due to a finite concentration of thermally excited triplons. Triplon-triplon interactions of the type $t_1^\dagger t_2^\dagger t_3 t_4$ are known to exist. For instance, they lead to the occurrence of bound states [96, 90]. They also yield some renormalization of the dispersion upon mean-field decoupling

$$\begin{aligned}
t_1^\dagger t_2^\dagger t_3 t_4 &\approx \langle t_1^\dagger t_3 \rangle t_2^\dagger t_4 + \langle t_2^\dagger t_3 \rangle t_1^\dagger t_4 \\
&\quad + \langle t_1^\dagger t_4 \rangle t_2^\dagger t_3 + \langle t_2^\dagger t_4 \rangle t_1^\dagger t_3 + \text{const.,}
\end{aligned} \tag{5.2.10}$$

which is proportional to the triplon densities $\langle t^\dagger t \rangle (T)$. The inclusion of the above terms will renormalize the effective dispersion $\omega_T(k)$ slightly. We do not consider the effect of the terms in Eq. (5.2.10) here quantitatively for two reasons.

First, an estimate of the quantitative effect of these corrections indicates that they are not very significant. For instance, they are of the same order as the effect of the inclusion of the factor $s^2(T)$ in Eq. (5.2.2). If this term is omitted no qualitative changes of our results will occur because they are dominated by the renormalization of matrix elements, not by the renormalization of the energies as we will show in the following. Second, their systematic treatment is very tedious because a quantitative determination of all interaction elements would be required.

5.2.3 Temperature limits of the mean field parameter

Before we present the self-consistent numerical solutions of (5.2.9) we present an analytical estimate of the temperature limits of the mean field parameter $s^2(T)$. Therefore we estimate $\omega(k, s)$ to find an upper boundary. We know $\cos(x)$ is a bounded continuous function. Since $\omega(k, s)$ is a finite sum of bounded continuous functions, $\omega(k, s)$

itself is bounded and continuous leading to

$$\mid \omega(k,s) \mid \leq \mid t_0 \mid +s^2 2 \sum_{m=1}^{m<\infty} \mid \nu_m \mid =: g(s), \tag{5.2.11}$$

where we have used the triangle inequality repeatedly. Evaluating $g(s)$ yields a real number R such that $|g(s)| \leq R$ for all $s \in [0,1]$, since the sum in Eqs. 5.1.16 or 5.2.2 is finite due to the finite extension of the included hopping amplitudes. For the high temperature limit and the zero temperature limit we obtain respectively

$$\lim_{T\to\infty} \left(1 - \frac{3}{2\pi} \int_{-\pi}^{\pi} \frac{e^{-\frac{R}{T}}}{Z_R} dk \right)$$
$$= 1 - \frac{3}{4} = \frac{1}{4} \tag{5.2.12}$$

and

$$\lim_{T\to0} \left(1 - \frac{3}{2\pi} \int_{-\pi}^{\pi} \frac{e^{-\frac{R}{T}}}{Z_R} dk \right) = 1, \tag{5.2.13}$$

where Z_R in each case is given by replacing $\omega_T(k,s)$ in equation (5.2.7) by R. This estimate holds true as long as the dispersion satisfies $\omega(k,s) \geq 0$, which is the physically reasonable case. In summary, we get for $T \to 0$ a limit of 1 and for $T \to \infty$ a limit of $\frac{1}{4}$ independent of the choice of s. Physically this means, that we obtain a uniform distribution of all four states for infinite temperature and a full occupation by the singlet state at zero temperature as it is to be expected.

5.2.4 Vertex corrections and effective spectral weights

The second building block for the one-triplon contribution to the dynamical structure factor is the one-triplon spectral weight. Its unconditional part, active also at zero temperature, is contained in $O_{1,0}^{\text{eff}}$ after the CUT. It is illustrated diagrammatically in panel a) of Fig. 5.2.1. Contributions $O_{n,m}^{\text{eff}}$ with $m > 0$ are only active at finite temperatures; they represent conditional excitations. Our idea is to include such contributions as vertex corrections in an effective manner. We identify $O_{2,1}^{\text{eff}}$ as most important contribution because it requires only a single triplon to be present. It is illustrated diagrammatically

in panel b) of Fig. 5.2.1. Hence its quantitative contribution will be proportional to the triplon density. In second quantization $O_{2,1}^{\text{eff}}$ contains operators of the form $t_\alpha^\dagger t_\beta^\dagger t_\gamma$.

In contrast, any term of $O_{m+1,m}^{\text{eff}}$ with $m > 1$ requires the existence of m triplons so that its quantitative contribution will be proportional to the m-th power of the triplon density. In the regime of low temperatures not significantly larger than the spin gap each additional power in the triplon density stands for another additional exponentially small factor.

Restricting ourselves to the two parts $O_{m+1,m}^{\text{eff}}$ with $m \in \{0,1\}$, the effective observable is given by

$$
\begin{aligned}
O^{\text{eff}}(r) &= U^\dagger O(r) U \\
&\approx O_{1,0}^{\text{eff}}(r) + O_{2,1}^{\text{eff}}(r) \\
&= \sum_p \left(a_p t_{0,r+p}^\dagger + \text{h.c.} \right) + \sum_{\alpha,\beta,\gamma} \sum_{i<j,p} \left(a_{i,j,p}^{\alpha,\beta,\gamma} t_{\alpha,r+i}^\dagger t_{\beta,r+j}^\dagger t_{\gamma,r+p} + \text{h.c.} \right).
\end{aligned}
$$

The ordering of operators in the above equation is not unique. To avoid double counting, the convention $i < j$ is used. A few excitation processes appearing in $O_{2,1}^{\text{eff}}$ in low order in the small parameters are illustrated in Fig. 5.2.2.

Symmetries of the system imply further constraints. The conservation of the total S^z component for processes of the type $t_\alpha^\dagger t_\beta^\dagger t_\gamma$ leads to

$$
0 = \alpha + \beta - \gamma \qquad \alpha, \beta, \gamma \in \{0, \pm 1\}, \tag{5.2.14}
$$

where it is understood that the bare observable is given by Eq. (5.1.14).
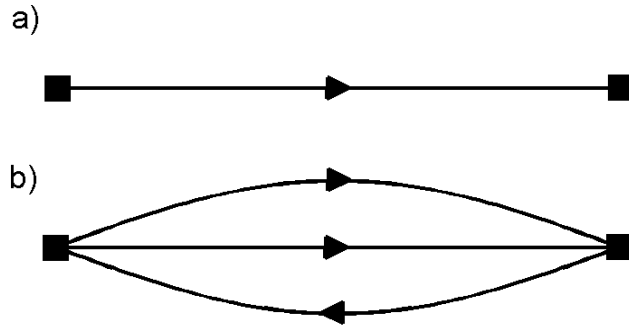

Figure 5.2.1: Propagation of the excitation included in the calculation. Diagram a) shows the *one triplon excitation*; diagram b) shows the *conditional triplon excitation* which requires the existence of a triplon.
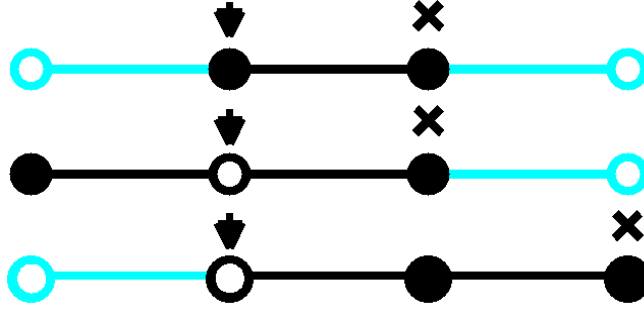
Figure 5.2.2: Some conditional excitation processes are sketched which are of linear order in x, as obtained from the results of the series expansions. The arrows indicate the rung on which the observable $O_{2,1}^{\text{eff}}(r)$ acts, whereas the cross **x** denotes the rung which is occupied by the one-triplon before the conditional excitation. Black filled circles denote the rungs occupied by triplons after the conditional excitation process. Open circles are in their singlet state after the excitation; the cyan part is shown for completeness.

For scattering experiments we are interested in the Fourier transform of $O^{\text{eff}}(r)$ in Eq. (5.2.14). For the unconditional contribution $O_{1,0}^{\text{eff}}$ we find

$$
\begin{aligned}
O_{1,0}^{\text{eff}}(k) &= \frac{1}{\sqrt{N}} \sum_r \mathrm{e}^{\mathrm{i}kr} O_{1,0}^{z,\text{eff}}(r) \\
&= \frac{1}{\sqrt{N}} \sum_{r,p} \left(\mathrm{e}^{\mathrm{i}kr} a_p t_{0,r+p}^\dagger + \mathrm{e}^{\mathrm{i}kr} a_p t_{0,r+p} \right) \\
&= \frac{1}{\sqrt{N}} \sum_{r,p} a_p \left(\mathrm{e}^{\mathrm{i}k(r-p)} t_{0,r}^\dagger + \mathrm{e}^{\mathrm{i}k(r-p)} t_{0,r} \right) \\
&= a(k) \left(t_{0,-k}^\dagger + t_{0,k} \right)
\end{aligned}
\tag{5.2.15}
$$

where we use

$$
a(k) := \sum_p \mathrm{e}^{-\mathrm{i}kp} a_p. \tag{5.2.16}
$$

Note that the coefficients a_p are real. For the symmetric spin ladder studied here they are also symmetric $a_p = a_{-p}$, so that $a(k)$ is also real. The operators $t_{0,k}^\dagger$ and $t_{0,k}$ are defined by

$$
t_{0,k} := \frac{1}{\sqrt{N}} \sum_r \mathrm{e}^{\mathrm{i}kr} t_{0,r} \tag{5.2.17a}
$$

$$
t_{0,k}^\dagger := \frac{1}{\sqrt{N}} \sum_r \mathrm{e}^{-\mathrm{i}kr} t_{0,r}^\dagger. \tag{5.2.17b}
$$

The complete treatment of the conditional excitation is complicated since it involves several sums and the resulting terms are not diagonal in momentum space. But we do not aim at the exhaustive description of the multi-particle response, but at the renormalization of the single-mode response. Therefore, we use a mean-field decoupling for $O_{2,1}^{\text{eff}}(k)$ to identify the processes belonging to the creation of a single triplon.

The mean-field decoupling is motivated by Wick's theorem, but represents an approximation here because the triplons are hardcore bosons. For concentrations of the triplons tending to zero, i.e., for $T \to 0$, the hardcore constraint becomes less and less effective and the use of Wick's theorem is justified

$$t_{\alpha,i}^{\dagger}t_{\beta,j}^{\dagger}t_{\gamma,p} \approx t_{\alpha,i}^{\dagger}\langle t_{\beta,j}^{\dagger}t_{\gamma,p}\rangle + t_{\beta,j}^{\dagger}\langle t_{\alpha,i}^{\dagger}t_{\gamma,p}\rangle. \qquad (5.2.18)$$

Due to the symmetry constraint Eq. (5.2.14) only for the cases

$$\begin{aligned}\langle t_{\beta,j}^{\dagger}t_{\gamma,p}\rangle \neq 0 &\quad \text{if} \quad \beta = \gamma \quad \text{and} \quad \alpha = 0 \\ \langle t_{\alpha,i}^{\dagger}t_{\gamma,p}\rangle \neq 0 &\quad \text{if} \quad \alpha = \gamma \quad \text{and} \quad \beta = 0\end{aligned} \qquad (5.2.19)$$

the expectation values do not vanish. In all other cases the expectation values are zero. We define the *hopping expectation values* by

$$\tau_T(j - p) := \langle t_{\beta,j}^{\dagger}t_{\beta,p}\rangle. \qquad (5.2.20)$$

Due to spin rotation symmetry this definition is independent of β, but depends on the relative distance of the two rungs j and p as depicted in Fig. 5.2.3. Consequently, we perform an index shift $(j - p) \to j$ yielding $\tau_T(j)$ which is used in the following.
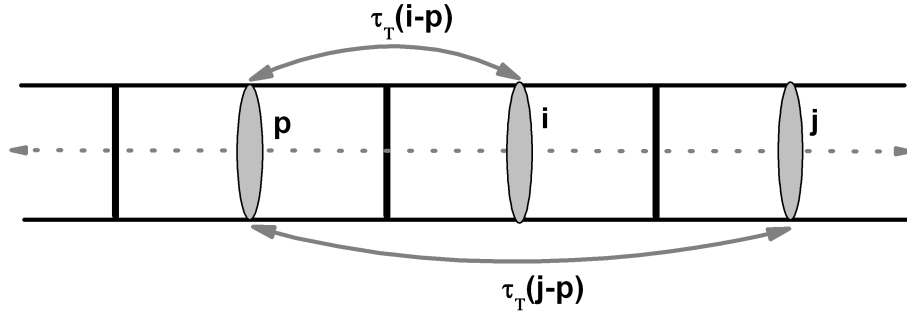

Figure 5.2.3: Illustration of the hopping expectation value $\tau_T(j - p)$ as defined in Eq. (5.2.20).

Employing the mean-field decoupling (5.2.18) renders the operator structure of $O_{2,1}^{\text{eff}}$ the same as for $O_{1,0}^{\text{eff}}$. Therefore, Fourier transformation makes it concise

$$
\begin{aligned}
O_{2,1}^{\text{eff}}(k) &= \frac{1}{\sqrt{N}} \sum_{r,i,j,p} \sum_{\alpha,\beta,\gamma} a_{i,j,p}^{\alpha,\beta,\gamma} \left(e^{ikr} t_{\alpha,r+i}^{\dagger} t_{\beta,r+j}^{\dagger} t_{\gamma,r+p} + e^{ikr} t_{\alpha,r+i} t_{\beta,r+j} t_{\gamma,r+p}^{\dagger} \right) \\
&\approx \frac{1}{\sqrt{N}} \sum_{r,i,j,p} \sum_{\beta} a_{i,j,p}^{0,\beta,\beta} \left(e^{ikr} t_{0,r+i}^{\dagger} \tau_T(j-p) \delta_{\beta,\gamma} + e^{ikr} t_{0,r+i} \tau_T(j-p) \delta_{\beta,\gamma} \right) \\
&\quad + \frac{1}{\sqrt{N}} \sum_{r,i,j,p} \sum_{\alpha} a_{i,j,p}^{\alpha,0,\alpha} \left(e^{ikr} t_{0,r+j}^{\dagger} \tau_T(i-p) \delta_{\alpha,\gamma} + e^{ikr} t_{0,r+j} \tau_T(i-p) \delta_{\alpha,\gamma} \right).
\end{aligned}
$$

Shifting the indices $r \to r - i$ and $j \to j + p$ in the first sum as well as $r \to r - j$ and $i \to i + p$ in the second sum leads to

$$
\begin{aligned}
O_{2,1}^{\text{eff}}(k) &= \tfrac{1}{\sqrt{N}} \sum_{r,i,j,p} \sum_{\beta} a_{i,j+p,p}^{0,\beta,\beta} \left(e^{-iki} e^{ikr} t_{0,r}^{\dagger} + e^{-iki} e^{ikr} t_{0,r} \right) \tau_T(j) \\
&\quad + \tfrac{1}{\sqrt{N}} \sum_{r,i,j,p} \sum_{\alpha} a_{i+p,j,p}^{\alpha,0,\alpha} \left(e^{-ikj} e^{ikr} t_{0,r}^{\dagger} + e^{-ikj} e^{ikr} t_{0,r} \right) \tau_T(i) \quad \text{(5.2.21)} \\
&\overset{(5.2.17)}{=} \sum_{i,j,p} \sum_{\beta} a_{i,j+p,}^{0,\beta,\beta} \left(t_{0,-k}^{\dagger} + t_{0,k} \right) e^{-iki} \tau_T(j) \\
&\quad + \sum_{i,j,p} \sum_{\alpha} a_{i+p,j,p}^{\alpha,0,\alpha} \left(t_{0,-k}^{\dagger} + t_{0,k} \right) e^{-ikj} \tau_T(i) \quad \text{(5.2.22)} \\
&= \sum_{i,j,p} \sum_{\alpha} \left(a_{j,i+p,}^{0,\alpha,\alpha} + a_{i+p,j,p}^{\alpha,0,\alpha} \right) \left(t_{0,-k}^{\dagger} + t_{0,k} \right) e^{-ikj} \tau_T(i).
\end{aligned}
$$

Finally the full effective observable $O^{\text{eff}}(k)$ in momentum space is given by

$$
\begin{aligned}
O^{\text{eff}}(k) &= O_{1,0}^{\text{eff}}(k) + O_{2,1}^{\text{eff}}(k) \\
&= [a(k) + A_T(k)] \left(t_{0,-k}^{\dagger} + t_{0,k} \right), \quad \text{(5.2.23)}
\end{aligned}
$$

where we used the definitions

$$
A_T(k) := \sum_i A_i(k) \tau_T(i) \quad \text{(5.2.24a)}
$$

$$
A_i(k) := \sum_j A_{i,j} e^{-ikj} \quad \text{(5.2.24b)}
$$

$$
A_{i,j} := \sum_{p,\alpha} \left(a_{j,i+p}^{0,\alpha,\alpha} + a_{i+p,j,p}^{\alpha,0,\alpha} \right). \quad \text{(5.2.24c)}
$$

Clearly, (5.2.23) shows that the conditional excitations imply a renormalization of the spectral weight of the triplons which are the single-mode excitations for the spin ladder. The temperature dependence of $A_T(k)$ stems from the temperature dependence of the

hopping expectation values $\tau_T(j)$. Similar to the calculation of the triplon occupation in (5.2.6), the hopping expectation values result from the suitably weighted averages over the Brillouin zone

$$\tau_T(j) = \frac{1}{2\pi Z_\omega} \int_{-\pi}^{\pi} e^{-\frac{\omega_T(k)}{T}} \cos(jk) dk. \qquad (5.2.25)$$

The expressions (5.2.24) for the effective spectral weights hold for all momenta k. But the main effect in the spectral weight is measured at the lowest excitation energy $\omega(\pi)$, i.e., at the momentum $k = \pi$. Hence we restrict ourselves to $k = \pi$ in the following. For $A_i(\pi)$ we obtain explicitly

$$A_i(\pi) = \sum_{p,j} (-1)^j \left(a_{j,i+p,p}^{0,0,0} + a_{i+p,j,p}^{0,0,0} + 2 \left(a_{j,i+p,p}^{0,1,1} + a_{i+p,j,p}^{1,0,1} \right) \right), \quad (5.2.26)$$

where the factor 2 comes from the fact that $a_{j,i+p,p}^{0,1,1} = a_{j,i+p,p}^{0,-1,-1}$ and $a_{j,i+p,p}^{1,0,1} = a_{j,i+p,p}^{-1,0,-1}$, respectively.

Adding the unconditional and the conditional excitation processes yields the total effective temperature-dependent one-triplon spectral weight at $k = \pi$

$$a_T^2(\pi) = \left[a(\pi) + A_T(\pi) \right]^2 s^2(T). \qquad (5.2.27)$$

The factor $s^2(T)$ stands for the reduced availability of rungs for the creation of triplons if there are already some thermally excited. Putting all pieces together we gain the expression (5.1.20) for the single-mode approximation of the dynamical structure factor at finite temperatures

$$S_T^{\mathrm{SM}}(k,\omega) = a_T^2(k)\delta(\omega - \omega_T(k)), \qquad (5.2.28)$$

which we use in the present work for $k = \pi$ only. This is the dynamic structure factor in single-mode approximation of the dynamical structure factor including the vertex corrections relevant at finite temperatures. The physical content of Eq. (5.2.28) will be exploited in the next section.

5.3 Theoretical results

Next we present our theoretical results obtained by extending the PCUT result to finite temperature using the MF approach. We demonstrate that the intensity decrease in the dynamical structure factor mainly arises from the contribution of the conditional excitations. The basic energy unit in this theory section is chosen to be the rung coupling
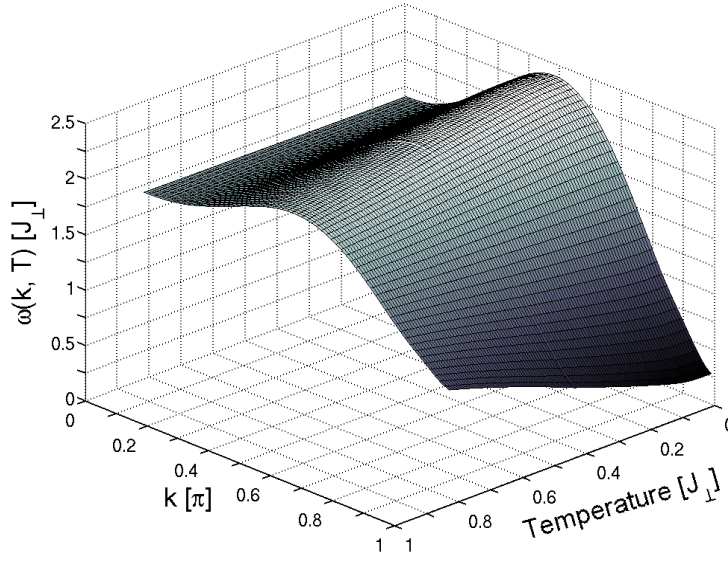
Figure 5.3.1: Effective mean-field dispersion for $x_{\mathrm{cyc}} = 0.2$ and $x = 1.5$ in dependence on temperature and momentum.

constant $J_\perp$ allowing for direct comparison for different parameter sets $\{x, x_{\mathrm{cyc}}\}$.

In Ref. [77] the parameters $x = 1.5$ and $x_{\mathrm{cyc}} = 0.2 - 0.25$ were determined to describe a generic cuprate spin ladder best. Thus we chose these parameters to compute the dependence of the self-consistent MF dispersions shown in Fig. 5.3.1 with temperature T and wave-vector k. This provides information on how the shape of the effective dispersion changes upon increasing temperature and momentum. The dispersion becomes flatter on increasing temperature implying a larger energy gap $\Delta(T) := \omega(\pi, T)$.

Figure 5.3.2 shows the gap as a function of temperature in units of $J_\perp$ for various $x = \{0.75, 1, 1.25, 1.5\}$ and a different x_{cyc} in each panel. The red dots in each panel indicate a characteristic temperature T_{char} above which the energy gap shows a significant dependency on temperature in form of a steep gap function $\Delta(T)$ for all x and x_{cyc}. The value of T_{char} scales with the spin gap $\Delta(T = 0)$; hence it decreases with increasing x_{cyc}.

Three further striking points are to be mentioned. First, with increasing x_{cyc} the curves for $x = \{0.75, 1, 1.25, 1.5\}$ approach one another until they lie almost on top of one another for $x_{\mathrm{cyc}} = 0.15 - 0.2$. For $x_{\mathrm{cyc}} = 0.25$ they start to spread again. Second, with
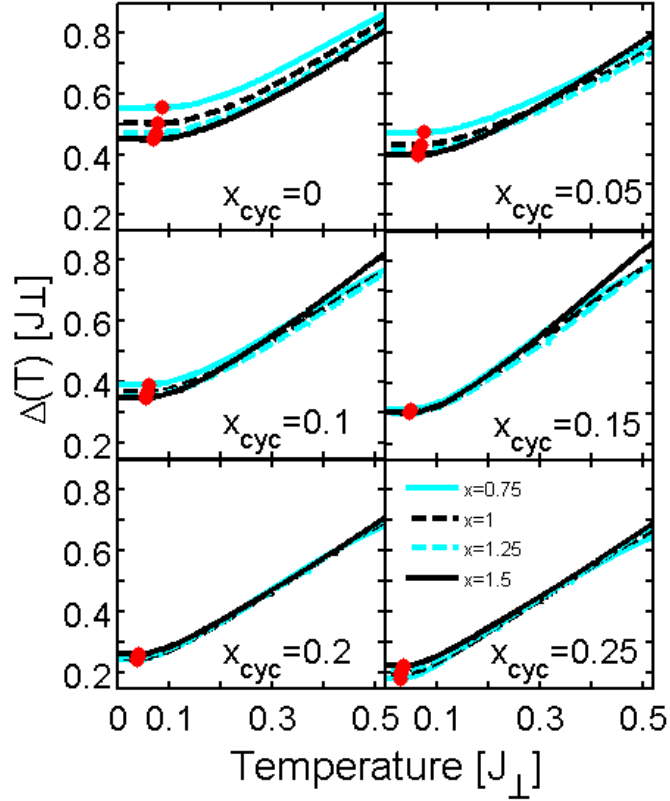
Figure 5.3.2: Excitation gap vs. temperature T for $x = \{0.75, 1, 1.25, 1.5\}$ and a different x_{cyc} in each panel. The red dots indicate the position of the characteristic temperature T_{char}.

increasing x_{cyc} the sequence of the curves in each panel changes from $0.75, 1, 1.25, 1.5$ to $1.5, 1.25, 1, 0.75$ from top to bottom. Third, the energy gap Δ decreases on increasing x_{cyc}.

Furthermore, it is interesting how much the average singlet state occupation number $s^2(T)$ changes with temperature. Its behaviour is illustrated in Fig. 5.3.3. Below the characteristic temperature T_{char} the occupation number $s^2(T)$ is almost independent on temperature for all x_{cyc} resulting from the almost constant gap energy $\Delta(T)$. Clearly, T_{char} scales with the energy gap $\Delta(0)$. Above T_{char} the occupation number $s^2(T)$ falls off the steeper the smaller x for a given value of x_{cyc}.

The generic behaviour of the MF triplon hopping expectation values $\tau(j)$ is depicted in Fig. 5.3.4 (upper panel) for $j = \{0, \cdots, 6\}$ vs. temperature for $x = 1.5$ and $x_{\mathrm{cyc}} = 0.2$.
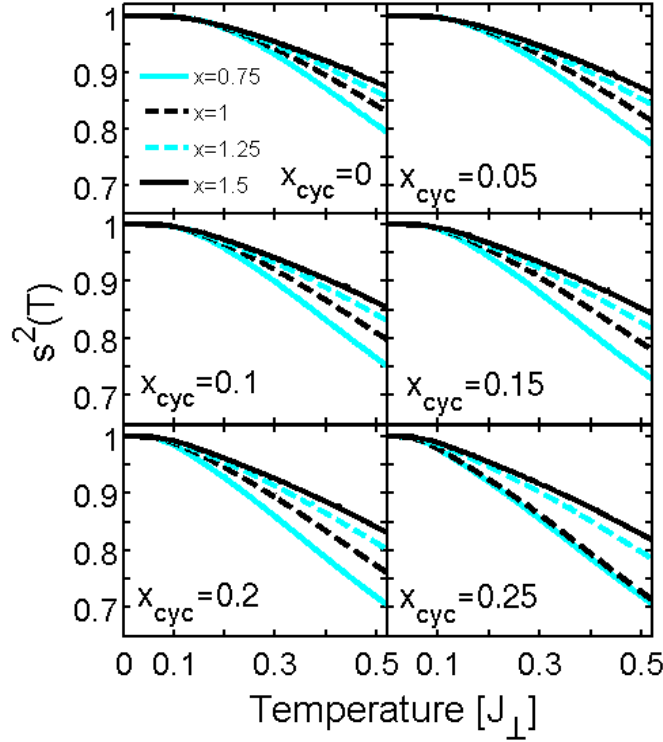
Figure 5.3.3: The dependence of the average singlet state occupation number $s^2(T)$ with temperature for various $x = \{0.75, 1, 1.25, 1.5\}$ with a different x_{cyc} in each panel.

For all other pairs of x and x_{cyc} the hopping expectation values look very similar. The associated conditional MF spectral weight $A(\pi, T)$ is shown in the bottom panel of Fig. 5.3.4. Thus, the shape of $A_\pi(T)$ is dominated by $\tau(j)$ with $j \geq 1$ explaining the minimum in $A_\pi(T)$ at about $T = 0.514 J_\perp$ which is about twice the spin gap $\Delta(0)$. [1]

The zero temperature one-triplon spectral weight $a^2(\pi)$ at the spin gap energy vs. x for $x_{\text{cyc}} = \{0, 0.05, 0.1, 0.15, 0.2, 025\}$ is shown in Fig. 5.3.5. With increasing x the one-triplon spectral weight at π grows. This increasing weight on increasing x confirms the conclusion, that the most important contribution to the one triplon weight and to the conditional triplon excitation weight is found at $k = \pi$. This is the dominant feature in the dynamic structure factor.

Fig. 5.3.6 depicts the conditional MF triplon spectral weight $A(\pi, T)$ obtained for various $x = \{0.75, 1, 1.25, 1.5\}$ and different values x_{cyc} vs. temperature. The conditional

---

[1]This value corresponds to about 630K for $J \perp = 105.5 \text{meV}$ in order to provide a first quantitative link to experiment. This temperature corresponds to about twice the spin gap found in Ref. [77].
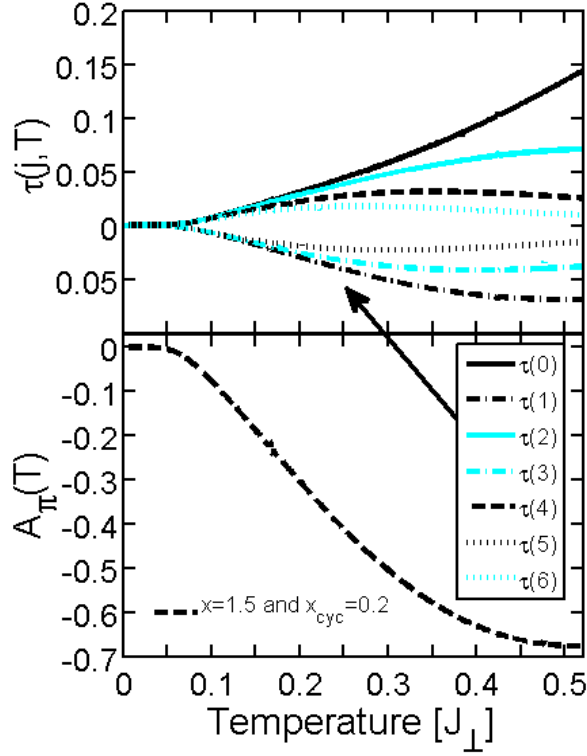
Figure 5.3.4: The upper panel shows the MF triplon hopping expectation value $\tau(j)$ for $j = \{0, \ldots, 6\}$ with $x = 1.5$ and $x_{\mathrm{cyc}} = 0.2$. The lower panel depicts the associated conditional MF spectral weight $A(\pi, T)$.

MF triplon weight for various x shows the expected almost constant behaviour below the characteristic temperature T_{char} where all curves lie indistinguishably on top of one another. Above T_{char} a steep fall-off is found. The steepness is affected by the values of x and x_{cyc}. The fall-off is the larger the larger x and x_{cyc} are. For fixed x_{cyc} the fall-off becomes stronger on increasing x.

The calculated conditional MF amplitude $A(\pi, T)$ displays a minimum at about $J_\perp/2$ which corresponds to about twice the spin gap $\Delta(0)$. We do not see any physical reason why the weight should increase again. Furthermore, the justification for the approximations involved is less sound beyond temperatures of about $2\Delta(0)$. Life time effects of the modes are expected to become more and more important [93, 92, 94] so that we do not expect the the calculated data to be reliable for temperatures beyond $J_\perp/2$.

The negative conditional MF amplitude $A(\pi, T)$ diminishes the one-triplon spectral weight $a_T(k)^2$ according to Eq. (5.2.27) yielding the normalized momentum-integrated
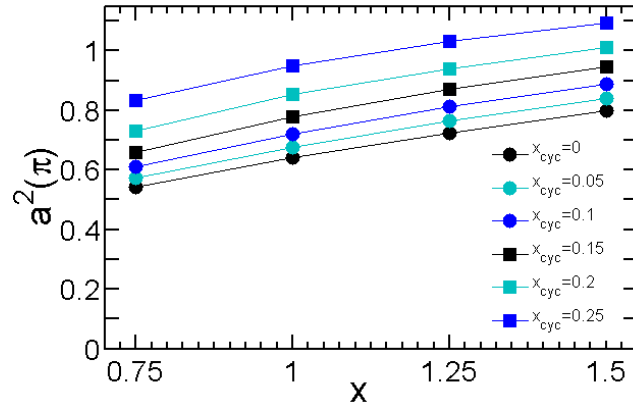
Figure 5.3.5: One-triplon spectral weight at $k = \pi$ where the the spin gap $\Delta(0)$ occurs for $T = 0$ vs. x for various x_{cyc}. The one-triplon spectral weight at $k = \pi$ increases on increasing x for fixed x_{cyc}. For fixed x the one-triplon spectral weight increases also on increasing x_{cyc}.
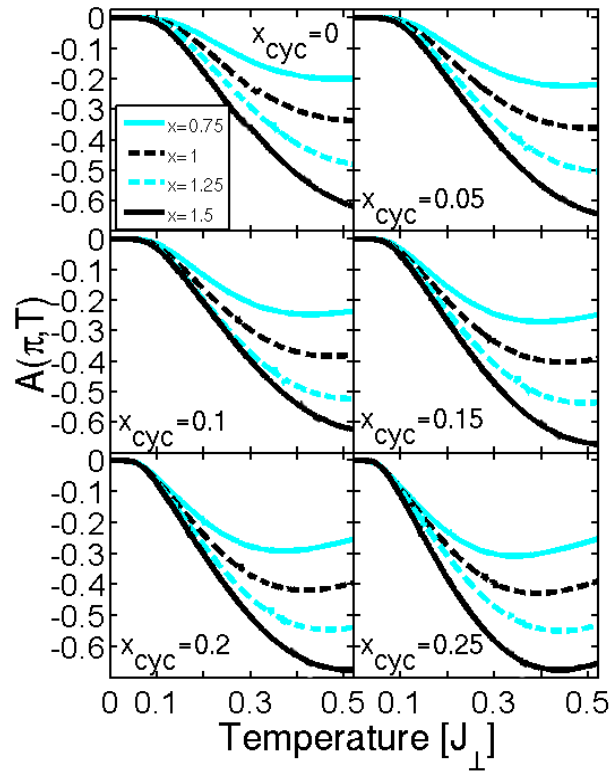

Figure 5.3.6: Conditional MF spectral weight vs. temperature T for $x = \{0.75, 1, 1.25, 1.5\}$ and different x_{cyc} in each panel.

structure factor $\frac{I(T)}{I_0}$ presented in Fig. 5.3.7. This is the experimentally relevant quantity. The shape of the normalized momentum-integrated structure factor $\frac{I(T)}{I_0}$ in Fig. 5.3.7 is very similar to the one of the conditional MF spectral weight in in Fig. 5.3.6 confirming that the conditional excitation process is the dominating effect on increasing temperature. This fact demonstrates the importance of vertex corrections in strongly correlated systems.
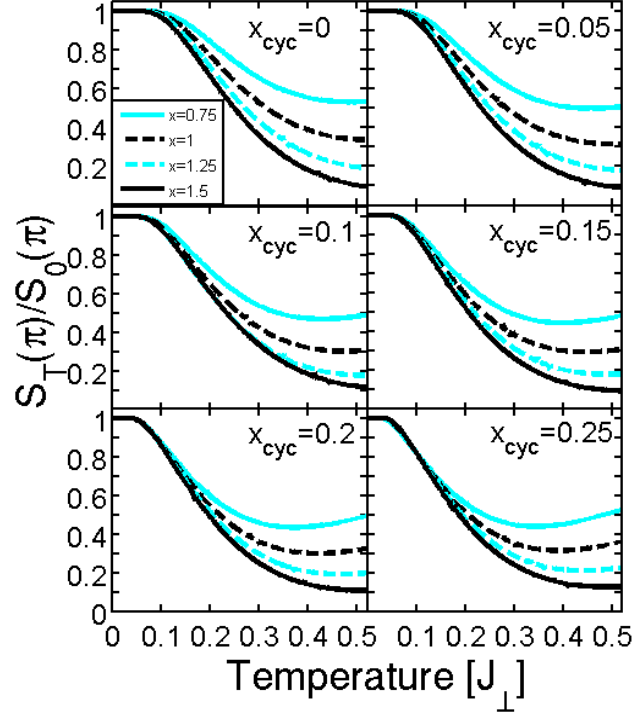

Figure 5.3.7: The momentum integrated dynamic structure factor $I(T) = \int S(k,T) \mathrm{d}k$ for $x = \{0.75, 1, 1.2, 1.5\}$ with a different x_{cyc} in each panel is presented. It is plotted vs. temperature, normalized to the momentum integrated dynamic structure factor $I_0 = \int S(k,0) \mathrm{d}k$ at zero temperature.

5.4   Comparison to experiment

In an inelastic neutron scattering experiment the dynamical structure factor is measured by the intensity of the scattered neutrons. In order to compare with theory a series of measurements were made on a cuprate spin ladder at different temperatures T. These measurements reveal the temperature development of the structure factor.

So far we discussed the theoretical results relative to the energy scale given by the coupling constant $J_\perp$. In order to compare to experimental data, we have to determine this energy scale. For each pair $\{x, x_{cyc}\}$ the coupling constant $J_\perp$ is determined from the experimental spin gap $\Delta(T = 0) = 27.6\text{meV}$ [97, 77]. The obtained values of $J_\perp$ are shown in Fig. 5.4.1 as functions of x (left panel) and of x_{cyc} (right panel). A striking
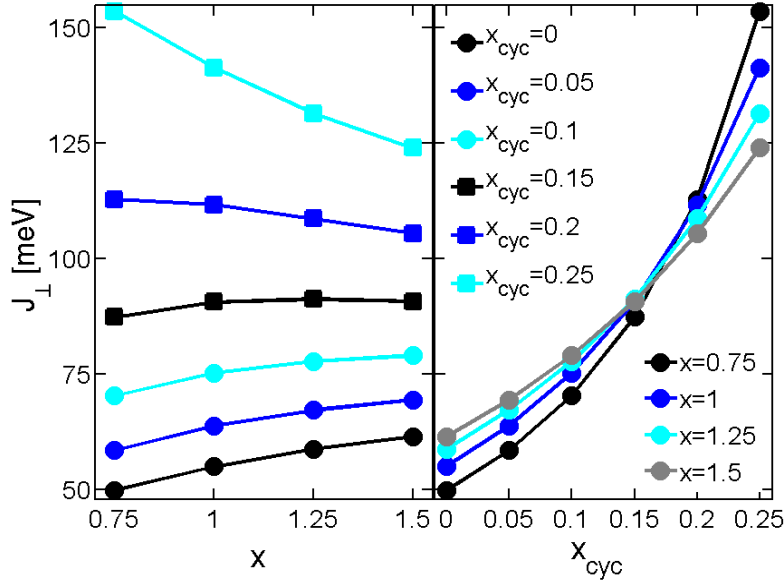

Figure 5.4.1: Rung coupling constants $J_\perp$ vs. x (left panel) and vs. x_{cyc} (right panel) determined from the experimental energy gap $\Delta(0) = 26.4\text{meV}$ found in Ref. [77].

point is found in the right panel of Fig. 5.4.1 where the for $x_{cyc} = 0.15$ the value of $J_\perp$ is nearly the same for all x. The sequence of the curves for various values of x changes at $x_{cyc} = 0.15$, i.e., for lower x_{cyc} the curves rise on rising x while they fall for larger x_{cyc}. Thus the curve for $x_{cyc} = 0.15$ in the left panel of Fig. 5.4.1 is almost flat.

5.4.1 Sample and INS experiments

Single crystals of $La_4Sr_{10}Cu_{24}O_{41}$ were grown using the 'traveling solvent floating zone' method [98] at 9 bar oxygen pressure. INS measurements were performed on the undoped ladder, $La_4Sr_{10}Cu_{24}O_{41}$ using the MAPS time-of-flight spectrometer at ISIS, Rutherford Appleton Laboratory, U.K. The sample consisted of three co-aligned single crystals with a total mass of 23g (see Ref.[77] for details). The crystals were mounted in a closed cycle cryostat with the $(0kl)$ reciprocal lattice plane horizontal and the c

axis perpendicular to the incident neutron beam k_i. A Fermi chopper was used to select an incident neutron energy of 100meV and 50meV and was rotated at a speed of 300 Hz to give an energy resolution at the elastic line of 4.1meV and 1.6meV, respectively. Close to the gap, at an energy transfer of 30meV the energy resolution is 3.06meV and 0.93meV at an incident neutron energy of 100meV and 50meV, respectively. Data were collected at temperatures of 15K, 50K, 100K, and 150K, and of 15K, 50K, and 150K with an incident energy of 100meV and 50meV, respectively. Incoherent nuclear scattering from a vanadium standard was used to normalize the magnetic cross-section. In the following text wave vectors Q_c and Q_a represent the direction along the ladder and along the rung respectively.

5.4.2   Background subtraction and data analysis

The ladder signal was extracted by taking a constant-Q cut at $Q_c = 0.5$ and $Q_a = 1.2$ (wave vector ranges $0.45 < Q_c < 0.55$ and $0.9 < Q_a < 1.5$) where Q_c and Q_a are given in units of $2\pi/c$ and $2\pi/a$, respectively. The wave vector $Q_c = 0.5$ corresponds to the position of the gap and the Q_a range is chosen to maximise the ratio of magnetic intensity to background due to the rung modulation which goes as $\approx (1 - \cos(Q_a d_{\mathrm{rung}}))$, where d_{rung} is the rung distance. The background was determined from a constant-Q cut for the wave vector range $-0.2 < Q_c < 0.2$, and $0.9 < Q_a < 1.5$. This range is appropriate for the determination of the background, because it contains no magnetic scattering due to the ladder structure factor. Each temperature run was treated in exactly the same way, yielding the data shown in Fig. 5.4.2.

The highest intensity was measured for the coldest run at 15K. The experiment does not reveal any temperature dependence between 15K and 50K. A slight decrease in intensity is observed for 100K and a significant decrease for 150K. The spin gap is found to be at $\Delta = (30 \pm 0.5)$meV, which lies a little lower than that found in Refs. [99] and [100] and a little higher than found in Ref. [77]. Here we define the gap as the energy below the intensity maximum where scattering strength is half of its maximum value.

The FWHM of the observed peak was extracted by fitting a Gaussian to the data. Because the real shape of the measured curve deviates from the ideal Gaussian, the fit is adjusted such that the Gaussian and the data points with an energy below the energy of the maximum intensity match each another. The FWHM values are found to be
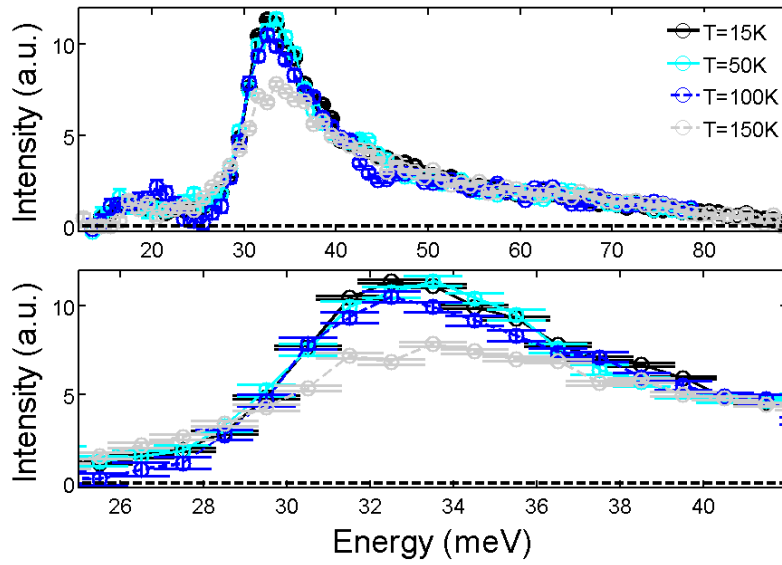
Figure 5.4.2: Background subtracted ladder signals measured at various temperatures extracted from INS measurements on $La_4Sr_{10}Cu_{24}O_{41}$. The lower panel represents a zoom of the top panel.

5.3 ± 0.5meV for 15K, 5.1 ± 0.5meV for 50K, 5.3 ± 0.5meV for 100K and (8 ± 0.5)meV for 150K for an incident energy of 100meV and 3.3 ± 0.5meV for 15K, 3.5 ± 0.5meV for 50K and (5.8 ± 0.5)meV for 150K for an incident energy of 50meV.Different FWHM values obtained for data collected at the same temperature but different incident energies was due to changes in the energy resolution.

A broadening effect due to damping could therefore only be observed at 150K. This result confirms that the broadening with increasing temperature is small in comparison to the intensity decrease with increasing temperature, which in turn validates the MF approach presented here. Strikingly the experimental intensity curves in Fig. 5.4.2 lie exactly on top of each other above 40meV for all measured temperatures, indicating there is a temperature independent contribution that results presumably from the wave vector resolution.

The data is compared to the theoretical spectral weight of the dynamical structure factor $S(\Delta(T))$ with increasing temperature described previously. To determine the relative changes we exclusively used the intensity signal in the range $28 \leq \omega \leq 40$meV and calculated the integrated intensities normalized by the area obtained from the 15K run. Fig. 5.4.3 shows the comparison between theory and experiment for the temperature
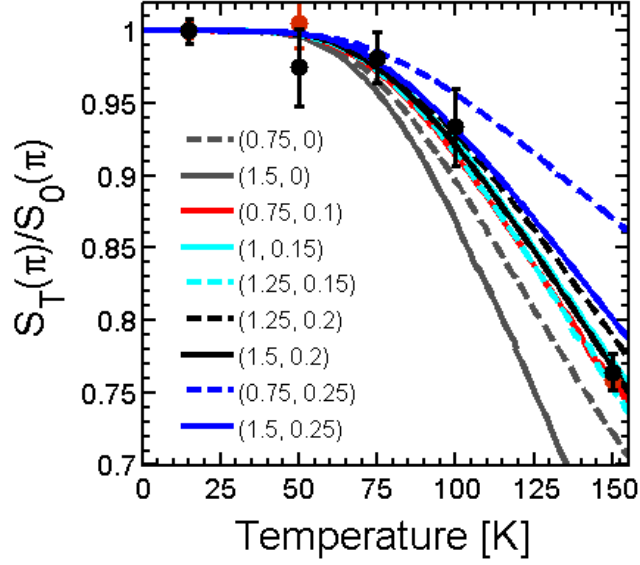
Figure 5.4.3: Temperature dependence of normalized dynamic structure factor $\frac{S_T(\pi)}{S_0(\pi)}$ at $k = \pi$ for various pairs of (x, x_{cyc}). The energy scale is set by $J_\perp$ given in Tab. 5.1. The black and red (gray) dots with error bars depict the experimental result obtained from INS for 100meV and 50meV, respectively.

dependent changes of the normalized integrated intensities. The temperature scale is restricted to the temperature region that has been probed experimentally. Possible pairs of (x, x_{cyc}) matching the INS data are

$$\{(0.75, 0.1), (1, 0.15), (1.25, 0.15), (1.5, 0.2)\}.$$

However, previous INS measurements [77] and optical conductivity measurements [101, 65] showed, that values of $x \approx 1.25 - 1.5$ and $x_{\mathrm{cyc}} \approx 0.20 - 0.27$ are realistic. To be consistent with previous experimental results we argue that the best agreement within the experimental error bars is found for $x = 1.5$ and $x_{\mathrm{cyc}} = 0.2$ (black solid curve).
In Ref. [77] $x = 1.5$ and $x_{\mathrm{cyc}} = 0.25$ with $J_\perp = 124$meV were fitted to the one-triplon dispersion extracted from experiment. This little discrepancy in x_{cyc} does not really matter because of the experimental errors and the approximation necessary for computing $A(\pi, T)$. Furthermore, if slightly different energy gaps are assumed, such as $\Delta = 35$meV (found in Refs. [99] and [100]), $\Delta = 30$meV (present work) and $\Delta = 27.6$meV (resulting from a theoretical re-analysis of the data from Ref. [77] [2]),

---

[2]This agrees with the published value of 26.4meV within the experimental resolution.

(x, x_{cyc})	$J_\perp[\mathrm{meV}]$
$(0.75, 0)$	54.2
$(1.5, 0)$	66.8
$(0.75, 0.1)$	76.4
$(1, 0.15)$	98.4
$(1.25, 0.15)$	99.1
$(1.25, 0.2)$	118
$(1.5, 0.2)$	115
$(0.75, 0.25)$	166.8
$(1.5, 0.25)$	135

Table 5.1: Values of the coupling constant $J_\perp$ based on a spin gap of $\Delta = 30\mathrm{meV}$ for the various pairs of (x, x_{cyc}) for which data is presented in Fig. 5.4.3
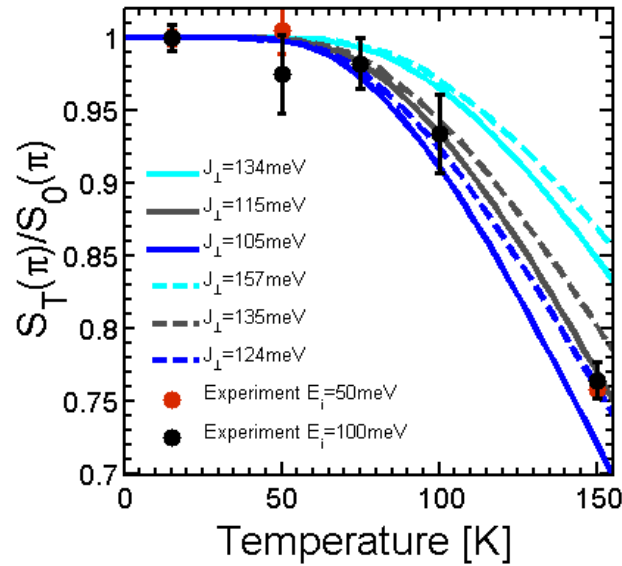

Figure 5.4.4: Normalized spectral weight based on different spin gaps ($\Delta = 35\mathrm{meV}$ (cyan lines), $\Delta = 30\mathrm{meV}$ (dark grey lines), and $\Delta = 27.6\mathrm{meV}$ (blue lines)) is shown. Dashed lines rely on $(x, x_{\mathrm{cyc}}) = (1.5, 0.25)$ and solid lines on $(x, x_{\mathrm{cyc}}) = (1.5, 0.2)$. The black and red dots with error bars depict the experimental result obtained from INS for 100meV and 50meV, respectively.

slightly different results are implied as presented in Fig. 5.4.4. Both a gap of 30meV and of 27.6meV match the data for realistic parameters (x, x_{cyc}). In fact, using the spin gap 27.6meV consistent with the data from Ref. [77] leads to convincing agreement with the values for (x, x_{cyc}) found in Ref. [77] to fit the INS data. Hence our findings in this work are fully consistent with previous results.

At about half the spin gap energy $\Delta(0)$ our MF theory of vertex corrections predicts a decrease of the spectral weight by 25% for $x = 1.5$ and $x_{\text{cyc}} = 0.2$ with $J_\perp = 115$meV which agrees very nicely with experiment, see Fig. 5.4.4. We stress that a decrease of 25% is well in the regime where we consider our approach valid and reliable.

Note, however, that we omitted the line broadening due to thermal fluctuations in the present analysis which play a more and more important role on increasing temperature. In particular, the unique experimental determination of the weight becomes increasingly difficult at higher temperatures.

5.5   Conclusions

We derived vertex corrections in the dynamic structure factor for a quantum antiferromagnet without long range order. The model system investigated is the two-leg spin ladder. The vertex corrections are linked to thermal fluctuations; they are relevant only at finite temperatures. We computed them in the framework of continuous unitary transformations which lead to an effective description of the system in terms of hardcore triplons as elementary excitations.

The vertex corrections are evaluated on the mean-field level, i.e., on the level of a single-model approximation. We found that they induce conditional excitation process which *reduce* the unconditional, zero-temperature excitation amplitude. Thereby, the spectral weight of the low-lying excitations is diminished because its temperature dependence is indeed found to be dominated by the vertex corrections. The vertex corrections stem eventually from the hardcore character of the triplons. Yet we emphasize that they go beyond the obvious mechanism that no triplon can be excited if its site is already excited by another triplon.

We compared the calculated spectral weight quantitatively with the one measured in the undoped ladder $La_4Sr_{10}Cu_{24}O_{41}$ using inelastic neutron scattering for a range of temperatures up to $150K$, equivalent to half the spin gap energy. The theory should still apply to considerably higher temperatures as long as these stay below twice the spin gap energy. Experiments at higher temperatures for undoped ladders could test this framework further.

Chapter 6

Two-dimensionality of coupled spin-$\frac{1}{2}$ ladders

In this Chapter the coupling of isolated antiferromagnetic (AF) spin-$\frac{1}{2}$ ladders is discussed. Several methods have been applied to study the influence of a non zero coupling between isolated ladders and lattices, which were mainly performed at zero temperature. Two geometries are of special interest - the square lattice and the trellis lattice, because both of them are realized in cuprates.

For example Matsuda et al. [37] studied the $S = \frac{1}{2}$ two-dimensional quantum Heisenberg antiferromagnet on the anisotropic dimerized square lattice using the quantum Monte Carlo method. Their findings include a closing of the spin gap for an inter-ladder coupling of $x_{\mathrm{inter}} = 0.314$, where $x_{\mathrm{inter}} = \frac{J_{\mathrm{inter}}}{J_{\perp}}$ denotes the ratio of inter-ladder coupling strength and the strength of the coupling along the rungs. Dagotto et al. [35] discussed an electronic model consisting of two chains or planes, each described by a $t - J$ model, coupled by $t' - J'$ interaction between them [35]. Their investigations also include the spin gap for the undoped coupled planes. Using Lanczos techniques they suggested that the spin gap opens for $J_{\perp} = J_{\parallel}$ [35]. The $t - J$ model was also investigated on coupled ladders in the presence of frustration by Riera an Dalosto [36] using various numerical techniques like quantum Monte Carlo (QMC) and exact diagonalization. They computed dynamical properties for the undoped and the doped case. Their findings include incommensurate peaks in the magnetic structure factor at low temperature [36] in the undoped case and a destruction of hole pairs with increasing inter-ladder coupling for

the doped case [36].

A mean field treatment with self-energy corrections of double ladders and of a periodic array of ladders by Gopalan et al. [38] results in a vanishing spin gap for an inter-ladder coupling of $x_{\mathrm{inter}} \approx 0.25$ in the square lattice case. For the trellis lattice they find an enhancement of the spin gap with increasing inter-ladder coupling x_{inter}.

Uhrig et al. [2] presented results for the coupling in the single layer and bilayer ladder plane. In Refs. [3] and [4] Uhrig and Schmidt treated the square lattice and the trellis lattice respectively. They stressed, that the hardcore property of the triplons is only taken into account along the ladders [4].

Starting from the well understood isolated Heisenberg spin-$\frac{1}{2}$ ladder the inter-ladder coupling of isolated ladders is in the following treated using the PCUT method combined with a mean field approach. This approach is performed analogously to our investigation of the temperature dependence in Chapter 5, except that conditional excitations are not taken into account. This time, however, the mean field approach is performed in two dimensions. We will discuss the effect of an inter-ladder coupling at zero and finite temperatures. As in Refs. [3] and [4] the calculations are performed for different underlying lattice geometries - the square lattice and the trellis lattice. The latter one is of special interest, because the trellis lattice reflects the real nature of the cuprate compounds $A_{14}Cu_{24}O_{41}$ [4] investigated in this thesis.

6.1   Model of coupled ladders

The approach employed in the following for both kinds of underlying lattice couplings starts from the effective model that has been derived for the isolated ladder in Refs. [90] and [65] and that has been already applied in Chapter 5. The two situations treated in the following are sketched in Fig. 6.1.1, where the square lattice coupling with only one lattice constant a represents an in-line coupling (left side) and the trellis lattice coupling a $\frac{c}{2}$-shifted coupling (right side). In the latter case c is the second lattice constant along the ladder direction and a represents the lattice constant along the rungs. The Hamiltonian describing such couplings is given by

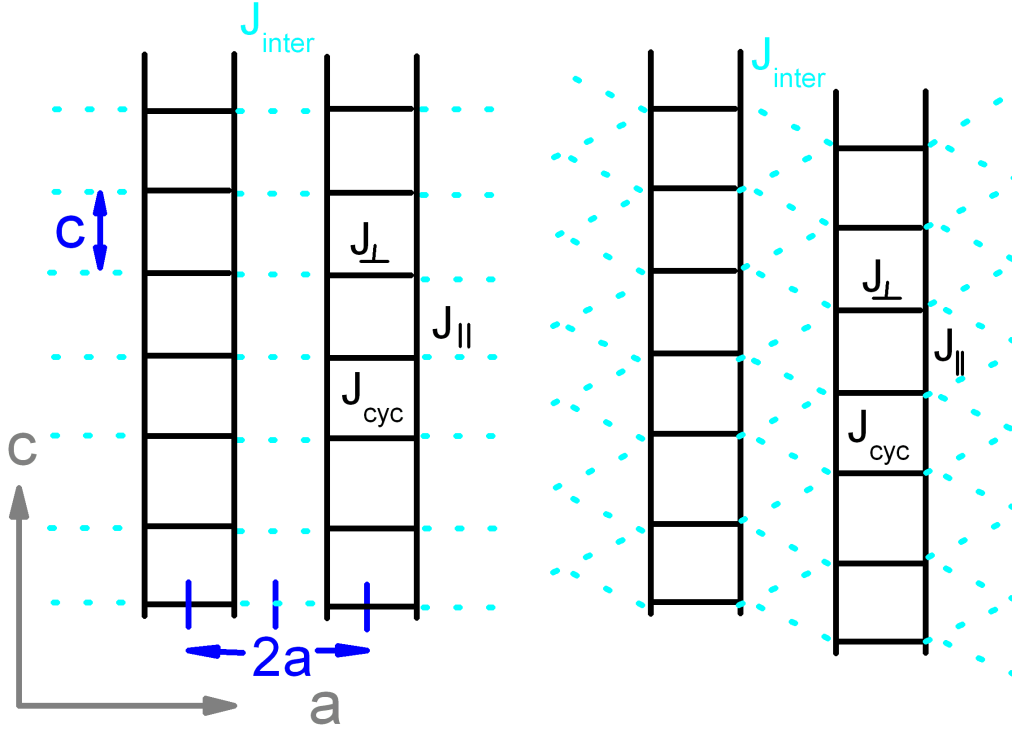$$H = H_{\mathrm{isol}} + H_{\mathrm{inter}}, \tag{6.1.1}$$

Figure 6.1.1: The coupling of isolated spin-$\frac{1}{2}$ Heisenberg ladders is sketched, where the left panel represents an in-line coupling (referred to as the square lattice coupling) and the right panel a $\frac{c}{2}$-shifted coupling (referred to as the trellis lattice coupling). The constant a reflects the lattice spacing along the rungs and c along the ladder direction. For the square lattice $a = c$ is valid.

where H_{isol} is the isolated ladder Hamiltonian and H_{inter} describes the inter-ladder Hamiltonian. The well known isolated Hamiltonian, also introduced in Chapter 5 and discussed in detail in the literature, e.g., in Refs. [29] and [28], reads

$$\frac{H_{\text{isol}}}{J_\perp} = H_\perp + \frac{J_\parallel}{J_\perp} H_\parallel + \frac{J_{\text{cyc}}}{J_\perp} H_{\text{cyc}}. \qquad (6.1.2)$$

The corresponding inter-ladder Hamiltonian H_{inter} reads in general

$$H_{\text{inter}} = J_{\text{inter}} \sum_{i \in \Gamma} \vec{S}_i^R \cdot \vec{S}_{i+\delta}^L, \qquad (6.1.3)$$

where the index i counts the rungs and δ represents the distance to the neighboring ladder. The capitals L and R stand for left and right spin, respectively, on the particular

rung. The distance δ is determined by the underlying lattice geometry. Therefore the exact form of H_{inter} is determined by the particular lattice, and will be discussed in the next sections for the square and the trellis lattice coupling.

6.1.1   Ladders with a square lattice coupling

First we will derive the effective one-triplon dispersion for the square lattice. We do not present the derivation of the one-triplon dispersion of H_{isol} here, because it is described in detail in the literature [90, 65, 29, 28]. Instead, we start with the final result

$$H_{\text{isol}} = \sum_{h,k;\alpha} \omega_0(k) t^{\dagger}_{k,0} t_{k,0} \tag{6.1.4}$$

obtained after applying the PCUT method and a Bogoliubov transformation. The one-triplon dispersion $\omega_0(k)$ is of the same form as in Eq. 5.2.2. We restrict ourselves to the inter-ladder Hamiltonian. In the case of a square lattice coupling it reads

$$H_{\text{inter}} = J_{\text{inter}} \sum_i \vec{S}^R_i \cdot \vec{S}^L_{i+2a}, \tag{6.1.5}$$

where J_{inter} represents the coupling parameter between two neighboring ladders. The distance δ between the two neighboring ladders is given by $\delta = (2a, 0)$. Inserting the effective spin operators (5.1.10) into the inter-ladder Hamiltonian gives

$$\begin{aligned}
H_{\text{inter}}(r) &= J_{\text{inter}} \sum_i \vec{S}^R_i \cdot \vec{S}^L_{i+2a} \\
&= -J_{\text{inter}} \sum_{i,m,m'} a_m a_{m'} \left(t^{\dagger}_{i+m,\alpha} s_{i+m,\alpha} + s^{\dagger}_{i+m,\alpha} t_{i+m} \right) \\
&\quad \cdot \left(t^{\dagger}_{i+m'+2a,\alpha} s_{i+m'+2a,\alpha} + s^{\dagger}_{i+m'+2a,\alpha} t_{i+m'+2a} \right) \\
&= -J_{\text{inter}} \sum_{i,m,m'} a_m a_{m'} s^2 \left(t^{\dagger}_{i+m,\alpha} t^{\dagger}_{i+m'+2a,\alpha} + t^{\dagger}_{i+m,\alpha} t_{i+m'+2a,\alpha} \right. \\
&\quad \left. + t_{i+m+2a} t^{\dagger}_{i+m'+2a} + t_{i+m,\alpha} t_{i+m'+2a,\alpha} \right),
\end{aligned} \tag{6.1.6}$$

where we introduce singlet annihilation/creation operator $s_i, s^{\dagger}_i$ where a triplet $t^{\dagger}_i, t_i$ is created/annihilated. These introduced singlet operators $s^{\dagger}_i, s_i$ are replaced by their average $\langle s^{\dagger}_i \rangle = s = \langle s_i \rangle$ in the latter step, because we consider the singlet bosons as

condensed. The minus sign results from the coupling of a right spin on rung i with the left spin on rung $i + 2a$. A Fourier transformation of the triplet operators

$$t_{i,\alpha}^\dagger = \sum_{k,h} t_{k,h,\alpha}^\dagger \exp\left(2\pi i \left(k r_{i+m} + h r_{i+m+2a}\right)\right)$$

$$t_{i,\alpha} = \sum_{k,h} t_{k,h,\alpha} \exp\left(-2\pi i \left(k r_{i+m} + h r_{i+m+2a}\right)\right)$$

(6.1.7)

results in the Fourier transformed Hamiltonian

$$\begin{aligned}
H_{\text{inter}}(k) = &-J_{\text{inter}} \sum_{k,h,\alpha} a^2(k) s^2 \Big[t_{k,h,\alpha}^\dagger t_{k,h,\alpha}^\dagger e^{2\pi i(k r_{i+m} + h r_{i+m})} e^{2\pi i(k r_{i+m} + h r_{i+m+2a})} \\
&+ t_{k,h,\alpha}^\dagger t_{k,h,\alpha} e^{2\pi i(k r_{i+m} + h r_{i+m})} e^{-2\pi i(k r_{i+m} + h r_{i+m+2a})} \\
&+ t_{k,h,\alpha} t_{k,h,\alpha}^\dagger e^{-2\pi i(k r_{i+m} + h r_{i+m})} e^{2\pi i(k r_{i+m} + h r_{i+m+2a})} \\
&+ t_{k,h,\alpha} t_{k,h,\alpha} e^{-2\pi i(k r_{i+m} + h r_{i+m})} e^{-2\pi i(k r_{i+m} + h r_{i+m+2a})} \Big] \\
= &-J_{\text{inter}} \sum_{k,h,\alpha} a^2(k) s^2 \cos(4\pi h) \left(t_{k,h,\alpha}^\dagger + t_{-k,-h,\alpha} \right) \left(t_{k,h,\alpha} + t_{-k,-h,\alpha}^\dagger \right).
\end{aligned}$$

(6.1.8)

In the last step the lattice constant a in the cosine is set to unity and the relation

$$\cos(4\pi h) = \frac{1}{2} \left(e^{(i4\pi h)} + e^{(-i4\pi h)} \right)$$

(6.1.9)

is used. Here, $a^2(k)$ is the one-triplon spectral weight and is given by the Fourier transform of the coefficients a_m according to

$$a(k) = \sum_m e^{(i2\pi km)} a_m.$$

(6.1.10)

Because of $a_m = a_{-m}$ the spectral weight $a(k)$ is real. We define

$$d_{h,k}(s) := \cos(4\pi h) a^2(k) s^2,$$

(6.1.11)

where h is measured in reciprocal lattice units (rlu). The cosine captures the shift from one ladder to the neighboring one.

The total Hamiltonian H describing the coupling of two isolated ladders with a square lattice coupling after the CUT and after neglecting multi-triplon contributions reads

$$H_{\text{isol}} + H_{\text{inter}} = \sum_{h,k;\alpha} \omega_0(k,s) t_{k,0}^\dagger t_{k,0} - J_{\text{inter}} d_{h,k}(s) \left(t_{k,h,\alpha}^\dagger + t_{-k,-h,\alpha} \right) \left(t_{k,h,\alpha} + t_{-k,-h,\alpha}^\dagger \right).$$

(6.1.12)

In order to diagonalize this Hamiltonian a standard Bogoliubov transformation is applied allowing for rewriting the Hamiltonian in new bosonic creation/annihilation operators $\gamma^\dagger_{k,h,\alpha}, \gamma_{k,h,\alpha}$ given by

$$
\begin{aligned}
t_{k,h} &= u_{k,h}\gamma_{k,h} + v_{k,h}\gamma^\dagger_{-k,-h} \\
t^\dagger_{k,h} &= u_{k,h}\gamma^\dagger_{k,h} + v_{k,h}\gamma_{-k,-h} \\
t_{-k,-h} &= u_{k,h}\gamma_{-k,-h} + v_{k,h}\gamma^\dagger_{k,h} \\
t^\dagger_{-k,-h} &= u_{k,h}\gamma^\dagger_{-k,-h} + v_{k,h}\gamma_{k,h},
\end{aligned}
\tag{6.1.13}
$$

where $u_{k,h}, v_{k,h} \in \mathbb{R}$. Inserting the new representation into the Hamiltonian (6.1.22) gives

$$
\begin{aligned}
H = \sum_{k,h,\alpha} \omega_0(k,s) &\left(u^2_{k,h}\gamma^\dagger_{k,h}\gamma_{k,h} + v^2_{k,h}\gamma_{-k,-h}\gamma^\dagger_{-k,-h} \right. \\
&\left. + {\color{red}u_{k,h}v_{k,h}\left(\gamma^\dagger_{k,h}\gamma^\dagger_{-k,-h} + \gamma_{-k,-h}\gamma_{k,h}\right)} \right) \\
- J_{\text{inter}}d_{k,h}(s) &\left[\left(u^2_{k,h} + v^2_{k,h}\right)\left(\gamma^\dagger_{k,h}\gamma_{k,h} + \gamma_{-k,-h}\gamma^\dagger_{-k,-h}\right) \right. \\
&+ 2u_{k,h}v_{k,h}\left(\gamma^\dagger_{k,h}\gamma^\dagger_{-k,-h} + \gamma_{-k,-h}\gamma_{k,h}\right) \\
&+ {\color{red}\left(u^2_{k,h} + v^2_{k,h}\right)\left(\gamma^\dagger_{k,h}\gamma^\dagger_{-k,-h} + \gamma_{-k,-h}\gamma_{k,h}\right)} \\
&\left. + 2u_{k,h}v_{k,h}\left(\gamma^\dagger_{k,h}\gamma_{k,h} + \gamma_{-k,-h}\gamma^\dagger_{-k,-h}\right) \right].
\end{aligned}
\tag{6.1.14}
$$

The red colored terms represent the off-diagonal terms. The new bosonic operators γ and $\gamma^\dagger$ fulfill the bosonic commutator relation. This is reflected by the constraint

$$
u^2_{k,h} - v^2_{k,h} = 1
\tag{6.1.15}
$$

for all k, h. To get rid of the off-diagonal terms we have to solve

$$
\left[\omega_0(k,s) - 2J_{\text{inter}}d_{h,k}(s)\right]u_{k,h}v_{k,h} - J_{\text{inter}}d_{h,k}(s)\left(u^2_{k,h} + v^2_{k,h}\right) = 0.
\tag{6.1.16}
$$

Together with Eq. 6.1.15 we obtain a system of equations to determine the coefficients $u_{k,h}, v_{k,h}$, which in turn allows for determining the effective one-triplon dispersion including the effect of inter-ladder coupling. The dispersion relation due to the diagonalized Hamiltonian for a square lattice coupling in reciprocal lattice units is finally given

by

$$\omega(k, h, s, J_{\text{inter}}) = \sqrt{(\omega_0(k, s) - 2J_{\text{inter}}d_{h,k}(s))^2 - (2J_{\text{inter}}d_{h,k}(s))^2}$$

$$= \sqrt{\omega_0^2(k, s) + 4J_{\text{inter}}^2 d_{h,k}^2(s) - 4J_{\text{inter}}^2 d_{h,k}^2(s) - 4\omega_0(k, s)J_{\text{inter}}d_{h,k}(s)}$$

$$= \sqrt{\omega_0^2(k, s) - 4J_{\text{inter}}s^2 a^2(k)\omega_0(k, s)\cos(4\pi h)}.$$

$$(6.1.17)$$

Since we deal with a non-diagonal Hamiltonian in Eq. 6.1.22 the Bogoliubov transformation has to be also applied to the hardcore constraint Eq. 5.2.3, that has to be Fourier transformed first. We obtain

$$0 = s^2 - 1 + \sum_{\alpha,k,h} \langle t_{k,h,\alpha}^\dagger t_{k,h,\alpha} \rangle$$

$$= s^2 - 1 + 3 \sum_{k,h} \left\langle \left(u_{k,h}\gamma_{k,h}^\dagger + v_{k,h}\gamma_{-k,-h} \right) \left(u_{k,h}\gamma_{k,h} + v_{k,h}\gamma_{-k,-h}^\dagger \right) \right\rangle$$

$$= s^2 - 1 + 3 \sum_{k,h} \left\langle u_{k,h}^2\gamma_{k,h}^\dagger\gamma_{k,h} + v_{k,h}^2\gamma_{-k,-h}^\dagger\gamma_{-k,-h} + v_{k,h}^2 \right\rangle$$

$$+ 3 \sum_{k,h} \left(\underbrace{\left\langle u_{k,h}v_{k,h}\gamma_{k,h}^\dagger\gamma_{-k,-h}^\dagger \right\rangle}_{=0} + \underbrace{\left\langle u_{k,h}v_{k,h}\gamma_{-k,-h}\gamma_{k,h} \right\rangle}_{=0} \right)$$

$$= s^2 - 1 + 3 \sum_{k,h} \left(\langle \gamma_{k,h}^\dagger\gamma_{k,h} \rangle + 2v_{k,h}^2\langle \gamma_{k,h}^\dagger\gamma_{k,h} \rangle + \langle v_{k,h}^2 \rangle \right)$$

$$(6.1.18)$$

$$= s^2 - 1 + \frac{3}{4\pi^2} \iint_{1^{\text{st}}\text{BZ}} \frac{e^{-\frac{\omega(k,h,s)}{E}}}{Z} \text{d}k\text{d}h$$

$$+ \frac{3}{4\pi^2} \iint_{1^{\text{st}}\text{BZ}} \left(\frac{\omega_0(k,s) - 2J_{inter}d_{k,h}(s)}{\omega(k,h,s)} - 1 \right) \frac{e^{-\frac{\omega(k,h,s)}{E}}}{Z} \text{d}k\text{d}h$$

$$+ \frac{3}{4\pi^2} \iint_{1^{\text{st}}\text{BZ}} \left(\frac{-\omega(k,h,s) + (\omega_0(k,s) - 2J_{inter}d_{k,h}(s))}{2\omega(k,h,s)} \right) \text{d}k\text{d}h$$

$$= s^2 - 1 + \frac{3}{4\pi^2} \iint_{1^{\text{st}}\text{BZ}} \left(\frac{\omega_0(k,s) - 2J_{inter}d_{k,h}(s)}{\omega(k,h,s)} \right) \frac{e^{-\frac{\omega(k,h,s)}{E}}}{Z} \text{d}k\text{d}h$$

$$+ \frac{3}{4\pi^2} \iint_{1^{\text{st}}\text{BZ}} \left(\frac{\omega_0(k,s) - 2J_{inter}d_{k,h}(s)}{\omega(k,h,s)} - \frac{1}{2} \right) \text{d}k\text{d}h \ .$$

By the use of the dispersion 6.1.17 we solve Eq. 6.1.18 self-consistently for the mean field parameter s at a given J_{inter} and $E = k_B T$. While for zero inter-ladder coupling $J_{\text{inter}} = 0$ Eq. 6.1.18 results in Eq. 5.2.14, for zero temperature Eq. 6.1.18 represents

the quantum fluctuations, that will be focused on below. Above, Z denotes the partition function as defined in Chapter 5, where the dispersion is replaced by the dispersion given in Eq. 6.1.17. The resulting $s(J_{\text{inter}}, T)$ then introduces the effect of the inter-ladder coupling for the square lattice case when it is inserted into physical quantities such as the dispersion $\omega(k, h, s, J_{\text{inter}})$, the effective one-triplon spectral weight $a^2(k)$, and hence the dynamical structure factor $S(k, h, \omega)$.

The numerical results for $x = \frac{J_{\parallel}}{J_{\perp}} = \{1; 1.5\}$ with $x_{\text{cyc}} = \{0; 0.2\}$ respectively and $x_{\text{inter}} = \frac{J_{\text{inter}}}{J_{\perp}}$ will be presented in Section 6.2. First, the effective one-triplon dispersion for a trellis lattice coupling will be derived.

6.1.2   The trellis lattice model

The trellis lattice is sketched in Fig. 6.1.2. The coupling between the ladders is strongly frustrated [4] due to the shifted positions of the single ladders by $\frac{c}{2}$ to each another. The same procedure as before is now applied to the inter-ladder Hamiltonian for a trellis lattice coupling. In the case of the $\frac{c}{2}$-shifted coupling the inter-ladder Hamiltonian changes
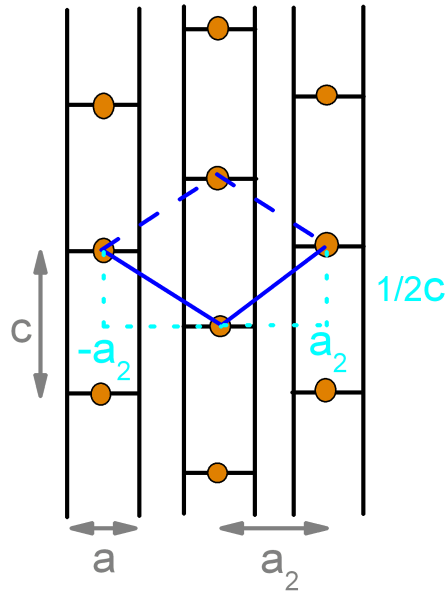

Figure 6.1.2: Schematic view of the inter-ladder coupling in a trellis lattice. The orange circles denote the coupling of two spins on the same rung centered in the middle of the rung. The lattice spacing between two spins on one rung is denoted by a, and between the centers of two rungs on neighboring ladders by a_2. Along the ladder the spacing is given by c.

to

$$H_{\text{inter}}(r) = J_{\text{inter}} \sum_i \left(\vec{S}_i^R \cdot \vec{S}_{i+a_2+\frac{1}{2}c}^L + \vec{S}_i^R \cdot \vec{S}_{i-a_2+\frac{1}{2}c}^L \right)$$

$$= -J_{\text{inter}} \sum_{i,m,m'} a_m a_{m'} \left(t_{i+m,\alpha}^\dagger + t_{i+m} \right) \cdot \left(t_{i+m'+a_2+\frac{c}{2},\alpha}^\dagger + t_{i+m'+a_2+\frac{c}{2},\alpha} \right)$$

$$+ \left(t_{i+m,\alpha}^\dagger + t_{i+m,\alpha} \right) \cdot \left(t_{i+m'-a_2+\frac{c}{2},\alpha}^\dagger + t_{i+m'-a_2+\frac{c}{2},\alpha} \right)$$

$$= -J_{\text{inter}} \sum_{i,m,m'} a_m a_{m'} s^2 \left(t_{i+m,\alpha}^\dagger t_{i+m'+a_2+\frac{c}{2},\alpha}^\dagger + t_{i+m,\alpha}^\dagger t_{i+m'+a_2+\frac{c}{2},\alpha} \right.$$

$$+ t_{i+m} t_{i+m'+a_2+\frac{c}{2}}^\dagger + t_{i+m,\alpha} t_{i+m'+a_2+\frac{c}{2},\alpha} + t_{i+m,\alpha}^\dagger t_{i+m'-a_2+\frac{c}{2},\alpha}^\dagger$$

$$\left. + t_{i+m,\alpha}^\dagger t_{i+m'-a_2+\frac{c}{2},\alpha} + t_{i+m} t_{i+m'-a_2+\frac{c}{2}}^\dagger + t_{i+m,\alpha} t_{i+m'-a_2+\frac{c}{2},\alpha} \right) \tag{6.1.19}$$

where the singlet operators $s^\dagger, s$ are directly replaced by their average for convenience. Here, the index $i + m' \pm a_2 + \frac{c}{2}$ means, that on rung $i + m'$ an excitation is created/annihilated interacting with the spin being $\left(\pm a_2, \frac{c}{2}\right)$ away. The global minus sign arises again from the coupling of a right spin with a left spin. Fourier transformation of the triplet operators Eq. 6.1.7 gives

$$H_{\text{inter}}(k) = -J_{\text{inter}} \sum_{k,h,\alpha} a^2(k) s^2 \left(t_{k,h,\alpha}^\dagger t_{k,h,\alpha}^\dagger e^{2\pi i (kr_{i+m}+hr_{i+m})} e^{2\pi i \left(kr_{i+m}+\frac{c}{2}+hr_{i+m+a_2}\right)} \right.$$

$$+ t_{k,h,\alpha}^\dagger t_{k,h,\alpha} e^{2\pi i (kr_{i+m}+hr_{i+m})} e^{-2\pi i \left(kr_{i+m}+\frac{c}{2}+hr_{i+m+a_2}\right)}$$

$$+ t_{k,h,\alpha} t_{k,h,\alpha}^\dagger e^{-2\pi i (kr_{i+m}+hr_{i+m})} e^{2\pi i \left(kr_{i+m}+\frac{c}{2}+hr_{i+m+a_2}\right)}$$

$$+ t_{k,h,\alpha} t_{k,h,\alpha} e^{-2\pi i (kr_{i+m}+hr_{i+m})} e^{-2\pi i \left(kr_{i+m}+\frac{c}{2}+hr_{i+m+a_2}\right)}$$

$$+ t_{k,h,\alpha}^\dagger t_{k,h,\alpha}^\dagger e^{2\pi i (kr_{i+m}+hr_{i+m})} e^{2\pi i \left(kr_{i+m}+\frac{c}{2}+hr_{i+m-a_2}\right)}$$

$$+ t_{k,h,\alpha}^\dagger t_{k,h,\alpha} e^{2\pi i (kr_{i+m}+hr_{i+m})} e^{-2\pi i \left(kr_{i+m}+\frac{c}{2}+hr_{i+m-a_2}\right)}$$

$$+ t_{k,h,\alpha} t_{k,h,\alpha}^\dagger e^{-2\pi i (kr_{i+m}+hr_{i+m})} e^{2\pi i \left(kr_{i+m}+\frac{c}{2}+hr_{i+m-a_2}\right)}$$

$$\left. + t_{k,h,\alpha} t_{k,h,\alpha} e^{-2\pi i (kr_{i+m}+hr_{i+m})} e^{-2\pi i \left(kr_{i+m}+\frac{c}{2}+hr_{i+m-a_2}\right)} \right)$$

$$= -J_{\text{inter}} \sum_{k,h,\alpha} 2 a^2(k) s^2 \cos(\pi k) \cos(\pi h) \left(t_{k,h,\alpha}^\dagger + t_{-k,-h,\alpha} \right)$$

$$\cdot \left(t_{k,h,\alpha} + t_{-k,-h,\alpha}^\dagger \right) . \tag{6.1.20}$$

In the latter step the lattice constants $2a_2$ and c are set to unity. We define

$$d_{h,k}(s) := \cos(\pi k)\cos(\pi h)a^2(k)s^2, \tag{6.1.21}$$

so that the total Hamiltonian H for a trellis lattice coupling after the CUT and after neglecting multi-triplon contributions reads

$$H_{\text{isol}}+H_{\text{inter}} = \sum_{h,k;\alpha} \omega_0(k,s)t^\dagger_{k,0}t_{k,0} - J_{\text{inter}}2d_{h,k}(s)\left(t^\dagger_{k,h,\alpha} + t_{-k,-h,\alpha}\right)\left(t_{k,h,\alpha} + t^\dagger_{-k,-h,\alpha}\right). \tag{6.1.22}$$

This Hamiltonian is diagonalized by a standard Bogoliubov transformation (see Eq. 6.1.13) yielding an analogue to Eq. 6.1.14. To get rid of the off-diagonal terms

$$\left[\omega_0(k,s) - 4J_{\text{inter}}d_{h,k}(s)\right]u_{k,h}v_{k,h} - 2J_{\text{inter}}d_{h,k}(s)\left(u^2_{k,h} + v^2_{k,h}\right) = 0 \tag{6.1.23}$$

has to be solved under the constraint defined by Eq. 6.1.15. The dispersion relation according to the diagonalized Hamiltonian for a trellis lattice coupling in reciprocal lattice units is finally given by

$$\omega(k,h,s) = \sqrt{\omega_0^2(k,s) - 8J_{\text{inter}}s^2a^2(k)\omega_0(k,s)\cos(\pi h)\cos(\pi k)}. \tag{6.1.24}$$

Since we represent the momenta h, k by their components along the ladder c and perpendicular to the ladder a_2, they are measured in units of $\frac{2\pi}{c}$ and $\frac{2\pi}{2a_2}$ respectively. Hence, the dispersion shows a periodicity of 2 both with respect to k and h. However, shifting $k \to k+1$ and $h \to h+1$ together reproduces the spectrum as it has to be [4]. The skewed unit cell as shown in Fig. 6.1.2 is simpler in spite of the *unusual* periodicities because it contains only one dimer so that it is a Bravais lattice with one (threefold degenerated) triplon mode per unit cell [4]. If one insisted on using unit vectors along and perpendicular to the ladders the unit cell would comprise two dimers so that two modes per unit cell have to be considered. They correspond to the modes at h and $h+1$ [4]. Again the Bogoliubov transformation has to be applied to the hardcore constraint in order to obtain the analogue to Eq. 6.1.18 – now with the effective one-triplon dispersion in the case of a trellis lattice coupling employed – which is solved self-consistently at zero and finite temperature for the mean field parameter s assuring the hardcore-constraint at a given J_{inter} and $E = k_B T$.

6.2 Theoretical results

Next some considerations concerning the temperature dependent term of Eq. 6.1.18 in general will be presented. After that the theoretical results at zero and finite temperature for both kinds of coupling will be discussed and compared to the zero temperature results in Ref. [2] and Ref. [4].

6.2.1 Remarks on the zero temperature limit in two dimensions

The preceding considerations are next applied to the one-triplon dispersion including the trellis lattice coupling. This is the lattice structure relevant for the cuprate $La_4Sr_{10}Cu_{24}O_{41}$, which serves for experimental validity in this work. However, the following argument can immediately be transferred to the square lattice. We argue, that the temperature dependent term of Eq. 6.1.18 yields zero for all inter-ladder coupling x_{inter} if $T \to 0$. This simplifies Eq. 6.1.18 for zero temperature.

The one-triplon dispersion ω_0 as employed in Eq. 6.1.24 is real, positive and bounded away from zero, as has been discussed in Chapter 5. This means that there is a constant $m > 0$ such that

$$\omega_0(k, s) \geq m > 0 \tag{6.2.1}$$

for all k holds. The above relation states nothing else than the existence of an energy gap. According to Eq. 6.1.24 the effective one-triplon dispersion $\omega(k, h, s)$ for a trellis lattice coupling can be represented by

$$\omega(k, h, s) = \omega_0(k, s)\sqrt{1 - \frac{8J_{\text{inter}}a^2(k)s^2}{\omega_0(k, s)} \cos(\pi h) \cos(\pi k)}. \tag{6.2.2}$$

If we now assume that J_{inter} is chosen in such a way that

$$\xi := \max_{k,h} \left\{ \left| \frac{8J_{\text{inter}}a^2(k)s^2}{\omega_0(k, s)} \cos(\pi h) \cos(\pi k) \right| \right\} < 1 \tag{6.2.3}$$

holds, then $\omega(k, h, s)$ is also bounded away from zero, i.e., it possesses an energy gap. This is the case for a weak coupling between neighboring ladders. Inserting Ineq. 6.2.1 and Eq. 6.2.3 into Eq. 6.2.2 leads to the quantitative statement

$$\omega(k, h, s) \geq m\sqrt{1 - \xi} > 0 \tag{6.2.4}$$

for all k, h. Since $f(x) = e^{-x}$ is a decreasing function, Ineq. 6.2.4 implies

$$e^{-\frac{\omega(k,h,s)}{E}} \le e^{-\frac{m\sqrt{1-\xi}}{E}} \tag{6.2.5}$$

for all k, h. A direct calculation yields

$$\lim_{E \to 0} \int_{-\pi}^{\pi} \int_{-\pi}^{\pi} e^{-\frac{\omega(k,h,s)}{E}} \mathrm{d}k\mathrm{d}h = \int_{-\pi}^{\pi} \int_{-\pi}^{\pi} \lim_{E \to 0} e^{-\frac{\omega(k,h,s)}{E}} \mathrm{d}k\mathrm{d}h = 0. \tag{6.2.6}$$

Next, we study the case of critical inter-ladder coupling. This means, we choose the minimal coupling $|J_\mathrm{inter}|$, such that $\omega(k, h, s) = 0$ possesses a zero and the energy gap is closed. From the particular shape of $\omega_0(k, s)$ and $a^2(k)$ employed in this work, we deduce that the critical $\omega(k, h, s)$ assumes the value 0 at a finite number of points (k_i, h_i). In all other points it is still positive. Hence, we obtain for the integrand

$$e^{-\frac{\omega(k,h,s)}{E}} \to 0 \qquad (E \to 0) \tag{6.2.7}$$

in all points (k, h) except of the zeroes (k_i, h_i), where $e^{-\frac{\omega(k,h,s)}{E}}$ equals 1 for all values of $E > 0$ and, hence, also in the limit. This means, that $e^{-\frac{\omega(k,h,s)}{E}}$ tends pointwise to 0 for $E \to 0$ on the square $[-\pi, \pi]^2$ except of a set of Lebesgue measure zero (see, e.g., Ref. [102]). As $|e^{-\frac{\omega(k,h,s)}{E}}| \le 1$ is true on $[-\pi, \pi]^2$, the integrand is dominated by an integrable function. Consequently, the dominated convergence theorem from Lebesgue integration theory [102] applies, yielding again the relation presented in Eq. 6.2.6. Hence, Eq. 6.1.18 is finally reduced to

$$0 \overset{!}{=} s^2 - \frac{5}{2} + \frac{3}{4\pi^2} \iint_{1^\mathrm{st}\mathrm{BZ}} \left(\frac{\omega_0(k,s) - 2J_{inter}d_{k,h}(s)}{2\omega(k,h,s)} \right) \mathrm{d}k\mathrm{d}h \tag{6.2.8}$$

for $T = 0$ and all values of physical meaningful values of J_inter, i.e., for all values of the inter-ladder coupling that only yield real values for $\omega(k, h, s)$ (see below). The last Eq. 6.2.8 gives information on the influence of quantum fluctuation.

From a purely numerical interest, we now analyze the case that

$$\left| \frac{8J_\mathrm{inter}a^2(k)s^2}{\omega_0(k,s)} \cos(\pi h) \cos(\pi k) \right| > 1. \tag{6.2.9}$$

for some values of k and h. In this case the dispersion $\omega(k, h, s)$ assumes complex values. Note that a complex dispersion has no physical relevance and is therefore only

of mathematical interest. However, the following argument will give an easy numerical criterion, whether the solution of Eq. 6.1.18 leads to complex values of $\omega(k, h, s)$ as a consequence of a strong inter-ladder coupling. For simplicity, we consider the case

$$\left| \frac{8 J_{\text{inter}} a^2(k) s^2}{\omega_0(k, s)} \cos(\pi h) \cos(\pi k) \right| > 1 \qquad (6.2.10)$$

for all values of h and k before we turn to the general case. Then

$$\omega(k, h, s) = \mathrm{i} \omega_0(k, s) \sqrt{\left| 1 - \frac{8 J_{\text{inter}} a^2(k) s^2}{\omega_0(k, s)} \cos(\pi h) \cos(\pi k) \right|} \qquad (6.2.11)$$

is purely imaginary. This affects the integral in equation (6.1.18), resulting in

$$\int_{-\pi}^{\pi} \int_{-\pi}^{\pi} \mathrm{e}^{-\mathrm{i} \frac{|\omega(k, h, s)|}{E}} \, \mathrm{d}k \mathrm{d}h \qquad (6.2.12)$$

for the integral in the defining equation for s. Since $\mu = \frac{1}{E}$ tends to infinity for $E \to 0$ the *Riemann-Lebesgue Lemma* applies yielding

$$\lim_{\mu \to \infty} \int_{-\pi}^{\pi} \int_{-\pi}^{\pi} \mathrm{e}^{-\mathrm{i} \mu |\omega(k, h, s)|} \, \mathrm{d}k \mathrm{d}h = 0 \qquad (6.2.13)$$

for all sufficiently large values of J_{inter}.

Turning now to the general case, we assume that $\omega(k, h, s)$ assumes both real and imaginary values including zero. However, we have to restrict the set on which $\omega(k, h, s)$ is zero to be a subset of $[-\pi, \pi]^2$ of Lebesgue measure zero. Then the integrand of the integrals can be split according to the cases that $\omega(k, h, s)$ is real (including zero) or imaginary. The two preceding different arguments for the purely imaginary and for the purely real case (including zeros) can be applied to the resulting individual terms. Consequently, the integral in Eq. 6.2.6 is zero for all values of the inter-ladder coupling J_{inter}, and hence Eq. 6.2.8 is valid for $T = 0$ even if its solution s is imaginary. This is of particular importance for numerical issues, since it makes clear that an imaginary solution of the simplified equation 6.2.8 is also an imaginary solution of the full equation 6.1.18 and thus indicates that a too large coupling constant J_{inter} has been employed without the need of solving the more complicated Eq. 6.1.18.

6.2.2 Square lattice inter-ladder coupling at zero temperature

The main purpose of the mean field treatment is to investigate the influence of quantum fluctuations on the closure of the spin gap. Thus, Eq. 6.2.8 is now solved self-consistently for the coupling of ladders in the square lattice geometry. We only present

results for $x = 1$ and $x = 1.5$ because of growing evidence, that these are the relevant parameters for cuprate ladders [96, 1, 101, 103]. More precise, $x = 1$ allows for comparison with [3], while evidence is found that $x = 1.5$ is realized in $La_4Sr_{10}Cu_{24}O_{41}$ [1].

The spin gap in the case of the square lattice coupling is presented in Fig. 6.2.1 as a function of inter-ladder coupling x_{inter}. The black curves in the panels of Fig. 6.2.1 present the spin gap with a constant singlet occupation number of $s^2 = 1$ and the cyan curves with the self-consistently solved mean singlet occupation number $s_{MF}^2 = s^2(x_{inter}, T = 0)$ according to Eq. 6.2.8. Each panel of Fig. 6.2.1 presents results for a different pair of (x, x_{cyc}) (for details see the panels).

As the black curves show the spin gap with a constant singlet occupation number of $s^2 = 1$ - i.e., to no mean field treatment - these curves show the closure of the spin gap neglecting zero temperature quantum fluctuations. Here the critical inter-ladder coupling x_{inter}^{crit}, at which the spin gap closes, is strongest for the isotropic case without cyclic exchange, hence for $x = 1$ and $x_{cyc} = 0$. With an increasing x the critical inter-ladder coupling decreases. Including a non zero cyclic exchange results in a further reduction of the value of the critical inter-ladder coupling x_{inter}^{crit}.

Including at zero temperature the quantum fluctuations (cyan colored curves in Fig. 6.2.1) results in a slightly increased critical value of the critical inter-ladder coupling x_{inter}^{crit} for each pair of (x, x_{cyc}). These critical values are summarized in Table 6.1.

(x, x_{cyc})	$x_{inter}^{crit}(s = 1)$	$x_{inter}^{crit}(s_{MF})$	Δx_{inter}^{crit}
$(1, 0)$	0.196	0.204	0.008
$(1, 0.2)$	0.0725	0.0748	0.0023
$(1.5, 0)$	0.141	0.145	0.004
$(1.5, 0.2)$	0.0648	0.0676	0.0028

Table 6.1: Values of the critical inter-ladder coupling x_{inter}^{crit}, at which the spin gap closes in the case of a square lattice coupling.

The change in the value of the critical inter-ladder coupling x_{inter}^{crit} is of the order of $3-4\%$ only. This traces back to the self consistently solved mean field singlet occupation number $s_{MF} = s(x_{inter}, T = 0)$. This quantity is presented as a function of the inter-ladder coupling x_{inter} in Fig. 6.2.2 for all pairs (x, x_{cyc}) shown in Fig. 6.2.1.

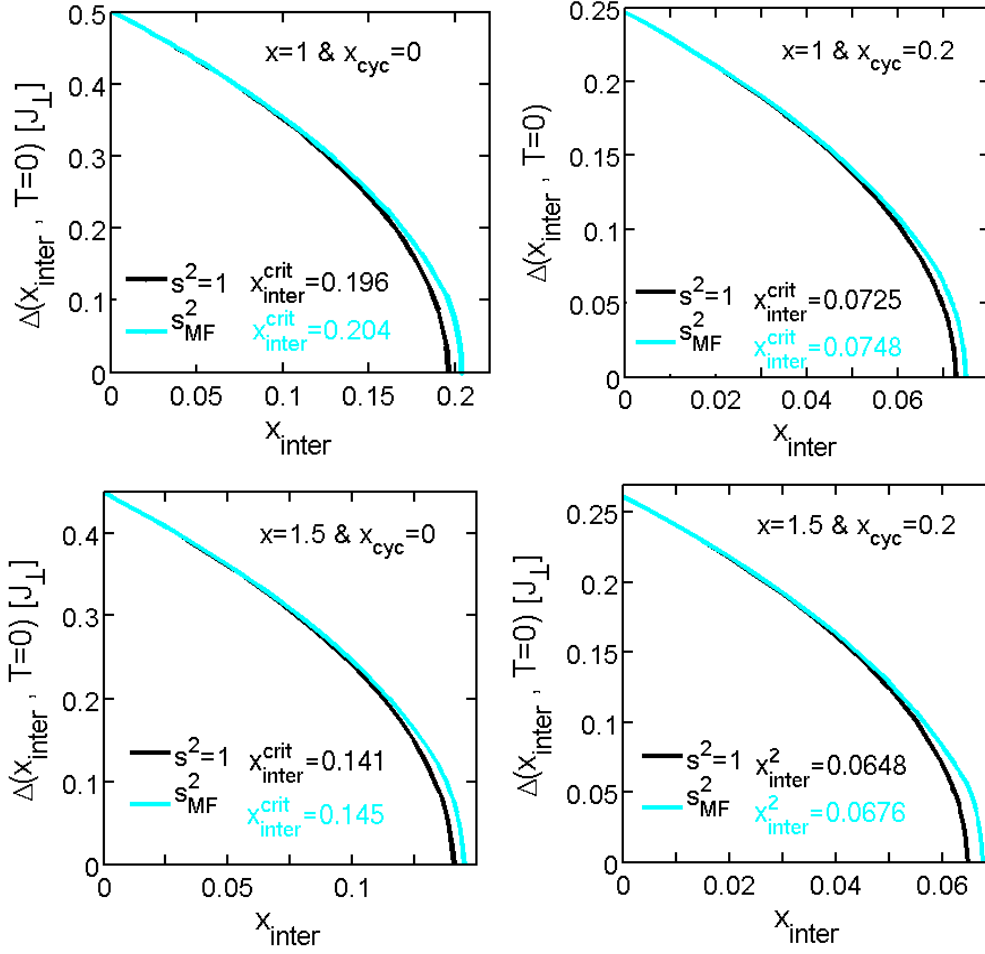During the calculation the self-consistent solution $s(x_{inter}, T)$ becomes complex. Com-

Figure 6.2.1: Spin gap at zero temperature as a function of the inter-ladder coupling x_{inter} for a constant singlet occupation number of $s^2 = 1$ (black solid curve) and for the self-consistently solved singlet occupation number s_{MF} (cyan solid curve) according to Eq. 6.2.8. The values of x_{inter} presented in the panels give the inter-ladder coupling at which the spin gap closes.

plex solutions of $s(x_{\text{inter}}, T)$ are, however, physical not meaningful. They arise when the dispersion becomes complex because of a too large inter-ladder coupling. Hence, the parameter range for x_{cyc} and x_{inter} leading to real solutions $s(x_{\text{inter}}, T)$ is of particular significance. More precisely for each x and each x_{cyc} a different *validity range* for x_{inter} is given. Thus, in Fig. 6.2.2 the self-consistently solved mean field singlet occupation number is only plotted for these validity ranges. The largest range of real solutions is yielded for $x_{\text{cyc}} = 0$ and both $x = 1$ and $x = 1.5$, where the range for the isotropic case with $x = 1$ is a little larger as compared to that for $x = 1.5$. From Fig. 6.2.2 we realize
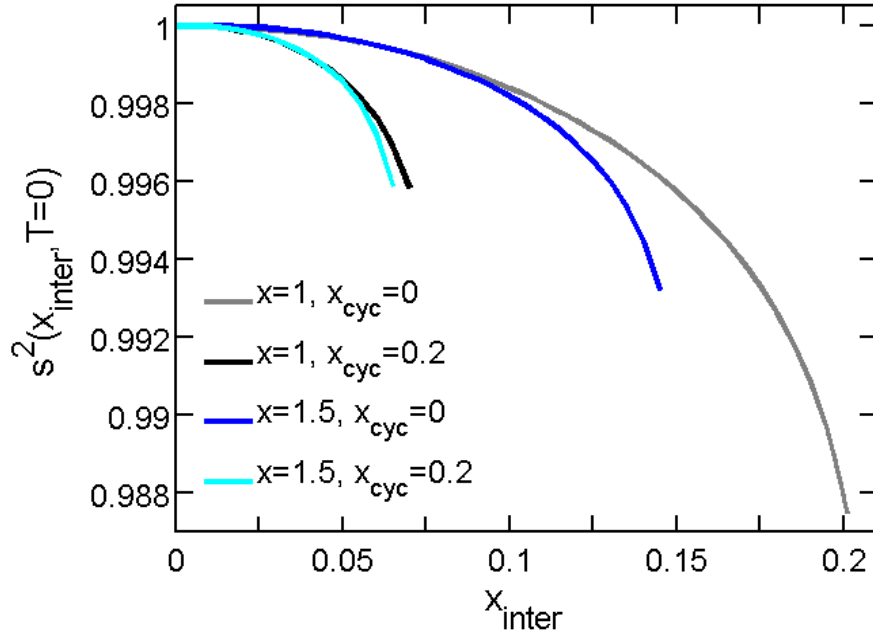
Figure 6.2.2: Singlet occupation number for the square lattice at zero temperature for $x = \{1, 1.5\}$ and $x_{\text{cyc}} = \{0, 0.2\}$ as a function of the inter-ladder coupling x_{inter}.

that a real mean field singlet occupation number can maximally deviate from 1 down to $s_{\text{MF}}^2 = 0.988$, i.e., by 1.2% for $x = 1$ and $x_{\text{cyc}} = 0$. This fact explains the small change in the critical inter-ladder coupling $x_{\text{inter}}^{\text{crit}}$.

Gopalan et al. [38] studied the coupling of two ladders in the case of the square lattice geometry as well as for a periodic array of such ladders. For the latter case they suggested a closing of the spin gap for an inter-ladder coupling of $x_{\text{inter}} = 0.25$ in the isotropic case and argued that the decrease in the spin gap with increasing x_{inter} occurs due to delocalization of the singlets across the ladders. For the mean field treatment presented here we find a closing of the spin gap for an inter-ladder coupling of $x_{\text{inter}} = 0.204$ in the isotropic case. This value of $x_{\text{inter}} = 0.204$ lies below all values that can be found in the literature, such as the QMC computation by Matsuda [37], that gave $x_{\text{inter}} = 0.314$. In conclusion, including the effect of quantum fluctuation on the mean field level leads to results that do not agree with the findings about the closure of the spin gap in the literature.

As the influence of the quantum fluctuation on the closure of the spin gap reveals to be only a small effect of about $3 - 4\%$, we relinquish to present the dispersion as a function of the wave vector, since no new physical insights will be obtained. We turn to the case of a trellis lattice coupling instead.

6.2.3 Trellis lattice inter-ladder coupling at zero temperature

In the following we investigate the influence of quantum fluctuations in the case of an underlying trellis-lattice geometry. For this purpose we evaluate Eq. 6.2.8 analogously to the previous section replacing the dispersion in Eq. 6.2.8 by the dispersion including the trellis lattice coupling as presented in Eq. 6.1.24. As in the previous section we restrict ourselves to the numerical results for $x = \{1, 1.5\}$ and $x_{\text{cyc}} = \{0, 0.2\}$.

The spin gap as a function of the inter-ladder coupling x_{inter} for various pairs of (x, x_{cyc}) is presented in Fig. 6.2.3. The black solid lines present the spin gap evaluated with a constant mean field singlet occupation number of $s^2 = 1$. With increasing x the critical inter-ladder coupling $x_{\text{inter}}^{\text{crit}}(s = 1)$ increases. Including a non zero cyclic exchange diminishes the critical inter-ladder coupling $x_{\text{inter}}^{\text{crit}}(s = 1)$.

The cyan solid curves show the results obtained with the self-consistently solved mean field singlet occupation number s_{MF}^2 by the use of Eq. 6.2.8. On the mean field level the spin gap closes at an enlarged value of the inter-ladder coupling x_{inter}. The critical inter-ladder couplings $x_{\text{inter}}^{\text{crit}}$ are summarized in Table 6.2 for $s^2 = 1$ and s_{MF}^2 including the relative change $\Delta x_{\text{inter}}^{\text{crit}}$.

(x, x_{cyc})	$x_{\text{inter}}^{\text{crit}}(s = 1)$	$x_{\text{inter}}^{\text{crit}}(s_{\text{MF}})$	$\Delta x_{\text{inter}}^{\text{crit}}$
$(1, 0)$	1.21	1.42	0.21
$(1, 0.2)$	0.8	0.97	0.17
$(1.5, 0)$	1.32	–	–
$(1.5, 0.2)$	0.9	0.97	0.07

Table 6.2: Values of the critical inter-ladder coupling $x_{\text{inter}}^{\text{crit}}$, at which the spin gap closes in the case of a trellis lattice coupling. Due to numerical problems the closing of the spin gap cannot presented for $x = 1.5$ and $x_{\text{cyc}} = 0$.

The spin gap does not close for $x = 1.5$ and $x_{\text{cyc}} = 0$ due to numerical problems. The root finding algorithm to solve Eq. 6.2.8 turned out to depend highly sensitively on the
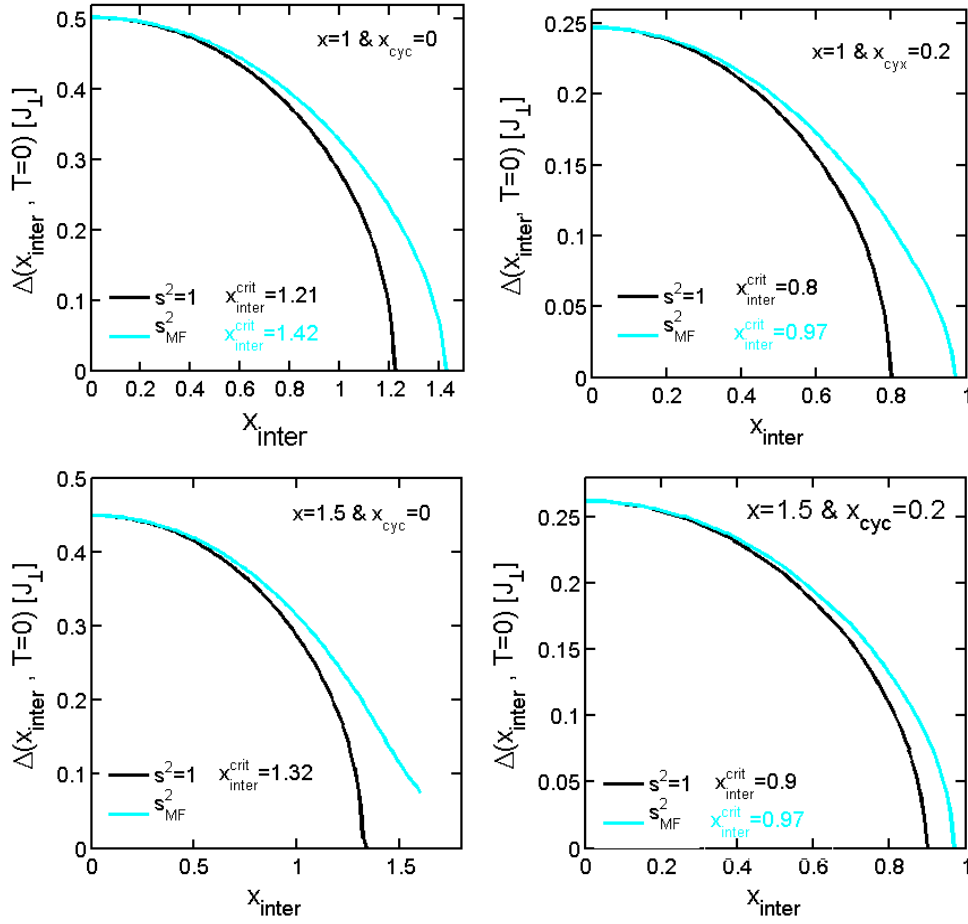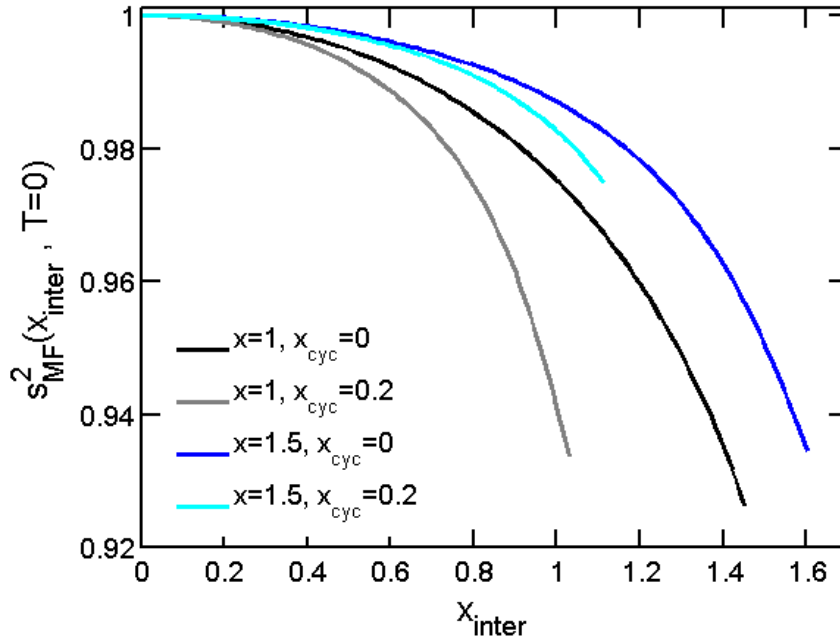
Figure 6.2.3: Spin gap with a trellis lattice coupling at zero temperature for $x = \{1, 1.5\}$ and $x_{\mathrm{cyc}} = \{0, 0.2\}$ as a function of the inter-ladder coupling x_{inter}. Solid black curves present the spin gap evaluated with a constant mean field singlet occupation number of $s^2 = 1$. The cyan solid curves present the spin gap evaluated with the self-consistently solved mean field singlet occupation number s^2_{MF}.

initial value for certain parameters. This is particulary the case for $x = 1.5$ and $x_{\mathrm{cyc}} = 0$, where the algorithm terminated at a complex solution of Eq. 6.2.8 for the chosen initial values. However, it is believed that there is a real solution despite the numerical findings.

Again the range of validity of the inter-ladder coupling x_{inter} for each pair of (x, x_{cyc}) is terminated by the set of real solutions of the self-consistently solved mean filed singlet occupation number s_{MF}. This quantity is presented in Fig. 6.2.4 as a function of the

inter-ladder coupling x_{inter} for various pairs of (x, x_{cyc}). In the case of the trellis lattice

Figure 6.2.4: Singlet occupation number for the trellis lattice coupling at zero temperature for $x = \{1, 1.5\}$ and $x_{\text{cyc}} = \{0, 0.2\}$ as a function of the inter-ladder coupling x_{inter}.

the mean field singlet occupation number deviates maximally from one by 8% down to $s_{\text{MF}}^2 = 0.925$ for $x = 1$ and $x_{\text{cyc}} = 0$. In contrast to the square lattice, the quantum fluctuations influence the closure of the spin gap in a much stronger way.

The findings in the case of a trellis lattice coupling agree with the findings of Schmidt and Uhrig in Ref. [4]. Here the gap is decreasing as a function of inter-ladder coupling x_{inter}. Gopalan et al [38] applied also a mean field treatment to the trellis lattice and found, that the excitation spectrum of such a frustrated double ladder consists of two degenerate branches at the minimum position of the spectrum [38]. Gopalan et al [38] argued that the spin gap should not change much from the spin gap of the isolated ladder, because due to the frustrated ladder coupling the singlets on two successive rungs of each ladder are completely out of phase [38]. Hence, they are not able to delocalize across the ladder through the trellis lattice coupling [38].

This is in contrast to the findings of this work. In our case, where quantum fluctuations

are included on the mean field level, we find that the spin gap closes. This allows for the argumentation that such fluctuations are not necessarily confined to the ladder.

6.2.4   Trellis and square lattice results at finite temperature

In the following we focus on the influence of the inter-ladder coupling if temperature is switched on. The effect can best be seen in the mean field singlet occupation number,
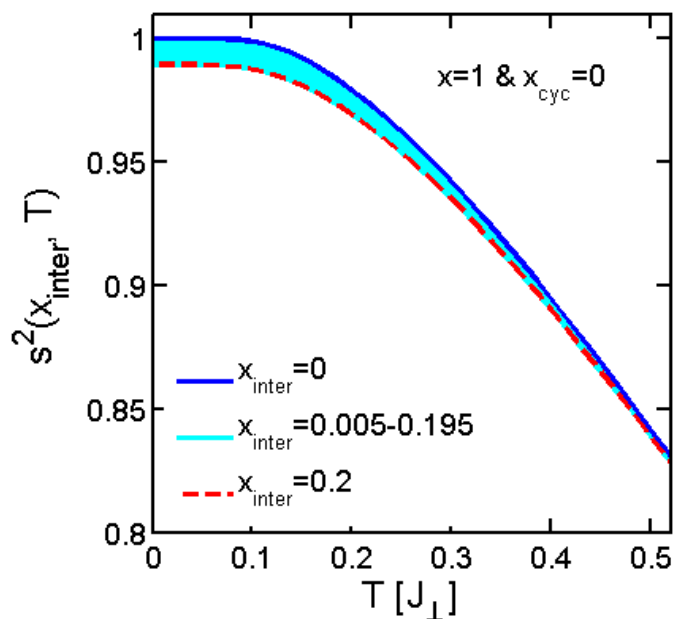

Figure 6.2.5: Square lattice coupling of ladders: Singlet occupation number for $x = 1$ and $x_{cyc} = 0$ as a function of temperature in units of the rung coupling $J_\perp$. The dark blue solid line presents the result of the isolated ladder $x_{inter} = 0$ and the red dashed line for $x_{inter} = 0.2$. The cyan colored area represents the result for $0 < x_{inter} < 0.2$.

which is shown as a function of temperature T in the Figs. 6.2.5 and 6.2.6. The result for the square lattice coupling is shown in Fig. 6.2.5 for $x = 1$ and $x_{cyc} = 0$ and for the trellis lattice coupling in Fig. 6.2.6 for $x = 1.5$ and $x_{cyc} = 0.2$. The dark blue solid line in both figures presents the result of the isolated ladder ($x_{inter} = 0$) with the corresponding pairs (x, x_{cyc}) mentioned before. The red dashed lines show the result for an inter-ladder coupling of $x_{inter} = 0.2$ for the square lattice coupling and of $x_{inter} = 0.4$ for the trellis lattice coupling. Curves for $s^2(x_{inter}, T)$ as a function of T obtained for values of the inter-ladder coupling x_{inter} between $0 < x_{inter} < 0.2$ in the square-lattice

case and between $0 < x_{\mathrm{inter}} < 0.4$ in the trellis lattice case proceed in the cyan colored area of Figs. 6.2.5 and 6.2.6, respectively.
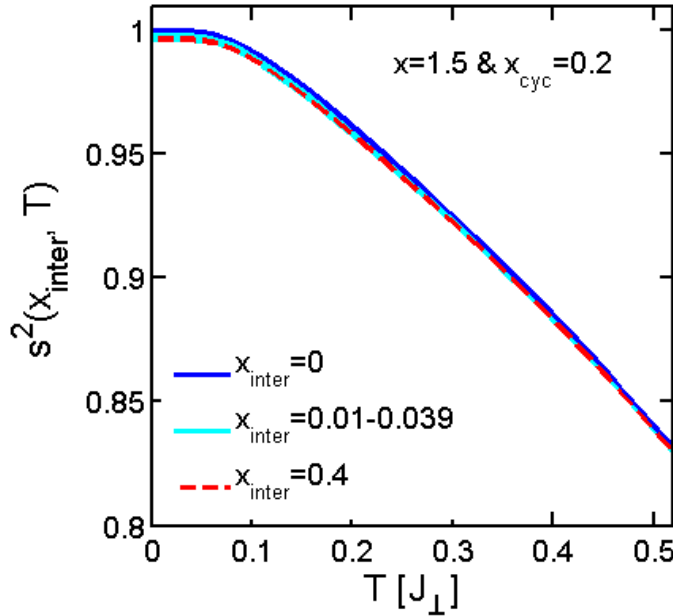

Figure 6.2.6: Trellis lattice coupling of ladders: Singlet occupation number for $x = 1$ and $x_{\mathrm{cyc}} = 0$ as a function of temperature in units of the rung coupling $J_{\perp}$. The dark blue solid line presents the result for the isolated ladder $x_{\mathrm{inter}} = 0$ and the red dashed line for $x_{\mathrm{inter}} = 0.4$. The cyan colored area presents the result for $0 < x_{\mathrm{inter}} < 0.4$.

In the case of an isolated ladder the mean field occupation number considered as a function of the temperature T always equals the value 1 below the characteristic temperature T_{char} (see Chapter 5). In case of an inter-ladder coupling $x_{\mathrm{inter}} > 0$ the mean field occupation number still remains constant upon increasing temperature below T_{char}, but this constant is now smaller than one with its value depending on the inter-ladder coupling strength $x_{\mathrm{inter}} > 0$ both in the square lattice case and in the situation of a trellis lattice. The possible range of values that $s^2(x_{\mathrm{inter}}, T)$ may assume for $0 \leq T < T_{\mathrm{char}}$ can be deduced from the width of the left part of the cyan colored area in Figs. 6.2.5 and 6.2.6, respectively. For $0 \leq T < T_{\mathrm{char}}$ the largest range of values for the mean field occupation number is obtained. Above the characteristic temperature T_{char} the width of the cyan colored areas shrinks with increasing temperature. For high temperature it converges against the curve for the case of the isolated ladder (blue curve).
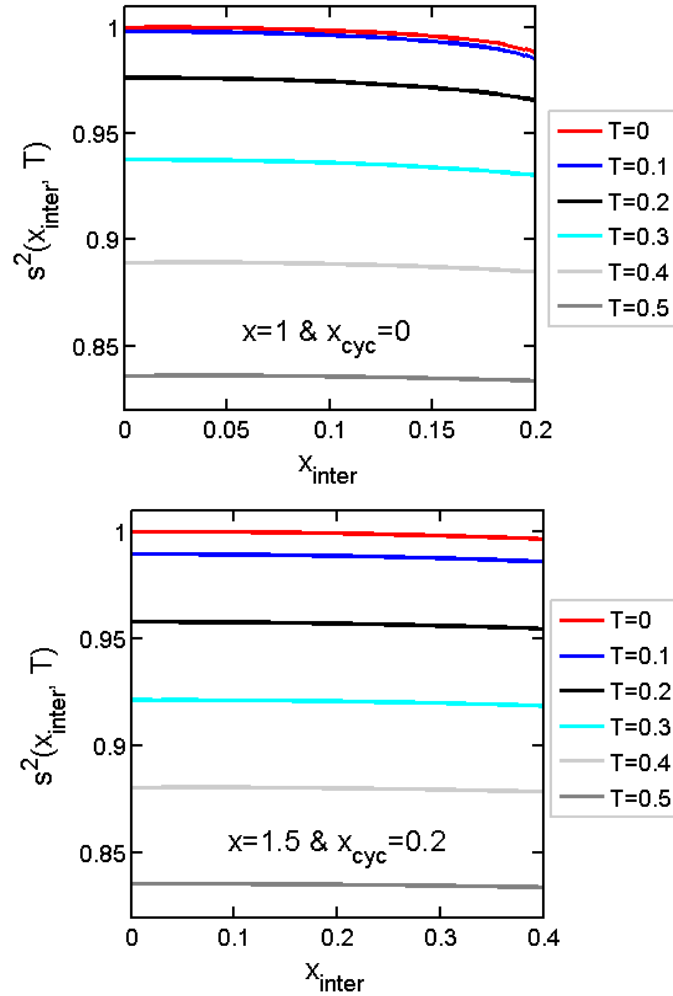
Figure 6.2.7: Singlet occupation number as a function of inter-ladder coupling x_{inter} at constant energies for the square lattice coupling for $x = 1$ with $x_{\text{cyc}} = 0$ (upper panel) and the trellis lattice coupling for $x = 1.5$ with $x_{\text{cyc}} = 0.2$ (lower panel). The slope of each curve becomes the less the larger the energy is.

Comparing both cases to each other shows that, at finite temperature the effect of inter-ladder coupling for a certain value of x_{inter} influences the spin gap stronger in the square lattice case than in the trellis lattice case. However, for the trellis lattice only a small range of possible x_{inter} is presented at finite temperature. The possible scale for values of x_{inter} in the trellis lattice case reaches up to the order of $x_{\text{inter}} \sim 1$ and larger. We present such a small range of x_{inter} for the trellis lattice, in order to point out that the underlying

lattice geometry plays an important role on the scale of the inter-ladder coupling x_{inter}.

In Fig. 6.2.7 the mean field occupation number is presented as a function of the inter-ladder coupling x_{inter} at various constant energies. The upper panel of Fig. 6.2.7 shows the result for the square lattice coupling of ladders and the lower panel for the trellis lattice coupling of ladders. The slope of the curves becomes the less the larger the energy is indicating the convergence torwards the case of the isolated ladder.

Comparing the width of the cyan colored areas of Fig. 6.2.5 and 6.2.6 as well as the slope of the curves in the panels of Fig. 6.2.7 reflects that the inter-ladder coupling of ladders in the square lattice case at a certain value of x_{inter} affects the physical properties of the system stronger than in the trellis lattice case even at finite temperature.

6.3 A comparison to experiment

In Ref. [4] an interesting effect of the one-triplon spectral weight due to a frustrated trellis lattice inter-ladder coupling was introduced. Schmidt and Uhrig derived in Ref. [4] the two dimensional one-triplon spectral weight according to

$$a_{SU}^2(k,h) = 2\sin^2\left(\pi h \frac{a}{2a_2}\right) a^2(k) \frac{\omega_0(k)}{\omega(k,h)}, \tag{6.3.1}$$

where the sine factor stems from the interference of the excitation processes from the left and the right spin on each rung [4]. The sine reflects the odd parity on the isolated ladder with respect to reflections about the centerline. Note, this one-triplon spectral weight does not contain the conditional excitations treated in Chapter 5. It only accounts for the first excited states - the first triplon. In order to employ this one-triplon spectral weight for our treatment the formula has to be modified. Due to the inclusion of the hardcore constraint on the mean field level we obtain

$$a^2(k,h) = 2\sin^2\left(\pi h \frac{a}{2a_2}\right) a^2(k) s^2(T, J_{\text{inter}}) \frac{\omega_0(k,s)}{\omega(k,h,s,J_{\text{inter}})} . \tag{6.3.2}$$

The approximated ratio of the two lattice constants in the sine factor is $a_2 = 1.5a$ [4] giving a factor of $\sin^2(\frac{\pi h}{3})$.

Schmidt and Uhrig [4] found in their mean field treatment that a change from anti-ferromagnetic to ferromagnetic inter-ladder coupling $|x_{\text{inter}}| \rightarrow -|x_{\text{inter}}|$ leads to the same curves where the momentum h is changed to $h + 1$ [4]. Thus, with increasing x_{inter} the shifting of the maximum position of $a_{SU}^2(k, h)$ away from $k = 0.5$ increases. Here the sign of x_{inter} plays an important role, because for a negative x_{inter} the spectral weight is shifted to the left from $k = 0.5$ at $h = 1$. At $h = 2$ it is shifted to the right away from $k = 0.5$. In the case of $x_{\text{inter}} > 0$ the shifting direction appears vice versa. As the strength of this shift depends on the size of the inter-ladder coupling, this effect serves for determining the inter-ladder coupling constant in real materials such as $La_4Sr_{10}Cu_{24}O_{41}$.

In Chapter 5 we compared the temperature dependent self-consistent mean field solution for the isolated spin ladder to INS data measured for the undoped ladder $La_4Sr_{10}Cu_{24}O_{41}$. We found that the coupling for $x = 1.5$ and $x_{\text{cyc}} = 0.2$ fits the data very well.

Hence, we present the spectral weight for $x = 1.5$ and $x_{\text{cyc}} = 0.2$ computed by Eq. 6.3.2 in Fig. 6.3.1 at two different temperatures. The left panel of Fig. 6.3.1 shows the result for zero temperature, where the right panel shows the result at a temperature of $T = 0.2J_{\perp}$, which is about 150K. Thus, the selected temperatures agree with the ones, that were measured. With increasing temperature the amplitude of the spectral weight decreases only slightly because conditional excitations are not considered in Eq. 6.3.2. Effects due to quantum fluctuations are not observed.

In the following we clarify the sign and the size of the two-dimensional inter-ladder coupling by studying the INS spectra of $La_4Sr_{10}Cu_{24}O_{41}$ at $q_h = 1$ and $q_h = 2$ as proposed in [4].

Hence, constant q_h-cuts from the INS data introduced in Chapter 5 with an initial energy of 50meV are made for $0.7 < q_h < 1.3 \frac{2\pi}{a}$ and $1.7 < q_h < 2.3 \frac{2\pi}{a}$ at temperatures of 15K and 150K.

The result is presented in Fig. 6.3.2. Gaussians are fitted to the data providing information on the positions of the peaks. These peak positions as well as the relative shift Δk to each other are summarized in Table 6.3. The blue vertical dashed lines are a guidance for the eyes in order to help in revealing the shift. Along the k-component that corresponds to the q_l[1] component in the experimental data, a shift of the maximum

---

[1]According to standard notation in neutron spectroscopy we will now use q_l to indicate the momentum
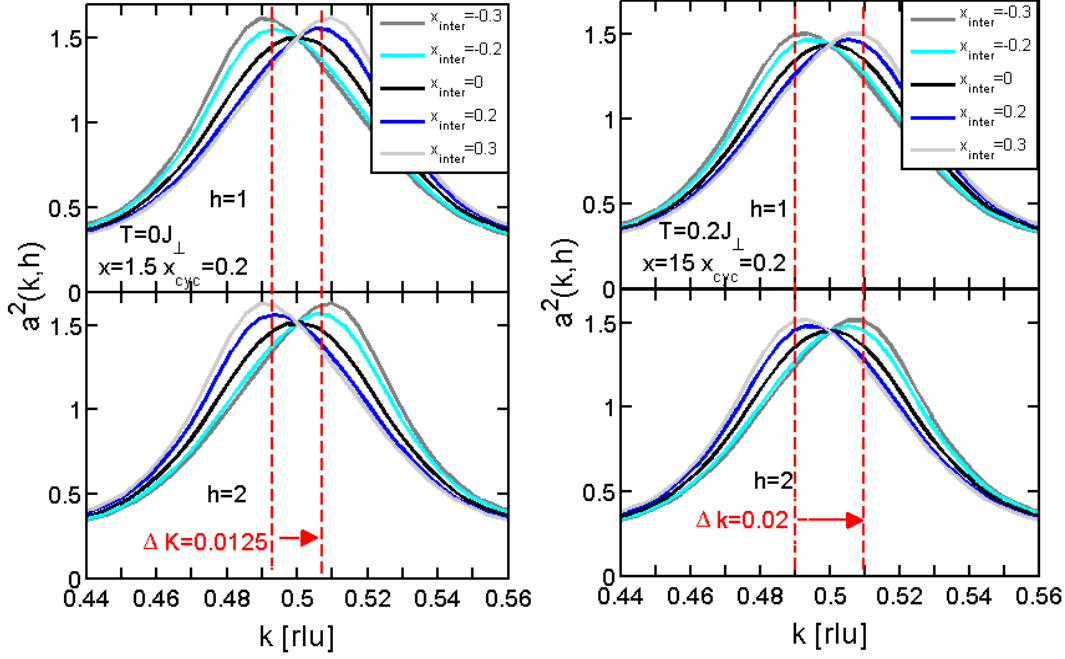
Figure 6.3.1: One-triplon spectral weight at zero temperature (left panel) and at about $150K$ (right panel) for $x = 1.5$ and $x_{\text{cyc}} = 0.2$ computed with Eq. 6.3.2. The width between the red dashed vertical lines represent the shift along $k = q_l$ extracted from the INS data of $La_4Sr_{10}Cu_{24}O_{41}$.

peak position is observed. At a temperature of $15K$ (left panels) the maximum along the q_l-component is shifted by $\Delta q_l = 0.01 - 0.015\frac{2\pi}{c}$ and at $150K$ (right panels) by $\Delta q_l = 0.02\frac{2\pi}{c}$ (for more details see Table 6.3).

	$q_{l,-}^{max}$ $[\frac{2\pi}{c}]$, 15K	$q_{l,+}^{max}$ $[\frac{2\pi}{c}]$, 15K	$q_{l,-}^{max}$ $[\frac{2\pi}{c}]$, 150K	$q_{l,+}^{max}$ $[\frac{2\pi}{c}]$, 150K
$h = 1\frac{2\pi}{a}$	-0.485 ± 0.001	0.475 ± 0.001	-0.48 ± 0.002	0.475 ± 0.003
$h = 2\frac{2\pi}{a}$	-0.5 ± 0.005	0.485 ± 0.003	-0.5 ± 0.004	0.475 ± 0.004
$\Delta q_l \frac{2\pi}{c}$	0.015 ± 0.005	0.01 ± 0.003	0.02 ± 0.004	0

Table 6.3: Positions of the peak maxima and the resulting shift presented in Fig. 6.3.2.

As the peak maximum for $q_h = 1$ lies at a smaller $q_{l,+}$ as for $q_h = 2$, the shift indicates a ferromagnetic coupling and thus $x_{\text{inter}} < 0$.

---

component along the ladder instead of k.
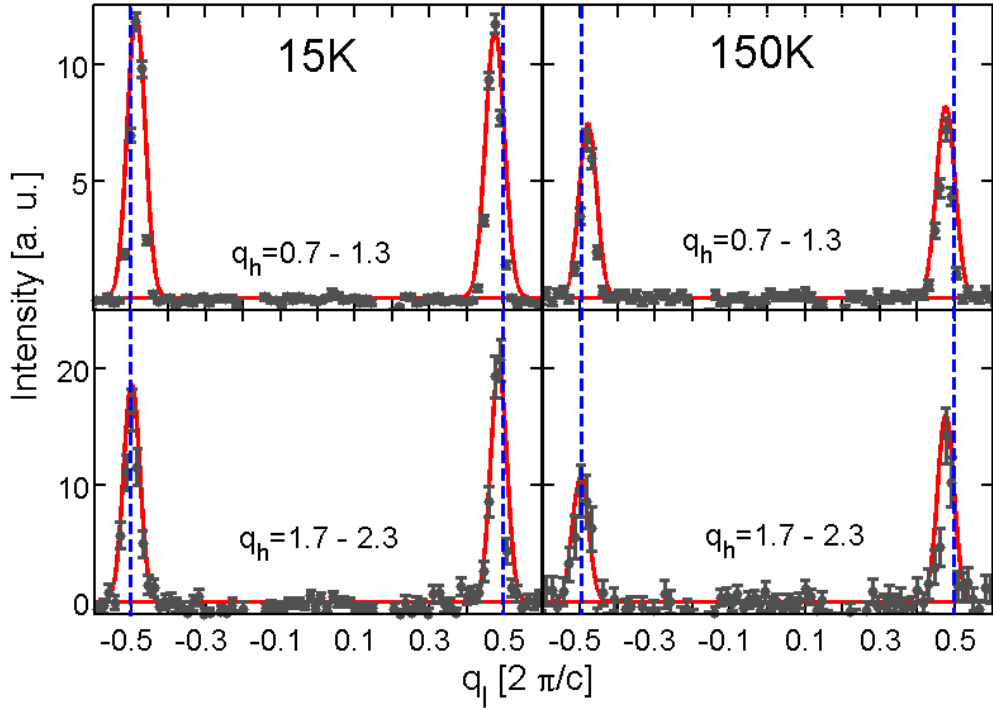
Figure 6.3.2: Extracted data of $La_4Sr_{10}Cu_{24}O_{41}$. Left panels show data at a temperature of 15K and right panels of 150K. Gaussians are fitted to the data providing information on the positions of the peaks. These peak positions are summarized in Table 6.3. A shift of the maxima along momentum component $k = q_l$ results when shifting from $h = 1$ to $h = 2$. The blue vertical dashed lines at $q_l = \pm 0.5$ are a guidance for the eyes in order to help in revealing the shift. At a temperature of 15K (left panels) the maximum is shifted by $\Delta q_l = 0.01 - 0.015 \frac{2\pi}{c}$ and of 150K (right panels) by $\Delta q_l = 0.02 \frac{2\pi}{c}$.

For comparison with theory, the extracted shifts obtained from the fitting of a Gaussian to the data at 15K and 150K of $h\Delta q_l = 0.0125 \pm 0.005 \frac{2\pi}{c}$ and $\Delta q_l = 0.02 \pm 0.004 \frac{2\pi}{c}$, respectively, are indicated in Fig. 6.3.1 by the spacing between the two dashed vertical red lines in each panel. This spacing is overlaid with the curves obtained for the confirmed parameter set of $x = 1.5$ and $x_{cyc} = 0.2$ presented in Chapter 5. This shift indicated by the spacing between the red dashed vertical lines is positioned equally around $k = 0.5$. At 15K the red lines intersect with the maximum positions of the curves for $hx_{inter} = -0.2 \pm 0.05$, whereas for 150K the slightly larger shift intersects with the curves for $hx_{inter} = -0.3 \pm 0.05$.

In summary, from the maximum peak positions of the cuts at $q_h = 1$ and $q_h = 2$ we find a ferromagnetic coupling, when compared to the theoretical peak positions derived in Ref [4]. From the width of the shift Δq_l we conclude that this ferromagnetic inter-ladder coupling is of the order of $hx_{\text{inter}} = -0.2 \pm 0.05$ at 15K and of the order of $hx_{\text{inter}} = -0.3 \pm 0.05$ at 150K both for parameters $x = 1.5$ and $x_{\text{cyc}} = 0.2$. In Chapter 5 we determined $J_\perp = 115$meV and therefore we obtain a ferromagnetic inter-ladder coupling of $hJ_{\text{inter}} = (-23 \pm 6)$meV at 15K and of $hJ_{\text{inter}} = (-36 \pm 6)$meV at 150K, which agrees with the findings for inter-ladder coupling of $hJ_{\text{inter}} = (-36 \pm 6)$meV found for $La_4Sr_{10}Cu_{24}O_{41}$ by Notbohm [1]. Notbohm extracted the dispersion from the data. By fitting the theoretical curve to the data the ferromagnetic inter-ladder coupling was determined. Furthermore, based on a quantum chemistry calculation it is argued that a ferromagnetic inter-ladder coupling $x_{\text{inter}} \approx -0.2$ is present in the compound $SrCu_2O_3$ [104].

The discrepancy of the inter-ladder coupling for 15K and 150K might indeed be a physical effect. Though the ladder $La_4Sr_{10}Cu_{24}O_{41}$ represents an example of an undoped ladder, the compound contains holes, which reside on the chains. However, experimental studies on the doping level reveal, that the hole distribution in such compounds is a function of temperature [9]. Thus, at higher temperatures holes might also reside in the ladders, which in turn affects the inter-ladder coupling x_{inter}. However, because of the error of $h0.05x_{\text{inter}}$ we cannot clearly conclude whether there is a temperature effect on the inter-ladder coupling or not.

6.4 Conclusions

Starting from the PCUT result for the effective one-triplon dispersion a mean field approach including the hardcore interaction is performed in order to investigate the significance and the strength of inter-ladder coupling. This approach is implemented both in the zero temperature case and at finite temperature for both the square and the trellis lattice coupling.

For zero temperature we showed that the temperature dependent integral assumes the value zero for each inter-ladder coupling x_{inter}, so that only the term describing the pure quantum fluctuations remains. At $T = 0$K we find that the singlet occupation number

for the square lattice only slightly deviates from one with minimum value $s^2 = 0.988$. For the square lattice, this results in a closure of the spin gap at an only slightly increased inter-ladder coupling by $3 - 4\%$. These findings concerning the closure of the spin gap are below all values found in the literature [37, 38].

For the trellis lattice coupling we find that the spin gap as a function of inter-ladder coupling x_{inter} is also decreasing, which is in agreement with Ref. [4]. However, in contrast to the square lattice the quantum fluctuations influence the closure of the spin gap in a much stronger way. We find an enlarged critical value of inter-ladder coupling up to 21%. These findings do not agree with the the results presented by Gopalan et al. [38] who argued that the spin gap in the trellis lattice remains open.

In addition, we find that the effect of inter-ladder coupling decreases with increasing temperature. It converges towards the case of isolated ladders in the high temperature limit. Furthermore, the effect of an inter-ladder coupling is not affected by temperature from zero up to the characteristic temperature T_{char} introduced in Chapter 5. The mean field singlet occupation number depends more sensitively on the inter-ladder coupling strength x_{inter} in case of the square lattice. However, the scale of possible inter-ladder couplings is found to be larger for the trellis lattice than for the square lattice.

Finally for an inter-ladder coupling of h$x_{\text{inter}} = -0.2 \pm 0.05$ at 15K and of h$x_{\text{inter}} = -0.3 \pm 0.05$ at 150K for $x = 1.5$ and $x_{\text{cyc}} = 0.2$ a ferromagnetic inter-ladder coupling of h$J_{\text{inter}} = -23 \pm 6$meV and h$J_{\text{inter}} = -36 \pm 6$meV could be determined from INS data for $La_4Sr_{10}Cu_{24}O_{41}$ in the way proposed in Ref. [4]. These findings agree with the value of the inter-ladder coupling found in Ref. [1]. It is argued that the different inter-ladder couplings for the two different temperatures could be an effect of hole redistribution at high temperature [9]. However, hthe error bars leave the question unanswered whether the temperature effect is real or not.

Chapter 7

Features of hole doped ladders

Doping spin liquids is a major goal for condensed matter physics as rich new physics is expected to arise from charge and spin pairing effects. However, to-date, the study of doped spin liquids has been hampered by difficulties in obtaining suitable systems and also in making sense of the complex physics of spin and charge involved. Here, we revisit the most promising systems to date, the cuprate spin ladders.We investigate the influence of hole doping on the magnetic scattering amplitude in cuprate spin ladders using inelastic neutron scattering.

Three samples each with a different estimated doping level $\delta = 0; 0.03; 0.06$ are studied below and above the charge ordering temperature of about 60K of $Sr_{2.5}Ca_{11.5}Cu_{24}O_{41}$. The spectra of the doped ladders are compared with the undoped ladder spectrum with $\delta = 0$. The spin gap is characteristic for all two-leg ladders [105]. In our experiment, however, we observe further spectral features besides the triplon gap, that are only present in the doped ladders. Therefore these two features are proposed to originate from the presence of holes.

At low temperatures, where a Wigner Hole Crystal (WHC) state forms, the dynamics show a highly dispersive and gapped excitation spectrum of triplons which closely resemble the undoped case but modified by a new lifetime broadening. In addition to the gapped triplons, subgap states extending down to 8meV appear. When the material is heated to the conducting state the triplons damp out strongly and the 8meV gap disappears leaving a gapless excitation spectrum. These phenomena are discussed in terms of both resonating valence bond [39] physics and charge segregation into hole-rich and hole-poor ladders due to Coulomb effects, which leads to the stripe ordering theory [14].

However, quantitative theoretical results for comparison with the measured data are not available, therefore the explanation of the results will remain qualitatively.

7.1 Materials

As already mentioned in Chapter 1 the parent material of the cuprate spin ladder is $Sr_{14}Cu_{24}O_{41}$, which is intrinsically hole doped with nearly all holes located in the chain [23]. Hole doping of the ladder is achieved by substitution of Ca^{2+} for Sr^{2+}. Because of the smaller ionic radius of Ca^{2+} [26, 24] the holes are transferred from the chain into the ladder. The amount of transferred holes depends on the amount of Ca^{2+} substitution. In contrast, a substitution with La^{3+} ions tremendously reduces the total number of holes according to its stoichiometry to

$$41 \cdot 2 - 24 \cdot 2 - 10 \cdot 2 - 4 \cdot 3 = 2$$

holes, which are mainly in the chains, so that the ladder $La_4Sr_{10}Cu_{24}O_{41}$ can be regarded as without holes.

The undoped ladder $La_4Sr_{10}Cu_{24}O_{41}$ represents a Mott-insulator, whereas the doped ladders resides in a regime between insulator and metal. For $Sr_{2.5}Ca_{11.5}Cu_{24}O_{41}$ resistivity measurements showed a phase in the ladder direction with an almost linear temperature dependence above $130K$ representing the metallic phase and a sharp resistivity increase below $60K$ representing the insulating phase. The insulating phase implies the localization of holes [27, 106, 107].

The interaction between the Cu-spins and the charge mobility of the conduction electrons is believed to play an important role for the mechanism of high temperature superconductivity in cuprates [108].

To study the influence of holes doped into the ladder on the magnetic spectrum, ladders with different doping levels δ are measured by inelastic neutron scattering. In order to conclude which effects result from the presence of holes, a measurement for the undoped ladder $La_4Sr_{10}Cu_{24}O_{41}$ is carried out giving the zero doping $\delta = 0$ reference spectrum. Two doped ladders are studied, $Sr_{2.5}Ca_{11.5}Cu_{24}O_{41}$ with an estimated doping of $\delta = 0.06$ [109] holes per ladder site and $Sr_8Ca_6Cu_{24}O_{41}$ with an estimated doping of $\delta = 0.03$ holes per ladder site.

7.2   Samples and experimental details

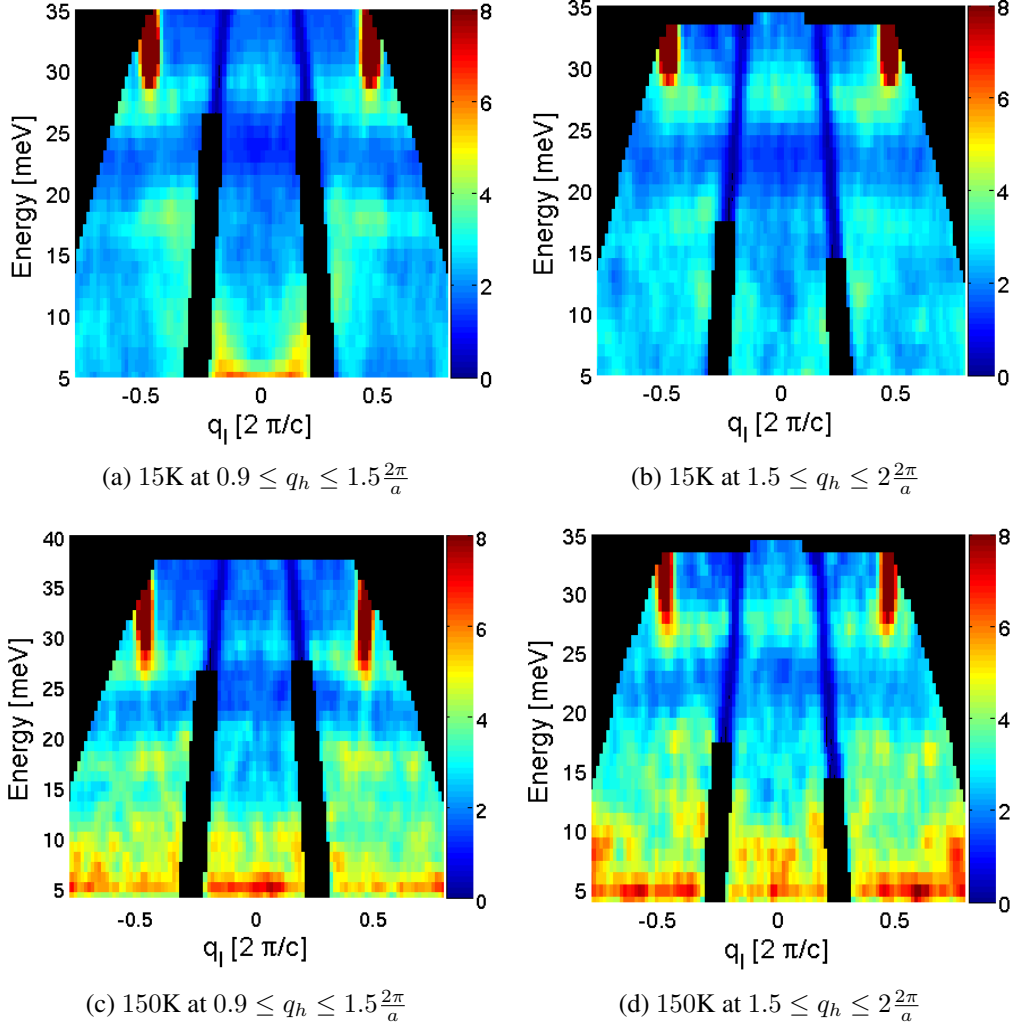In the case of the undoped ladder $La_4Sr_{10}Cu_{24}O_{41}$ the array of crystals already introduced in Chapter 5 was used with a total mass of 23g. For the doped spin-ladder $Sr_{2.5}Ca_{11.5}Cu_{24}O_{41}$ an array of four crystals of total mass 25g was used. Both samples, $La_4Sr_{10}Cu_{24}O_{41}$ and $Sr_{2.5}Ca_{11.5}Cu_{24}O_{41}$, were measured at the MAPS spectrometer at ISIS (for details on the spectrometer see Chapter 2) by Gibson et al. [110] and Notbohm et al. [111] respectively. During each measurement the crystals were mounted in a closed cycle cryostat with the $(0kl)$ reciprocal lattice plane horizontal and the c-axis perpendicular to the incident neutron beam k_i. The third ladder $Sr_8Ca_6Cu_{24}O_{41}$ was measured at MERLIN at ISIS by Mihalik [112]. In this case the sample was an array of two crystals with a total mass of 7.6g. The sample measured on MERLIN was stored in vacuum, and it was connected to the cold head of a closed cycle refrigerator. A Fermi chopper was used to select an incident neutron energy of 50meV and was rotated at a speed of 300 Hz to give an energy resolution at the elastic line of 4.17meV. Data were collected at temperatures of 15K (insulating phase) and 150K (metallic phase). Incoherent nuclear scattering from a vanadium standard was used to normalize the magnetic cross-section (see also Chapter 2). In the following text wavevectors q_l and q_h represent the direction along the ladder and along the rungs, respectively. The lattice spacing on a rung is given by a and along the ladder by c.

7.3   Raw data and background correction

We begin by presenting the measured raw data for all three samples at both temperatures in order to introduce the main properties of the spin ladder cuprates investigated within this work. It should be noticed, that the black areas in the plots arise due to missing detector coverage. As the incoherent scattering strength is very strong for energies between $0 - 4$meV, the data are presented from 5meV upwards.
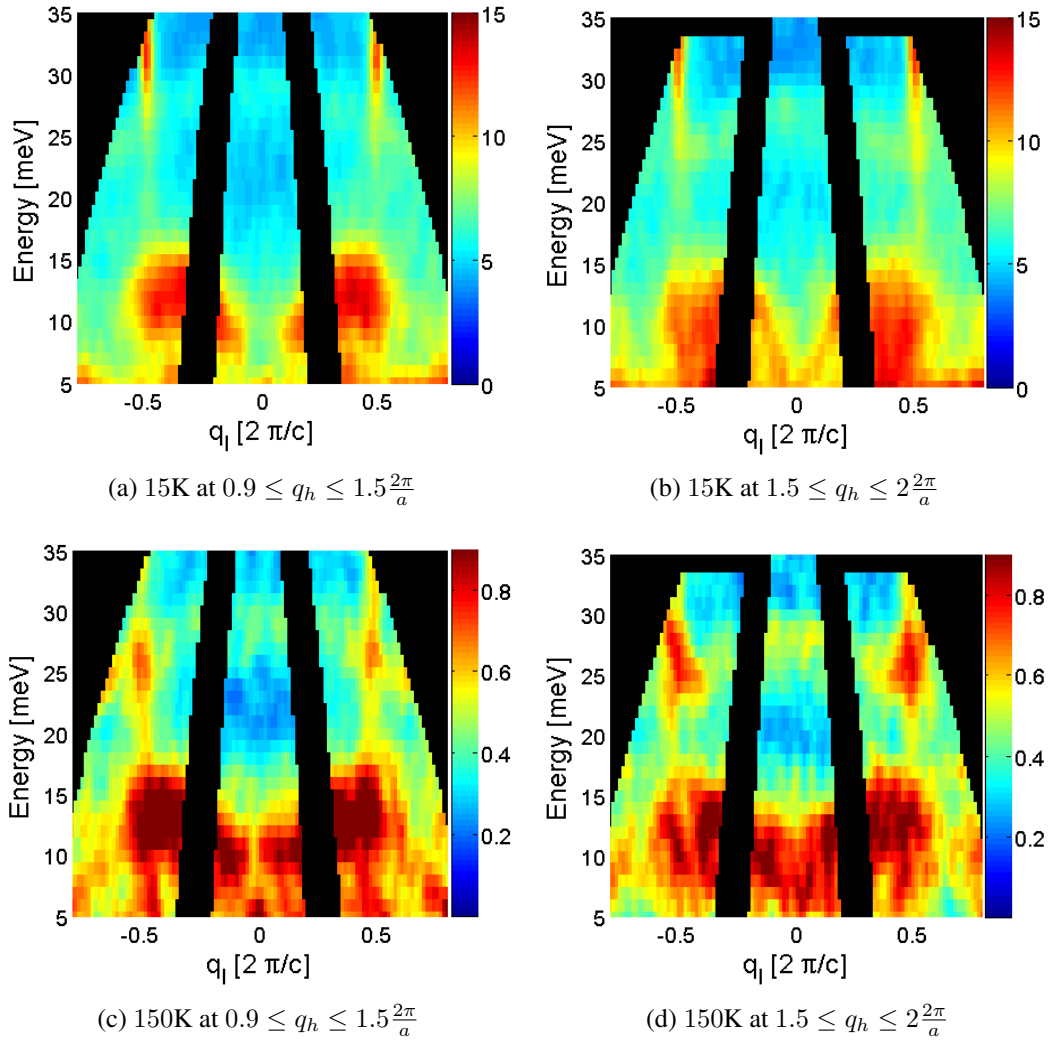
The raw data are given in Figs. 7.3.1 for $La_4Sr_{10}Cu_{24}O_{41}$, 7.3.2 for $Sr_{2.5}Ca_{11.5}Cu_{24}O_{41}$ and 7.3.3 for $Sr_8Ca_6Cu_{24}O_{41}$. They are all divided into two scattering regions. The one with energies between 5meV to 20meV shows the scattering from the chain structure and the one from about 25meV upwards shows the scattering from the ladder structure. We are mainly interested in the second region, corresponding to the ladder. To gain information on the ladder, the background scattering has to be handled properly.

Figure 7.3.1: Raw data measured for $La_4Sr_{10}Cu_{24}O_{41}$ at two different temperatures and averaged over two different narrow regions for the momentum q_h at MAPS by Gibson et al. [110]. Black areas represent regions without detector coverage.
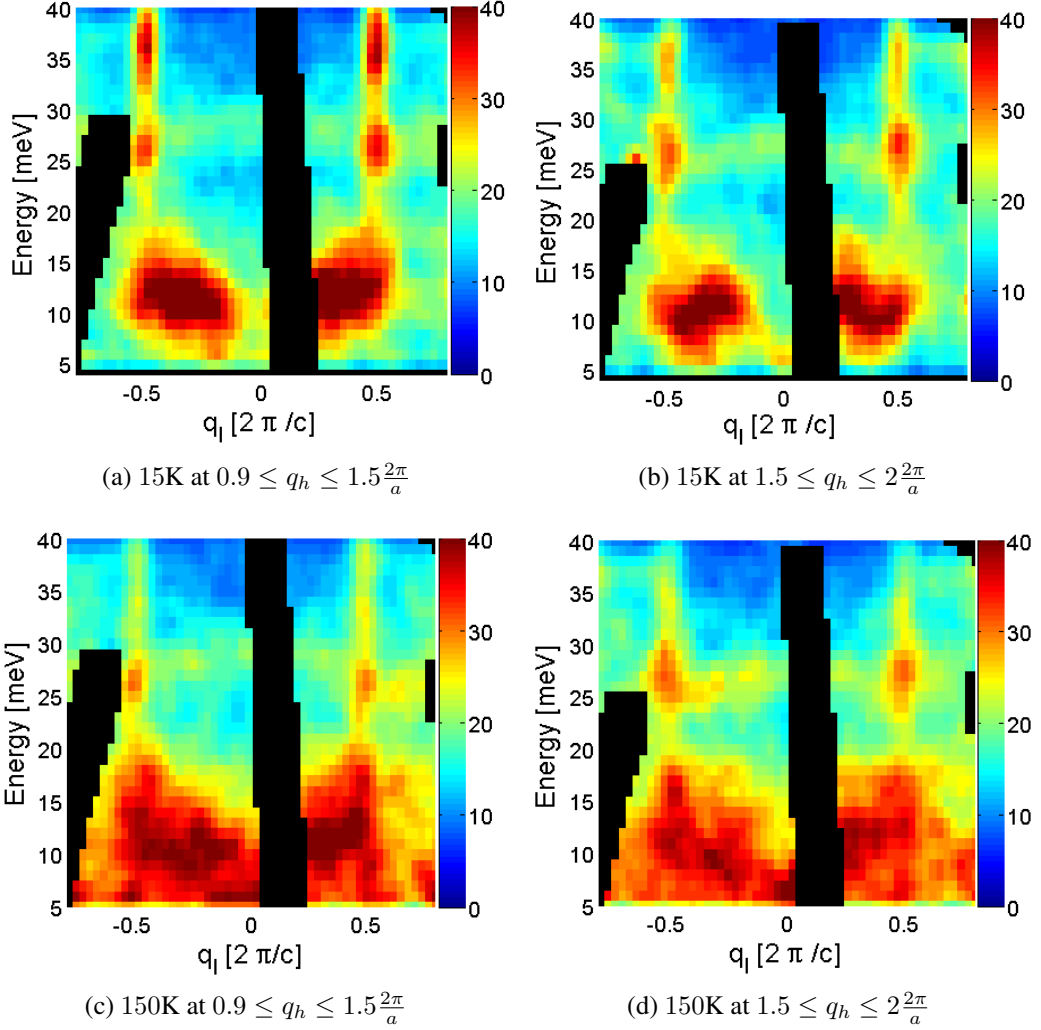

(a) 15K at $0.9 \leq q_h \leq 1.5 \frac{2\pi}{a}$

(b) 15K at $1.5 \leq q_h \leq 2 \frac{2\pi}{a}$

(c) 150K at $0.9 \leq q_h \leq 1.5 \frac{2\pi}{a}$

(d) 150K at $1.5 \leq q_h \leq 2 \frac{2\pi}{a}$

However, the raw data already show that background correction is a challenging task at least for the doped ladders, $Sr_{2.5}Ca_{11.5}Cu_{24}O_{41}$ and $Sr_8Ca_6Cu_{24}O_{41}$, because the background has considerable structure in wavevector and energy from single and multiple phonon scattering in a complicated way. In order to obtain only the magnetic scattering amplitude corresponding to the chain and ladder structure in the materials, we need to correct the data for the background scattering and the scattering due to phonon ex-

Figure 7.3.2: Raw data measured for $Sr_{2.5}Ca_{11.5}Cu_{24}O_{41}$ at two different temperatures and averaged over two different narrow regions for the momentum q_h at MAPS by Notbohm et al. [111]. Black areas represent regions without detector coverage.


(a) 15K at $0.9 \leq q_h \leq 1.5 \frac{2\pi}{a}$

(b) 15K at $1.5 \leq q_h \leq 2 \frac{2\pi}{a}$

(c) 150K at $0.9 \leq q_h \leq 1.5 \frac{2\pi}{a}$

(d) 150K at $1.5 \leq q_h \leq 2 \frac{2\pi}{a}$

citations. The phonon scattering is present in all measurements and is located in the energy range between 20meV and 30meV giving the arc-like shaped intensity along q_l in Figs. 7.3.1, 7.3.2 and 7.3.3. It is clear that the corresponding scattering traces back to a phonon excitation because it shows no pronounced q-dependence. Cuts in momentum space at various energies (not shown) document an intensity dispersing out of a nuclear position, which is typical of a phonon [113].

Figure 7.3.3: Raw data measured for $Sr_8Ca_6Cu_{24}O_{41}$ at two different temperatures and averaged over two different narrow regions for the momentum q_h at MERLIN by Mihalik et al. [112]. Black areas represent regions without detector coverage.

(a) 15K at $0.9 \leq q_h \leq 1.5\frac{2\pi}{a}$

(b) 15K at $1.5 \leq q_h \leq 2\frac{2\pi}{a}$

(c) 150K at $0.9 \leq q_h \leq 1.5\frac{2\pi}{a}$

(d) 150K at $1.5 \leq q_h \leq 2\frac{2\pi}{a}$

In order to account for the total background scattering including phonon scattering various constant q-cuts are performed and interpolated piecewise. The regions where the phonon (between 20meV and 30meV) occurs and no magnetic scattering is present are modeled by fitting polynomials to the data. In the region where magnetic scattering occurs the background was fitted by linear regression. Since the measured intensities in

Figs. 7.3.1, 7.3.2 and 7.3.3 are given in a $m \times n$-intensity-matrix (where m denotes the number of different energy values considered and n the number of different values for the momentum component q_l), in a second step the extracted constant q-cuts are interpolated along q_l by polynomials in order to obtain an intensity mapping of the background including the phonon scattering, that has the same grid as the original $m \times n$-intensity-matrix.

The resulting interpolated background is displayed in Fig. 7.3.4 for each temperature and each compound. The phonon scattering is clearly captured as it can be seen in the panels between 20meV and 30meV by the arc-shaped intensity. From the color scale of the intensity plots, one realizes, that the background scattering increases with temperature in a non-linear way. Therefore a background correction has to be done for each intensity map. Removing these backgrounds (Fig. 7.3.4) from the raw data as shown previously in Figs 7.3.1, 7.3.2 and 7.3.3 by subtraction reveals the pure magnetic scattering amplitudes in all three compounds at both temperatures of 15K and 150K.

Figure 7.3.4: Interpolated background for $La_4Sr_{10}Cu_{24}O_{41}$ (top), $Sr_{2.5}Ca_{11.5}Cu_{24}O_{41}$ (middle) and $Sr_8Ca_6Cu_{24}O_{41}$ (bottom) at 15K (left panels) and 150K (right panels).
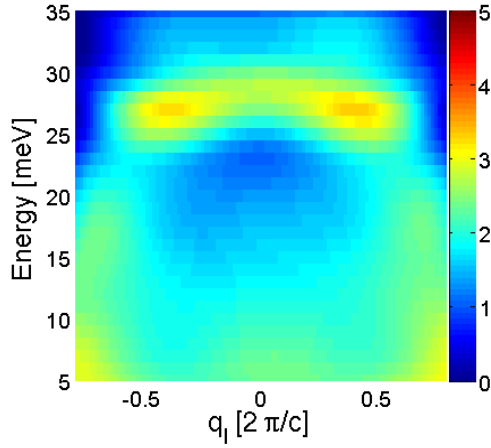
(a) Background for $La_4Sr_{10}Cu_{24}O_{41}$ at 15K
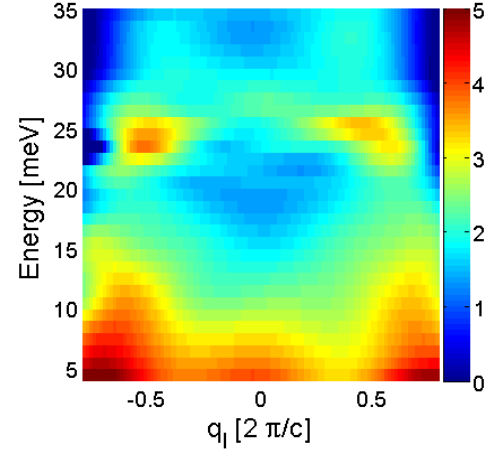
(b) Background for $La_4Sr_{10}Cu_{24}O_{41}$ at 150K
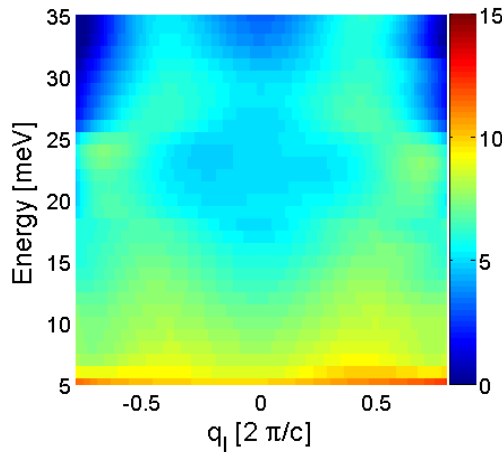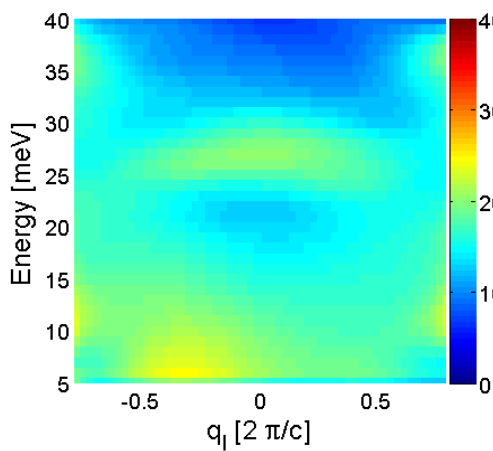
(c) Background for $Sr_{2.5}Ca_{11.5}Cu_{24}O_{41}$ at 15K
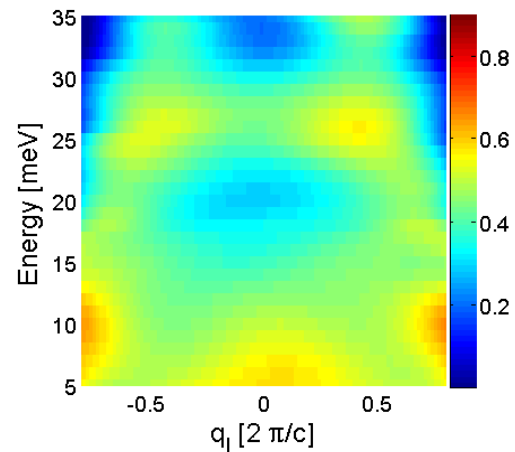
(d) Background for $Sr_{2.5}Ca_{11.5}Cu_{24}O_{41}$ at 150K

(e) Background for $Sr_8Ca_6Cu_{24}O_{41}$ at 15K
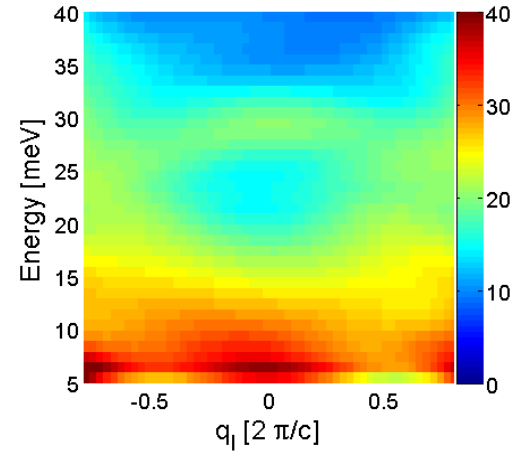
(f) Background for $Sr_8Ca_6Cu_{24}O_{41}$ at 150K

7.4 Data analysis

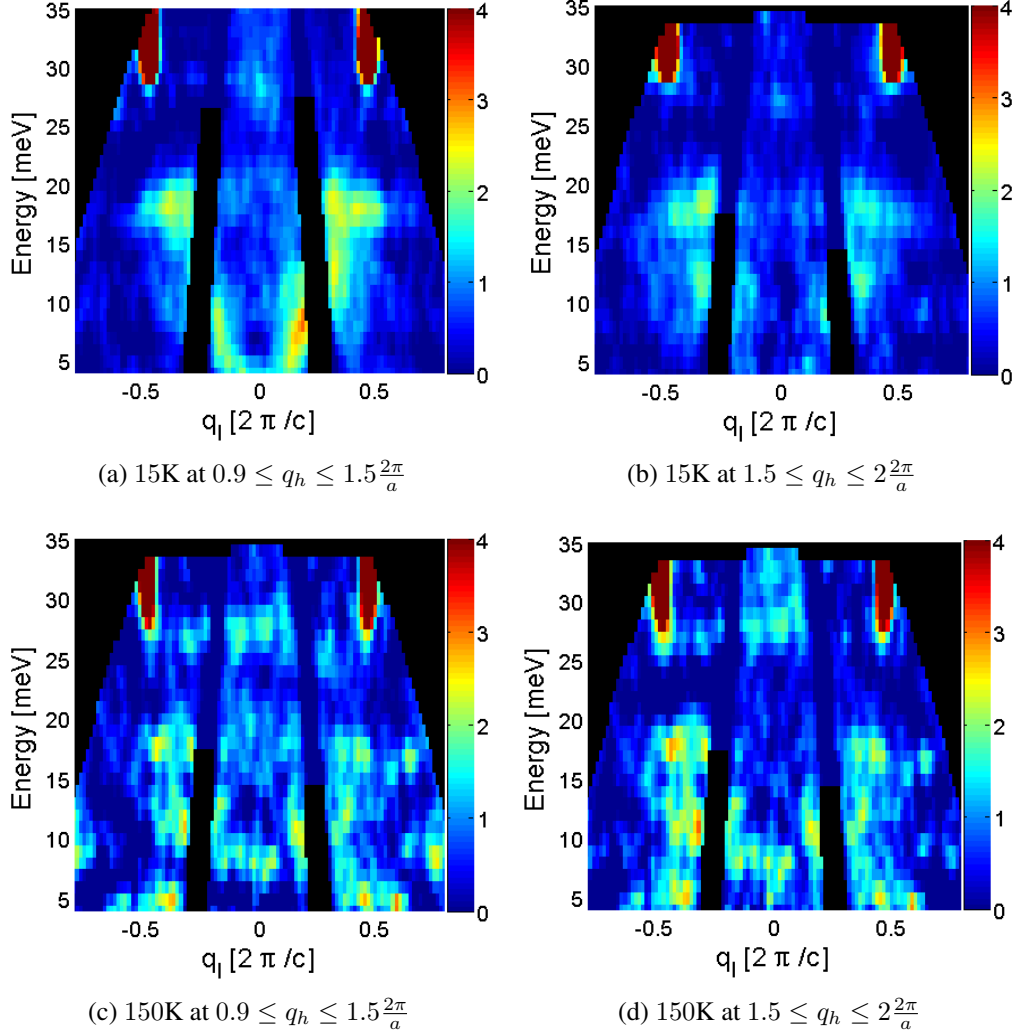### 7.4.1 Background corrected data

The background corrected data for $La_4Sr_{10}Cu_{24}O_{41}$ are presented in Fig. 7.4.1 at 15K (upper panels) and 150K (lower panels) averaged over the momentum ranges $0.9 \leq q_h \leq 1.5\frac{2\pi}{a}$ (left panels) and $1.5 \leq q_h \leq 2\frac{2\pi}{a}$ (right panels). The corrected data show the two different areas of magnetic scattering related to ladder and chain substructure, respectively.

The scattering occuring between 4meV and 20meV and along $-0.5 < q_l < 0.5\frac{2\pi}{c}$ traces back to the chain structure of $La_4Sr_{10}Cu_{24}O_{41}$. From the two dimensional color-plot in Fig. 7.4.1 one sees, that the scattering strength of the chain is a little larger at $0.9 \leq q_h \leq 1.5\frac{2\pi}{a}$ than at $1.5 \leq q_h \leq 2\frac{2\pi}{a}$. This already shows the q-dependence of the chain signal. At 15K the chain dispersion along q_l is clearly visible with its minimum at $q_l = 0$. This observation is in accordance with the findings presented earlier in [109]. An interesting feature of the chain dispersion is its intensity dip at 15meV possibly originating from the presence of ordered holes in the chain in $La_4Sr_{10}Cu_{24}O_{41}$, which locally destroy the magnetic order of the chains. At high temperature (lower panels of Fig. 7.4.1) the chain dispersion loses its shape resulting in a broadened feature as a function of energy from 20meV downwards at $q_l = -0.415\frac{2\pi}{c}$ and $q_l = 0.425\frac{2\pi}{c}$ respectively.

A constant q-cut along this region is presented in Fig. 7.4.2 for 15K (left panel) and 150K (right panel), where the red lines are polynomial fits. Both plots have a peak between 15meV and 20meV in common. At high temperature (150K) there is at least one further peak between $8 - 14$meV and a trend towards increasing intensity at even lower energies. In the 15K measurement this second peak and the intensity increase with decreasing energy is not present. Here, the dispersion is arc-shaped with its minimum at $q_l = 0$ (see Fig. 7.4.1). We only see a continuously decreasing intensity with decreasing energy. In conclusion, the magnetic spectrum of the chains is influenced by the holes. Thermally activated the ordered holes might delocalize at high temperature influencing the magnetic order. For the time being, it cannot be excluded that the extracted feature of the chain scattering at 150K is an artifact resulting from the background correction. Further investigations are required to judge, if the rise of the magnetic scattering inten-

Figure 7.4.1: Background corrected data for $La_4Sr_{10}Cu_{24}O_{41}$ at two different temperatures and two different momenta q_h showing the magnetic ladder and chain scattering only. Due to the strong incoherent scattering between 0meV and 4meV the magnetic scattering can only be extracted for $E \geq 5$meV.

(a) 15K at $0.9 \leq q_h \leq 1.5\frac{2\pi}{a}$

(b) 15K at $1.5 \leq q_h \leq 2\frac{2\pi}{a}$

(c) 150K at $0.9 \leq q_h \leq 1.5\frac{2\pi}{a}$

(d) 150K at $1.5 \leq q_h \leq 2\frac{2\pi}{a}$

sities with decreasing energies and increasing temperature is a real physical effect or not.

The chain scattering is clearly distinguished from the ladder scattering, that arises as a function of energy as a strong intensive stripe located at $q_l = \pm 0.5\frac{2\pi}{c}$ from 30meV upwards. The ladder scattering of $La_4Sr_{10}Cu_{24}O_{41}$ has a much stronger scattering strength than the chain scattering as can directly be seen from the intensity scale of Fig. 7.4.1.
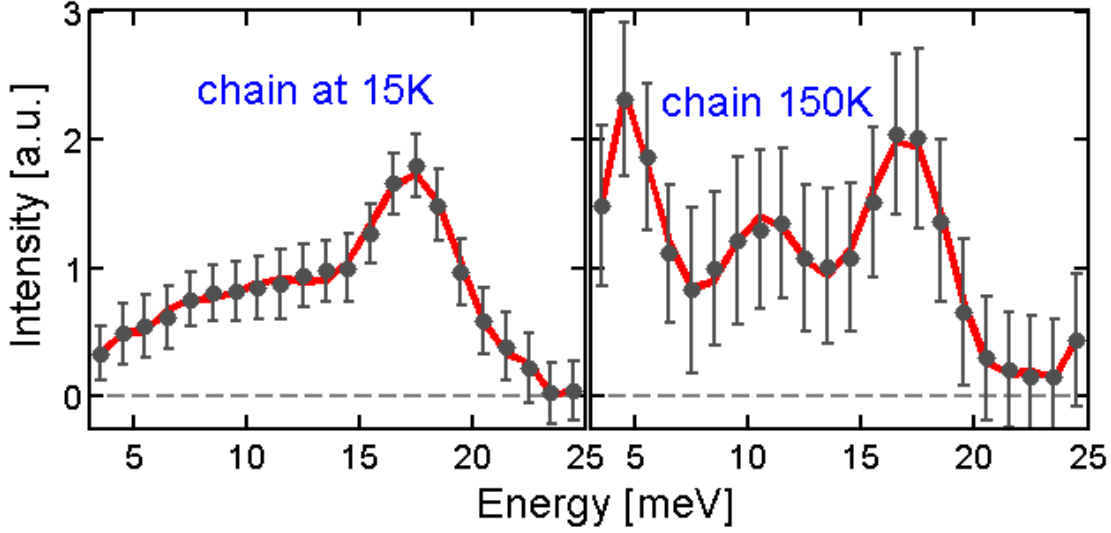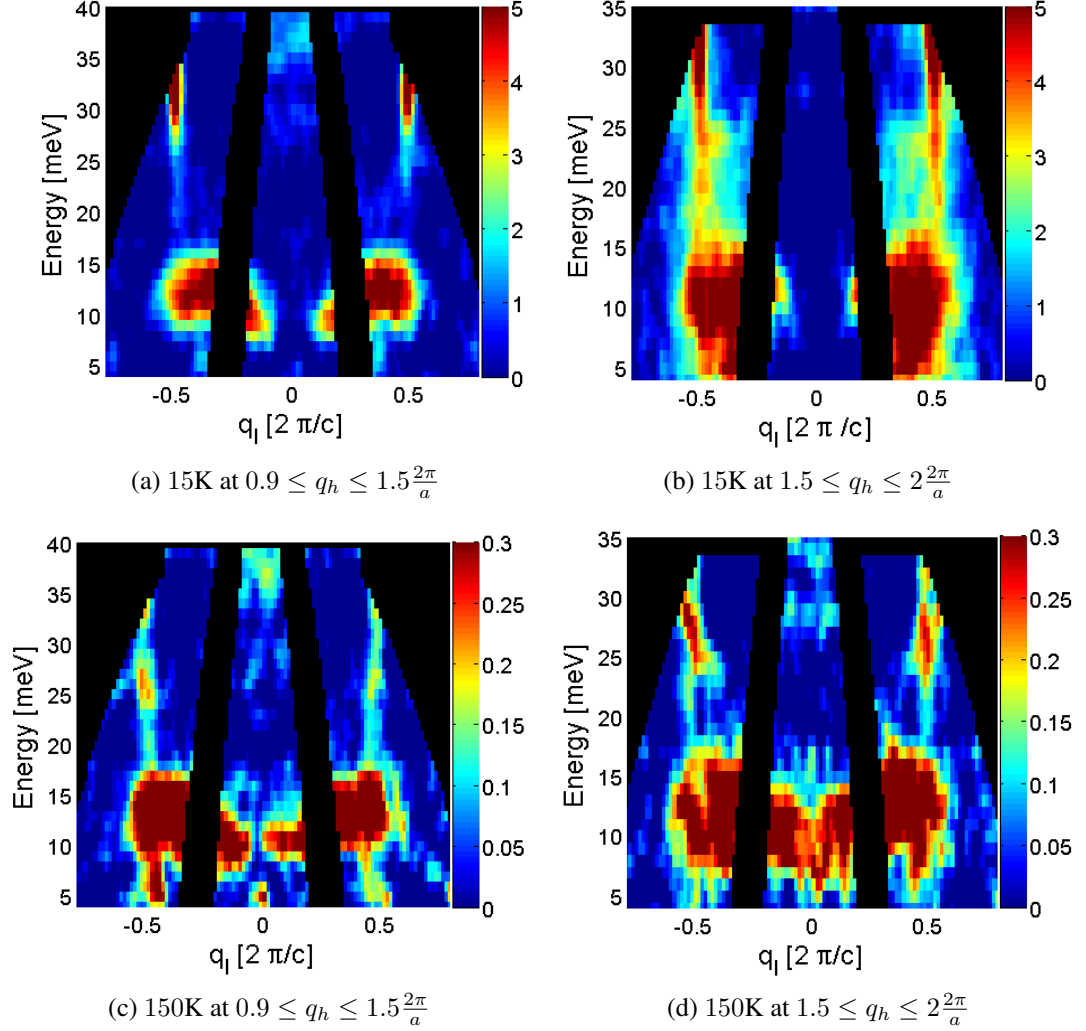
Figure 7.4.2: Chain scattering extracted from the background corrected data of $La_4Sr_{10}Cu_{24}O_{41}$ from Fig. 7.4.1 for 15K (left panel) and 150K (right panel) with $0.9 < q_h < 2\frac{2\pi}{a}$. Along q_l two ranges, $-0.43 < q_l < -0.40\frac{2\pi}{c}$ and $0.41 < q_l < 0.46\frac{2\pi}{c}$ are summed over. The red lines represent polynomial fits revealing a multi peak-dip structure at high temperature.

That ladder scattering and chain scattering are separating apart is obvious in Fig. 7.4.1 because of the intensity decrease between $20 < E < 30$meV in the data. A constant q-cut for the ladder scattering with a detailed analysis will be presented later.

Now we turn to the background corrected data of $Sr_{2.5}Ca_{11.5}Cu_{24}O_{41}$ that are presented in Fig. 7.4.3 showing the ladder and the chain scattering. Comparing the two intensity maps for 15K, we see, that the chain signal in the energy range from $4-20$meV changes tremendously with q. In comparison to $La_4Sr_{10}Cu_{24}O_{41}$ there is no sharp chain dispersion, but two strong drop shaped intensity patches.

The scattering amplitude of the ladder is characterized by a strongly q-dependent (located at $q_l = \pm 0.5\frac{2\pi}{c}$) intensity stripe starting from 30meV upwards. Additionally we see ladder intensity from 30meV extending down towards the region of chain scattering located at lower energies. The intensity found at $1.5 < q_h < 2\frac{2\pi}{a}$ (right panel) is stronger than at $0.9 < q_h < 1.5\frac{2\pi}{a}$ (left panel). At $1.5 < q_h < 2\frac{2\pi}{a}$ one might think of hybridisation of the ladder with the chain because the ladder intensity enters the energy region of chain scattering. Thus for the ladder intensity an additional energy gap, the
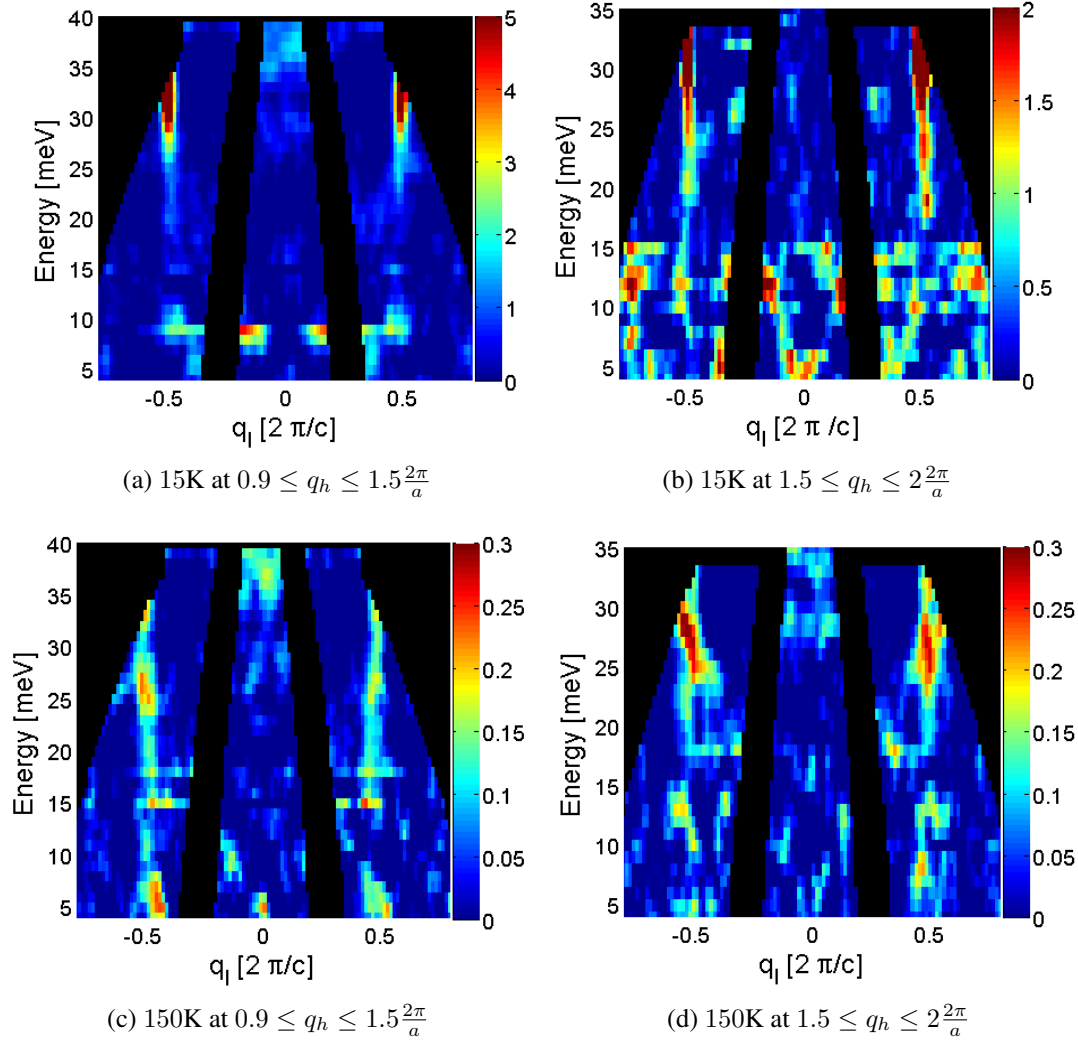
Figure 7.4.3: Background corrected data for $Sr_{2.5}Ca_{11.5}Cu_{24}O_{41}$ at two different temperatures and two different momenta q_h showing the magnetic ladder and chain scattering only.

(a) 15K at $0.9 \leq q_h \leq 1.5\frac{2\pi}{a}$

(b) 15K at $1.5 \leq q_h \leq 2\frac{2\pi}{a}$

(c) 150K at $0.9 \leq q_h \leq 1.5\frac{2\pi}{a}$

(d) 150K at $1.5 \leq q_h \leq 2\frac{2\pi}{a}$

subgap, results. However, in Fig. 7.4.3 this subgap cannot be seen because of the chain scattering lying on top. The same is true for the high temperature experiment presented in the panels at the bottom of Fig. 7.4.3. Here, the intensity shift towards the chain is even more pronounced. Additionally, the second energy gap of the ladder closes, which can be clearly seen at $0.9 < q_h < 1.5\frac{2\pi}{a}$ (left panel at the bottom).
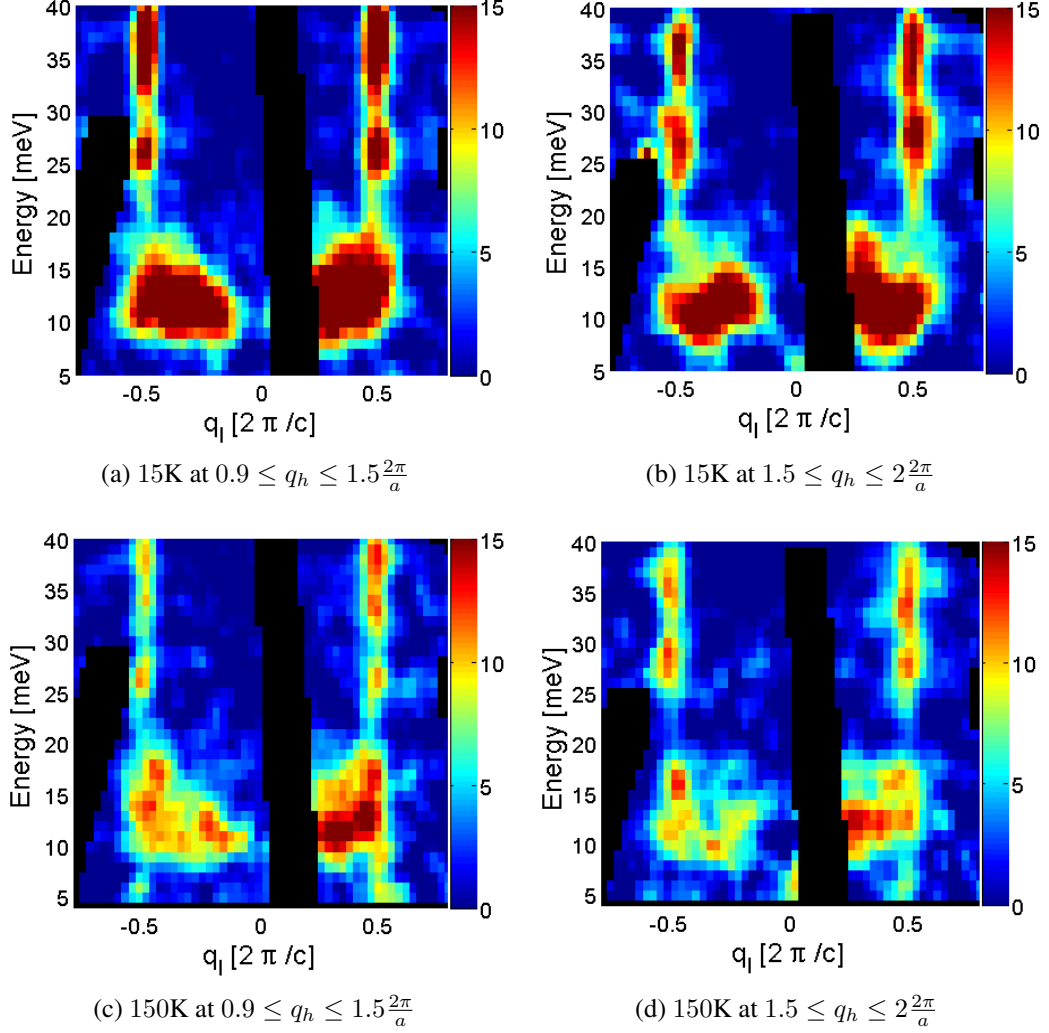
In order to get rid of the chain scattering and to focus on the ladder intensity, the

Figure 7.4.4: Background and chain scattering corrected data for $Sr_{2.5}Ca_{11.5}Cu_{24}O_{41}$ at two different temperatures and two different momenta q_h showing the ladder scattering only.

(a) 15K at $0.9 \leq q_h \leq 1.5\frac{2\pi}{a}$

(b) 15K at $1.5 \leq q_h \leq 2\frac{2\pi}{a}$

(c) 150K at $0.9 \leq q_h \leq 1.5\frac{2\pi}{a}$

(d) 150K at $1.5 \leq q_h \leq 2\frac{2\pi}{a}$

chain scattering was interpolated at each constant energy by a polynomial and subtracted off. The chain corrected result is shown in Fig. 7.4.4. Averaging over data at $0.9 < q_h < 1.5\frac{2\pi}{a}$ the pure ladder intensity now shows the second energy gap around 8meV at 15K (upper left panel) and the closing of this gap at 150K (lower left panel). In the right panels of Fig. 7.4.4 presenting the result at $1.5 < q_h < 2\frac{2\pi}{a}$ the closing of the energy gap at high temperature is found as well. At low temperature a modulation along q_l in the low energy region between $5 - 15$meV appears showing a possible connection
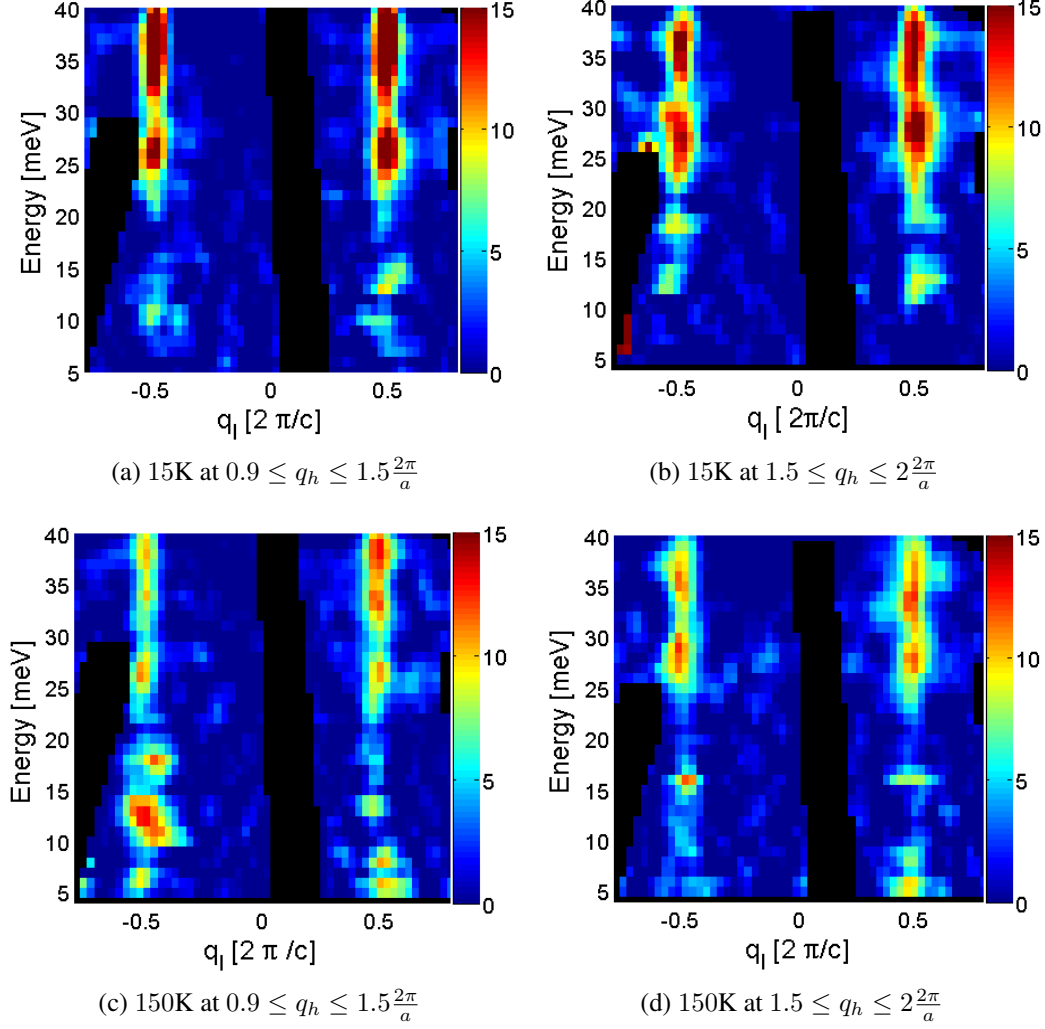
Figure 7.4.5: Background corrected data for $Sr_8Ca_6Cu_{24}O_{41}$ at two different temperatures and two different momenta q_h showing the magnetic ladder and chain scattering only.

(a) 15K at $0.9 \leq q_h \leq 1.5 \frac{2\pi}{a}$

(b) 15K at $1.5 \leq q_h \leq 2 \frac{2\pi}{a}$

(c) 150K at $0.9 \leq q_h \leq 1.5 \frac{2\pi}{a}$

(d) 150K at $1.5 \leq q_h \leq 2 \frac{2\pi}{a}$

between ladder and chain intensities. However, one should notice the change in the intensity scale. Nevertheless, the modulation along q_l is only present at $1.5 < q_h < 2 \frac{2\pi}{a}$.

Next we present the background corrected data of $Sr_8Ca_6Cu_{24}O_{41}$ in Fig. 7.4.5 showing the chain and ladder scattering. The intensity maps show similarities to the one of $Sr_{2.5}Ca_{11.5}Cu_{24}O_{41}$ in Fig 7.4.3. The chains appear as highly intensive drop shaped patches, that change their shape with changing q. The ladders are represented by highly

Figure 7.4.6: Background corrected data for $Sr_8Ca_6Cu_{24}O_{41}$ at two different temperatures and two different q_h showing the ladder only.

(a) 15K at $0.9 \leq q_h \leq 1.5 \frac{2\pi}{a}$

(b) 15K at $1.5 \leq q_h \leq 2 \frac{2\pi}{a}$

(c) 150K at $0.9 \leq q_h \leq 1.5 \frac{2\pi}{a}$

(d) 150K at $1.5 \leq q_h \leq 2 \frac{2\pi}{a}$

intensive stripes around $q_l = \pm 0.5 \frac{2\pi}{c}$ from 30meV upwards. A feature, that seems to be different from $Sr_{2.5}Ca_{11.5}Cu_{24}O_{41}$, is the additional intensity maximum in the energy region of $24 - 29$meV at $q_l = \pm 0.5 \frac{2\pi}{c}$ representing the closing of the ladder gap.

As the ladder scattering lies on top of the chain scattering between $10 - 20$meV, corresponding to the vertical intensity stripe extending downwards, we remove the chain scattering. To this end, the chain scattering is fitted by a polynomial at each constant energy exactly as it has been done for $Sr_{2.5}Ca_{11.5}Cu_{24}O_{41}$ before. The pure ladder signal

of $Sr_8Ca_6Cu_{24}O_{41}$ is given in Fig. 7.4.6. The intensity of the ladder clearly shows the downward shift of the ladder down to about 8meV at 15K (upper panels) and a closing of the ladder gap at 150meV (lower panels).

7.4.2   Cuts along energy

Constant q-cuts along energy allow for comparisons of the spectra and reveal similarities and differences in the magnetic spectra of the three ladders $La_4Sr_{10}Cu_{24}O_{41}$, $Sr_{2.5}Ca_{11.5}Cu_{24}O_{41}$ and $Sr_8Ca_6Cu_{24}O_{41}$. As already mentioned we compare the spectra of the doped ladders $Sr_{2.5}Ca_{11.5}Cu_{24}O_{41}$ and $Sr_8Ca_6Cu_{24}O_{41}$ with the spectrum of $La_4Sr_{10}Cu_{24}O_{41}$, because $La_4Sr_{10}Cu_{24}O_{41}$ shows the magnetic spectrum of the undoped ladder.

Such q-cuts are shown in Figs. 7.4.7 and 7.4.8, where the panels on the left show the results at 15K and those on the right for 150K. Fig. 7.4.7 shows cuts for $0.9 < q_h < 1.5\frac{2\pi}{a}$ and Fig. 7.4.8 for $1.5 < q_h < 2\frac{2\pi}{a}$. The compound presented is indicated in each panel. The full width half maxima (FWHM) of the peaks, that will be presented in the following, are determined by fitting a Gaussian to each peak of the data. The resolution of the spectrometer is not taken into account, because we are only interested in the relative changes of the FWHM compared to the peak of the undoped ladder (see the discussion below). Here the energy gaps are defined as the energy below the maximum of intensity where the scattering strength is half of its maximum value.
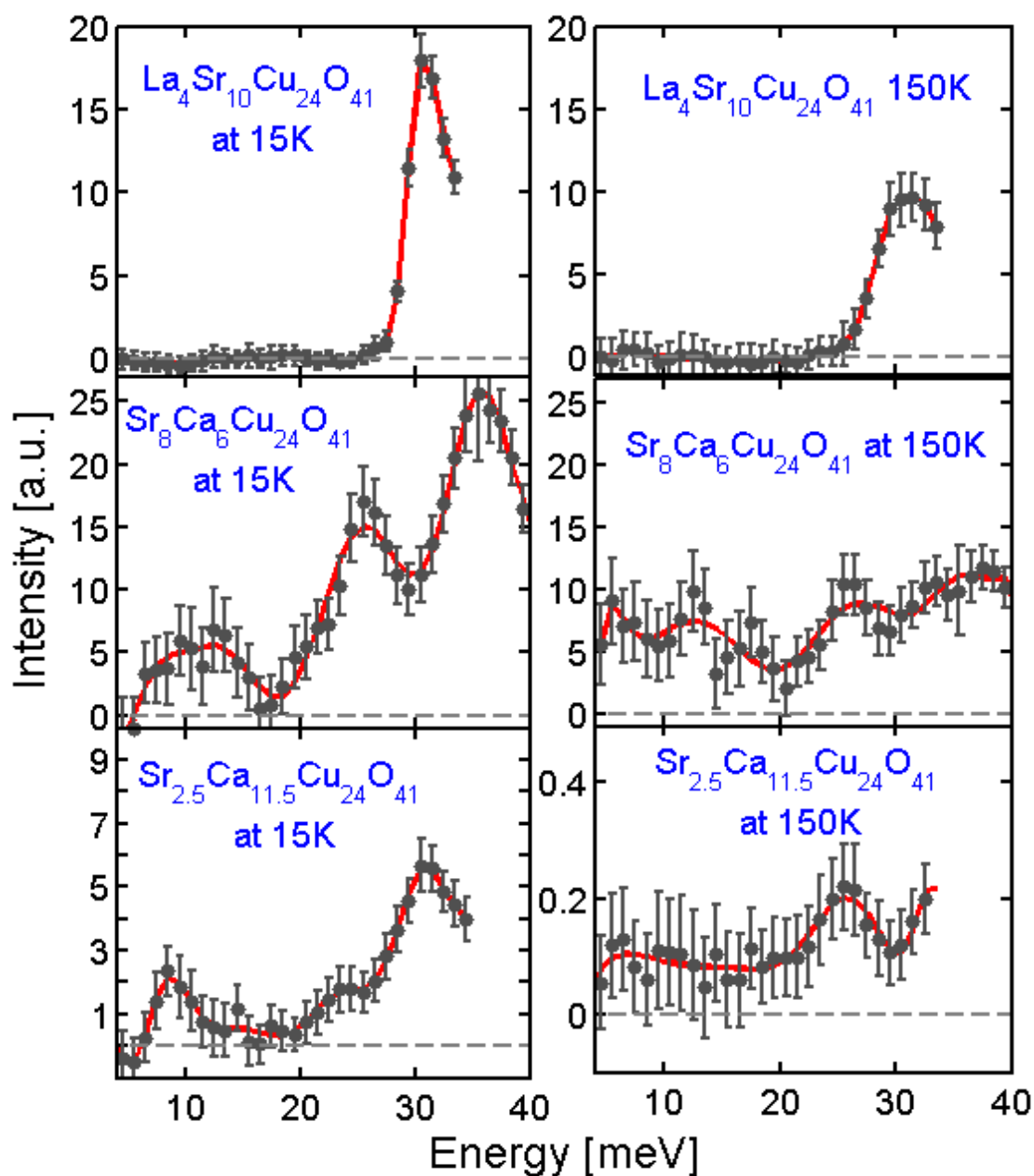
Figure 7.4.7: Constant q-cuts ($0.47 < q_l < 0.48\frac{2\pi}{c}$, $-0.52 < q_l < -0.51\frac{2\pi}{c}$, and $0.9 < q_h < 1.5\frac{2\pi}{a}$) showing the magnetic scattering amplitudes only related to the ladder structure in La$_4$Sr$_{10}$Cu$_{24}$O$_{41}$ (top), Sr$_8$Ca$_6$Cu$_{24}$O$_{41}$ (middle) and Sr$_{2.5}$Ca$_{11.5}$Cu$_{24}$O$_{41}$ (bottom) at 15K (left panels) and 150K (right panels). These cuts are taken along energy from the left panels of Figs. 7.4.1, 7.4.4 and 7.4.6.
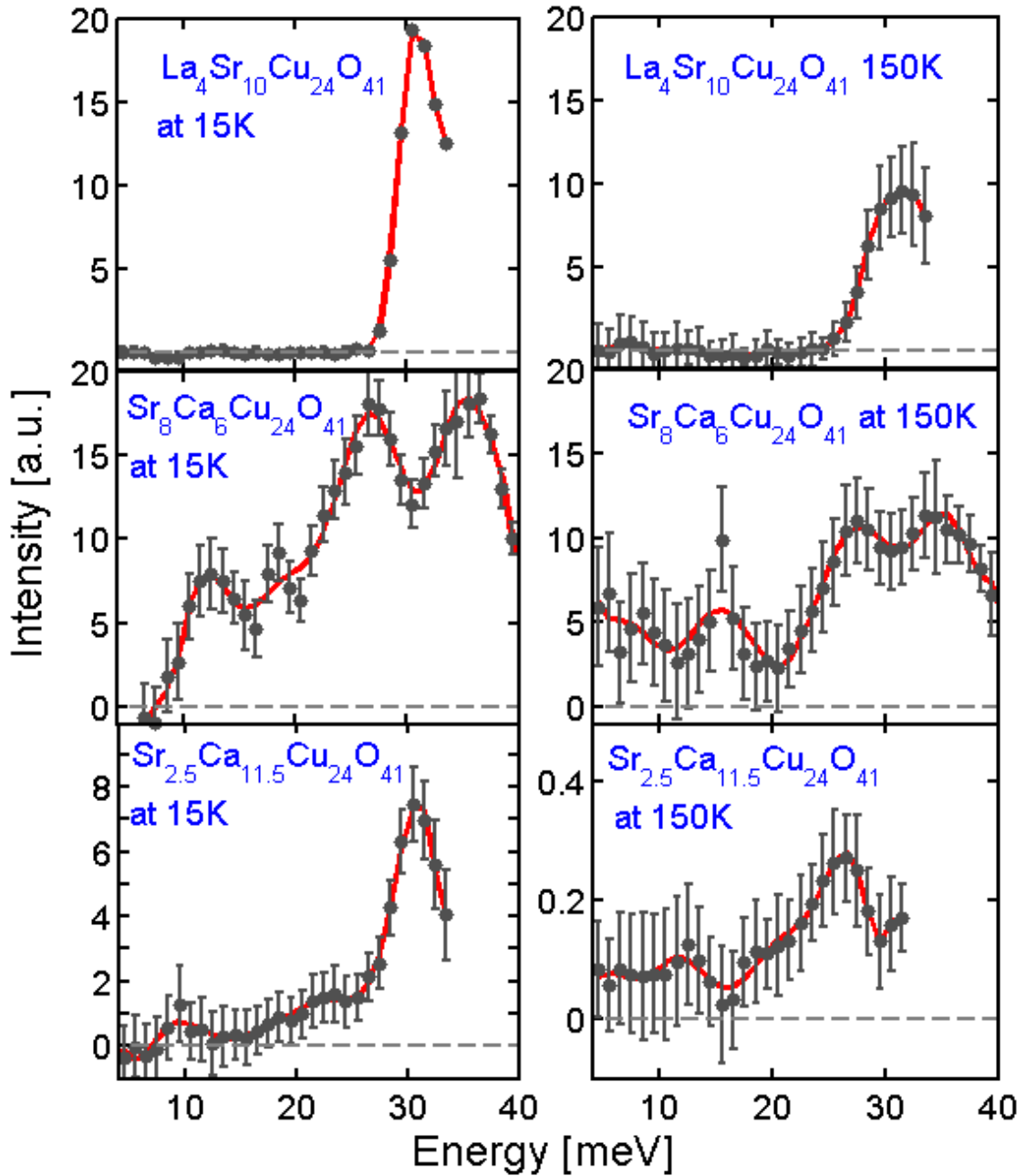
Figure 7.4.8: Constant q-cuts ($0.47 < q_l < 0.48$, $-0.52 < q_l < -0.51$, and $1.5 < q_h < 2\frac{2\pi}{a}$) showing the magnetic scattering amplitudes only related to the ladder structure in La$_4$Sr$_{10}$Cu$_{24}$O$_{41}$ (top), Sr$_8$Ca$_6$Cu$_{24}$O$_{41}$ (middle) and Sr$_{2.5}$Ca$_{11.5}$Cu$_{24}$O$_{41}$ (bottom) at 15K (left panels) and 150K (right panels). These cuts are taken along energy from the right panels of Figs. 7.4.1, 7.4.4 and 7.4.6.

7.4.3 $\mathbf{La_4Sr_{10}Cu_{24}O_{41}}$

The upper panels of Figs 7.4.7 and 7.4.8 present the spectrum of $La_4Sr_{10}Cu_{24}O_{41}$, where the chain response has been removed from the spectrum. Since $La_4Sr_{10}Cu_{24}O_{41}$ has no holes on the ladder, the peak with its maximum at 30.8meV represents the triplon excitation (see discussion). We find the energy gap of the triplon excitation to be $\Delta_T = (29.1 \pm 0.5)$meV with a $FWHM_T$ of 3.3meV at 15K and $\Delta_T = (27.9 \pm 0.5)$meV at 150K with a $FWHM_T$ of 5.8meV. The decrease of the maximum intensity is discussed in Chapter 5.

7.4.4 $\mathbf{Sr_8Ca_6Cu_{24}O_{41}}$

The doped ladder $Sr_8Ca_6Cu_{24}O_{41}$ is presented in the middle panels of Figs. 7.4.7 and 7.4.8. In this case three peaks are present for 15K as well as for 150K. Eye catching is, that the triplon peak at $30 - 40$meV has a higher maximum intensity than the peak at $20 - 30$meV for $0.9 < q_h < 1.5\frac{2\pi}{a}$ at 15K. The peak at $20 - 30$meV is referred to as the *quasiparticle-hole charge* (HC) peak as will be explained in the discussion. The third peak is located at lower energies between $7 - 15$meV and is referred to as the *subgap* (SG) peak and will be also explained in the discussion.

In the data of the undoped ladder $La_4Sr_{10}Cu_{24}O_{41}$ there is only one sharp peak giving one single energy gap. Thus, any additional properties in the spectra of the doped ladders are intrinsically connected with their content of holes.

	Δ_{SG} [meV]	Δ_{HC} [meV]	Δ_T [meV]
$0.9 < q_h < 1.5\frac{2\pi}{a}$ at 15K	7.3 ± 0.5	22.9 ± 0.5	31.7 ± 0.5
$1.5 < q_h < 2\frac{2\pi}{a}$ at 15K	10.4 ± 0.5	23.3 ± 0.5	31.2 ± 0.5
$0.9 < q_h < 1.5\frac{2\pi}{a}$ at 150K	8.3 ± 0.5	22.9 ± 0.5	30.1 ± 0.5
$1.5 < q_h < 2\frac{2\pi}{a}$ at 150K	11.7 ± 0.5	23.3 ± 0.5	30 ± 0.5

Table 7.1: Values of the energy gaps in the spectrum of $Sr_8Ca_6Cu_{24}O_{41}$. The indices are shortcuts for triplon (T), hole-charge (HC) and subgap (SG).

The energy gaps of all peaks are determined by fitting a Gaussian to the data. The results for the energy gaps and their FWHM of the spectrum for $Sr_8Ca_6Cu_{24}O_{41}$ are summarized in Tables 7.1 and 7.2, respectively. The position of the subgap varies a bit

	FWHM$_{\text{SG}}$ [meV]	FWHM$_{\text{HC}}$ [meV]	FWHM$_{\text{T}}$ [meV]
$0.9 < q_h < 1.5\frac{2\pi}{a}$ at 15K	7.5	5.8	8.3
$1.5 < q_h < 2\frac{2\pi}{a}$ at 15K	4.2	7.5	8.3
$0.9 < q_h < 1.5\frac{2\pi}{a}$ at 150K	8.3	5.8	11.7
$1.5 < q_h < 2\frac{2\pi}{a}$ at 150K	6.7	7.5	10

Table 7.2: Values of the FWHM in the spectrum of $Sr_8Ca_6Cu_{24}O_{41}$. The indices are shortcuts for triplon (T), hole-charge (HC) and subgap (SG).

with q_h (compare with Table 7.1), where the position of the charge-hole peaks and the triplon peaks remain nearly constant.

It is clear that the peak with a gap at 30meV originates from the triplon excitation, because it is located at the same energy as the $La_4Sr_{10}Cu_{24}O_{41}$ peak. Due to the broadening of this peak in comparison to the $La_4Sr_{10}Cu_{24}O_{41}$ peak the gap moves to a slightly higher energy. The broadening of the peak traces back to the presence of holes. The holes might collide with the triplons, resulting in a lifetime broadening even at a low temperature of 15K.

7.4.5 $Sr_{2.5}Ca_{11.5}Cu_{24}O_{41}$

If we turn to the doped ladder $Sr_{2.5}Ca_{11.5}Cu_{24}O_{41}$ (bottom panels of Figs. 7.4.7 and 7.4.8), we see again three peaks. The energy gaps and their FWHM are summarized in Tables 7.3 and 7.4, respectively.

	Δ_{SG} [meV]	Δ_{HC} [meV]	Δ_{T} [meV]
$0.9 < q_h < 1.5\frac{2\pi}{a}$ at 15K	6.9 ± 0.5	22.9 ± 0.5	27.9 ± 0.5
$1.5 < q_h < 2\frac{2\pi}{a}$ at 15K	7.9 ± 0.5	23.3 ± 0.5	28.3 ± 0.5
$0.9 < q_h < 1.5\frac{2\pi}{a}$ at 150K	$--$	22.9 ± 0.5	$--$
$1.5 < q_h < 2\frac{2\pi}{a}$ at 150K	$--$	23.3 ± 0.5	$--$

Table 7.3: Values of the energy gaps in the spectrum of $Sr_{2.5}Ca_{11.5}Cu_{24}O_{41}$. The indices are shortcuts for triplon (T), hole-charge (HC) and subgap (SG).

In this case the hole-charge peak between $20 - 30$meV is not that obvious, because firstly it has only one third of the intensity of the triplon peak and secondly it is overlaid

	FWHM$_{SG}$ [meV]	FWHM$_{HC}$ [meV]	FWHM$_T$ [meV]
$0.9 < q_h < 1.5\frac{2\pi}{a}$ at 15K	3.3	5.8	5.8
$1.5 < q_h < 2\frac{2\pi}{a}$ at 15K	3.3	5.8	5
$0.9 < q_h < 1.5\frac{2\pi}{a}$ at 150K	——	5.8	——
$1.5 < q_h < 2\frac{2\pi}{a}$ at 150K	——	5.8	——

Table 7.4: Values of the FWHM in the spectrum of $Sr_{2.5}Ca_{11.5}Cu_{24}O_{41}$. The indices are short-cuts for triplon (T), hole-charge (HC) and subgap (SG).

by the triplon peak. However, it is still visible.

The peak of the subgap state is clearly seen at low energies. The situation at 150K looks different. At $0.9 < q_h < 1.5\frac{2\pi}{a}$ (Fig. 7.4.7) the hole charge peak has clearly survived. In contrast, the triplon excitation has nearly vanished in the energy range captured here. However, it might be possible that it has moved up to higher energies with a surely tremendously decreased scattering amplitude. This possible shifted triplon response cannot be extracted from the data presented here, because the edges of detection are about 35meV. The subgap state peak ($\Delta_{SG} = 7 - 8$meV at 15K) broadens that much, that it results in a constant intensity distribution of one third to one half of the maximum intensity values down to the lowest energy of 4meV.

7.5 Discussion

In the following we propose a possible explanation for the experimental findings described in the preceding section. Similarities with angle resolved photo emission spectroscopy [40, 41] and a further INS study [42] are pointed out.

7.5.1 Undoped ladder - triplon excitation

The formation of the gapped spin liquid state in the undoped ladder is readily understood in terms of the formation of pairs of spin singlets patterned over the lattice - a resonating valence bond type state. Energy is required to break such a singlet and form a triplon - an SU(2) rotational triplet excited state carrying spin $S = 1$. The magnetic dispersion is characterised by an energy gap to the highly dispersive triplon [109].

The energy gap appearing in the undoped ladder is at 29meV which results from such an

excitation of a singlet to a $S = 1$ triplet on a rung during the neutron scattering process. For $La_4Sr_{10}Cu_{24}O_{41}$ the wave vector broadening at $150K$ in comparison to $15K$ traces back to collisions among the triplons, which in turn result in finite lifetimes of the excitations. This effect was described theoretically by Essler et al. [92].

7.5.2   Considerations on hole doping

Doping holes into the ladder is expected to result in the formation of charge-pairs due to the magnetic spin pairing pushing the holes together. The paired holes can then cooperatively form s- or d-wave charge-density-wave (s-CDW or d-CDW), superconducting (SC), or Wiger hole crystal (WHC), states depending on the balance of magnetic and Coulomb interaction strengths. The consensus for the doped cuprates at low doping is that they will either form WHC or superconducting states and that these will compete with each other in an analogous way to how stripes and superconductivity are thought to compete in high-T_c cuprates [10]. Indeed, in the materials $Sr_{14-x}Ca_xCu_{24}O_{41}$ (SCCO) which have hole-doped ladders Raman [114, 115], electrical conductivity [116, 114], and x-ray diffraction measurements [117, 118] have shown that a WHC forms. Further, for Ca substitutions $x = 11 - 13$ superconductivity is observed [119] under pressure.

Whilst the CDW states form at the wavevector $2k_F$, the instability for the formation of the Wigner hole crystal is $4k_F = 2k_F^B + 2k_F^A = (1 - \delta)\frac{\pi}{c}$ [120] where c is the Cu-Cu distance along the legs and k_F^B, k_F^A the bonding and antibonding Fermi wavevectors. The hole concentration δ on the ladders in $Sr_{14-x}Ca_xCu_{24}O_{41}$ (SCCO) for different Ca substitution x has been controversial. Measurements using soft x-ray resonant diffraction (SXRD) [117, 118] have reported Bragg peaks at small wave-vectors along the ladder direction $[0, 0, q_c]$ where $q_c = \frac{2\pi}{3c}$ for the Calcium concentration $x = 11$ and $q_c = \frac{2\pi}{5c}$ for $x = 0$, corresponding to repeat distances along the ladders of $\lambda = 3$ and $\lambda = 5$ respectively for the charge modulation. While these distances were interpreted as hole concentrations of $\delta = \frac{1}{3}$ and $\delta = \frac{1}{5}$ (using the $4k_F$ relation above), any staggering of the order between ladders was ignored in the analysis. In fact holes on neighbouring ladders in close proximity are expected to repel each other due to an electrostatic repulsion of order 0.2eV [121]. This should result in staggered ordering on neighbouring ladders as shown in Fig. 7.5.1. For a simple on-axis Bragg peak, such as the $[0, 0, L]$ observed by Abbamonte and coworkers [117], the staggering will result in modified relationships
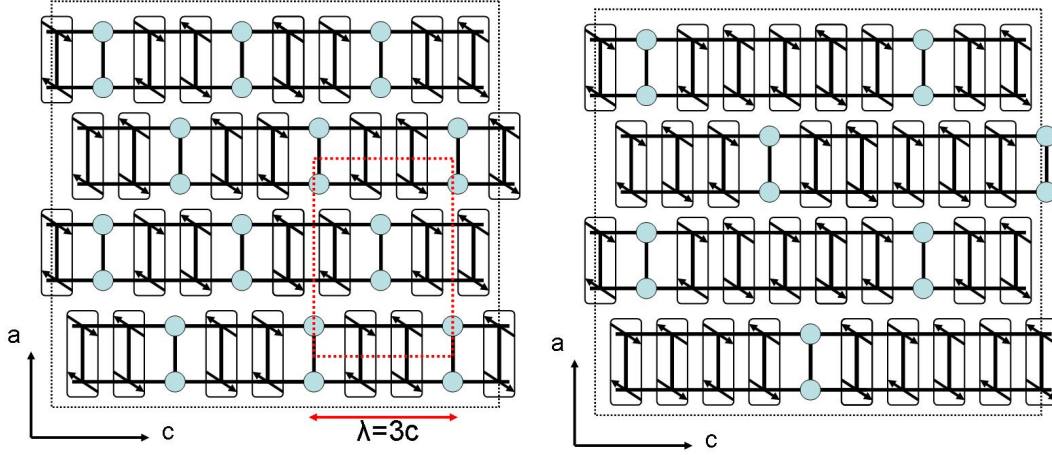
Figure 7.5.1: Staggered ordering on different ladders (taken from Ref. [10]): The Bragg peak $[0, 0, \frac{1}{3}]$ is in absence for this structure (left panel). The hole patterning shown would produce a clear Bragg peak at $[0, 0, \frac{1}{3}]$ but has a filling of $\frac{1}{6}$ rather than $\frac{1}{3}$ (right panel).

$\delta = \frac{L}{Z}$ where $Z = 1, 2, 3, ...$ Due to the short wavevector 0.47Å^{-1} for the $CuL_{\frac{3}{2}}$ edge SXRD reaches only a very limited region of reciprocal space and so variations in the hole ordering could in fact result in the inability of SXRD to observe Bragg peaks despite a Wigner hole crystal forming (e.g. causing off-axis Bragg peaks). Indeed, other techniques indicate Wigner hole ordering for all x in apparent contradiction to quantum hole melting claimed on the basis of the SXRD showing disappearance of on-axis Bragg peaks.

ARPES[1] measurements give an indication of antibonding and bonding Fermi wavevectors, k_F^A and k_F^B in the ladder plane. In the case of coupled gapped ladders the hole density can be estimated from the putative Fermi surface using Luttingers theorem [124]. Whilst Koitzsch et al. obtain a hole content on the ladders of between 0.15 and 0.2 for SCCO with $x = 11.5$, their analysis depends on a large shifting of the bonding and antibonding bands between $x = 0$ and $x = 11.5$. A re-evaluation of this approximation by Tennant [10] estimated a lower number of holes of 0.02 hole doping per ladder copper. Nücker [125] has estimated the number of holes to be 0.08 per ladder Cu which would match with $Z = 4$.

---

[1]Angle resolved photo-emission spectroscopy (ARPES) measures in principal the dispersion upon removing an electron (equally to injecting a hole) [122, 123], allowing for a direct study of the momentum dependence of electronic properties [6]. Therefore, in the case of the doped ladder ARPES measures a large Fermi surface although the material is an insulator [123].

7.5.3   Doped ladders - triplon and subgap states

The most interesting new feature presented in this work is the appearance of a new mode extending well below the triplon gap of 29meV, down to 8meV, the "subgap" scattering. The subgap states are weak in intensity and are directly linked to the presence of holes. They are observed to appear in both of the doped samples studied, $Sr_{2.5}Ca_{11.5}Cu_{24}O_{41}$ and $Sr_8Ca_6Cu_{24}O_{41}$.

The subgap states are similar in both cases, with wave-vector broadened intensity extending below the damped triplons to an energy gap of 8meV. The triplons in the doped ladders are, however, no longer resolution limited as in the undoped ladder but show lifetime broadening, which traces back to collisions of triplons and holes. In the case of $Sr_8Ca_6Cu_{24}O_{41}$ the triplon peak is split into two peaks.

On heating to above the charge ordering temperature of about 60K for $Sr_{2.5}Ca_{11.5}Cu_{24}O_{41}$, the subgap states collapse and the spectrum becomes gapless. In addition intensity is rapidly lost from the triplon mode at 30meV. This is much more distinct than for the undoped ladder where changes only occur on the temperature scale of the gap of about 300K (see Capter 5). The same collapse in spectrum is evident in the $Sr_8Ca_6Cu_{24}O_{41}$ measurements on heating to 150K.

To understand more about the behaviour of the magnetic dynamics and nature of the excitations we consider the dynamics of the electronic degrees of freedom and quasi-particles. The electronic quasiparticles form two "bands", an antibonding band (A) and a bonding band (B). These have been observed in $Sr_{14}Cu_{24}O_{41}$ and $Sr_{2.5}Ca_{11.5}Cu_{24}O_{41}$ using angle resolved photoemission spectroscopy (ARPES) by Yoshida et al. [40] and Koitzsch et al. [41]. The quasiparticle hole-charge dispersions show an energy gap in SCCO for $x = 0$ of $\Delta_{HC} \sim 70$meV and $\Delta_{HC} \sim 12$meV for $x = 11$ [40] as expected for the charge ordering. LDA band structure calculations for the Cu_2O_3 planes have been undertaken by Arai [126] (for SCCO with $x = 0$ and $x = 14$) and Müller et al. [127] (for $SrCu_2O_3$) which give similar results and are in "remarkable agreement" [41] with the ARPES spectra.

The appearance of a gap at $\Delta_{SG} \sim 8$meV in the subgap states is consistent with charge pairing occuring in SCCO $x = 6$ and $x = 11.5$ and a singlet magnetic ground state. In addition the quasi-particles are also gapped consistent with a resonating valence bond state with quasiparticle pairing proposed by Rice and collaborators [123]. It is interest-

ing to this end to note that the quasiparticle-hole charge gap, $2\Delta_{HC} \sim 24\text{meV}$ is similar to the triplon gap $\Delta_T \sim 28\text{meV}$. Quantum field theories [128, 129] predict dynamical symmetry enlargement in doped ladders with small gaps compared to their bandwidths (here we have 30meV compared to 300meV [109]) as applicable here. A key signature of this is that the energy gaps of magnetic and charged dynamics become the same and the similarity of $2\Delta_{HC}$ and Δ_T is therefore noteworthy. The excitations are split into a
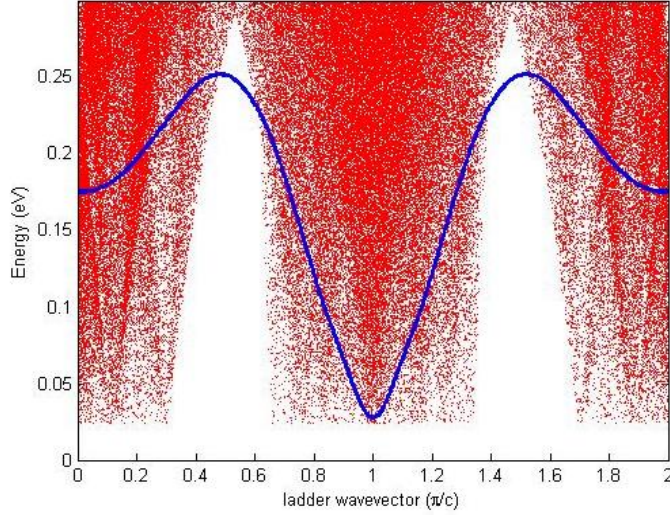

Figure 7.5.2: Quasiparticle-hole spectra for $Sr_{14}Cu_{24}O_{41}$ and $Sr_{2.5}Ca_{11.5}Cu_{24}O_{41}$ overlaid with the one-triplon dispersion ($x = 1.5$ and $x_{cyc} = 0.2$) at low temperature (below the charge ordering temperature of $Sr_{2.5}Ca_{11.5}Cu_{24}O_{41}$).

limited number of (paired) quasi-particles carrying charge e and spin $\frac{1}{2}$, and the triplon mode with $S = 1$ [130]. At half filling (zero doping) the quasi particles disappear and the triplon mode continuously deforms to the undoped dispersion. In Figs. 7.5.2 and 7.5.3 we show the quasiparticle-hole spectra overlaid on the one-triplon mode below and above the charge ordering temperature, respectively. Both spectra overlap and so providing the channel for triplon decay and therefore lifetime broadening down to the lower boundary of the quasiparticle-hole continuum. It has been pointed out by Roux et al. [52] that hole pairs can capture a triplon and form a bound mode as sketched in Fig. 7.5.4, and this may explain the origin of the subgap state. On increasing the temperature above the charge ordering temperature the quasiparticle gap is expected to close and so the quasiparticle-hole continuum extends to zero energy as shown in Fig. 7.5.3. The observed collapse of the subgap states to gapless and the sudden loss of
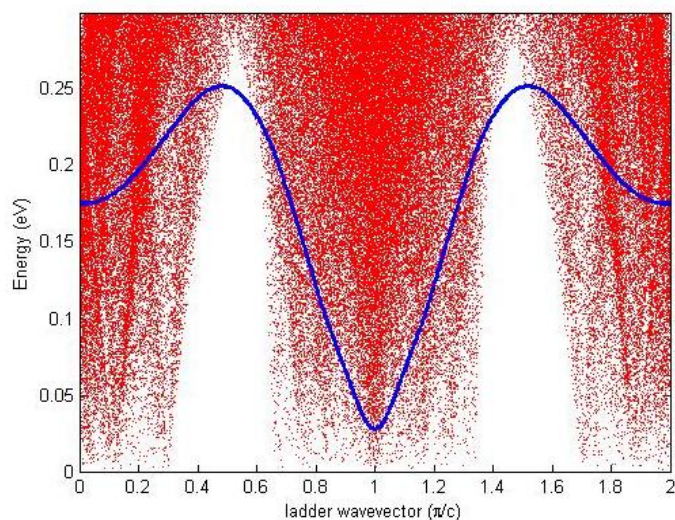
Figure 7.5.3: Quasiparticle-hole spectra for $Sr_{14}Cu_{24}O_{41}$ and $Sr_{2.5}Ca_{11.5}Cu_{24}O_{41}$ over-laid with the one-triplon dispersion ($x = 1.5$ and $x_{cyc} = 0.2$) at high temperature (above the charge ordering temperature of $Sr_{2.5}Ca_{11.5}Cu_{24}O_{41}$).
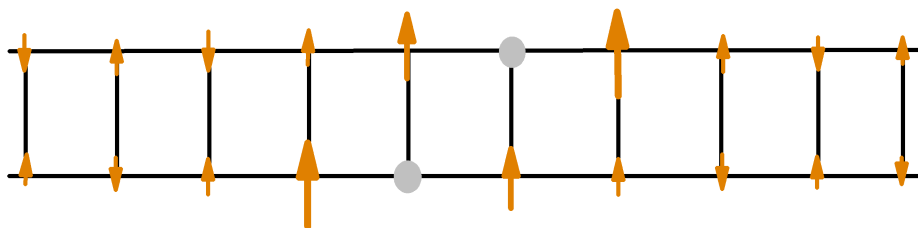

Figure 7.5.4: Hole pair captured by triplons. Holes are indicated by the solid grey circles and the spins $\frac{1}{2}$ by the orange arrows.

intensity of the triplons as they decay more strongly in both x=6 and x=11.5 SCCO is entirely consistent with this (compare with Figs. 7.4.7 and 7.4.8). Indeed, recent INS measurements on x=0 [42] also show decay and melting behaviour that is consistent with the interpretation here. An interesting point is that the triplon gap in x=6 (and x=0 [42]) is split. A possible explanation for this is that the Coulombic energy at low doping favours the formation of charge rich and charge poor ladders as shown in Fig. 7.5.3. The gaps would then be from the two different effective dopings in the system. Further high resolution soft x-ray and ARPES measurements would be useful in these cases.
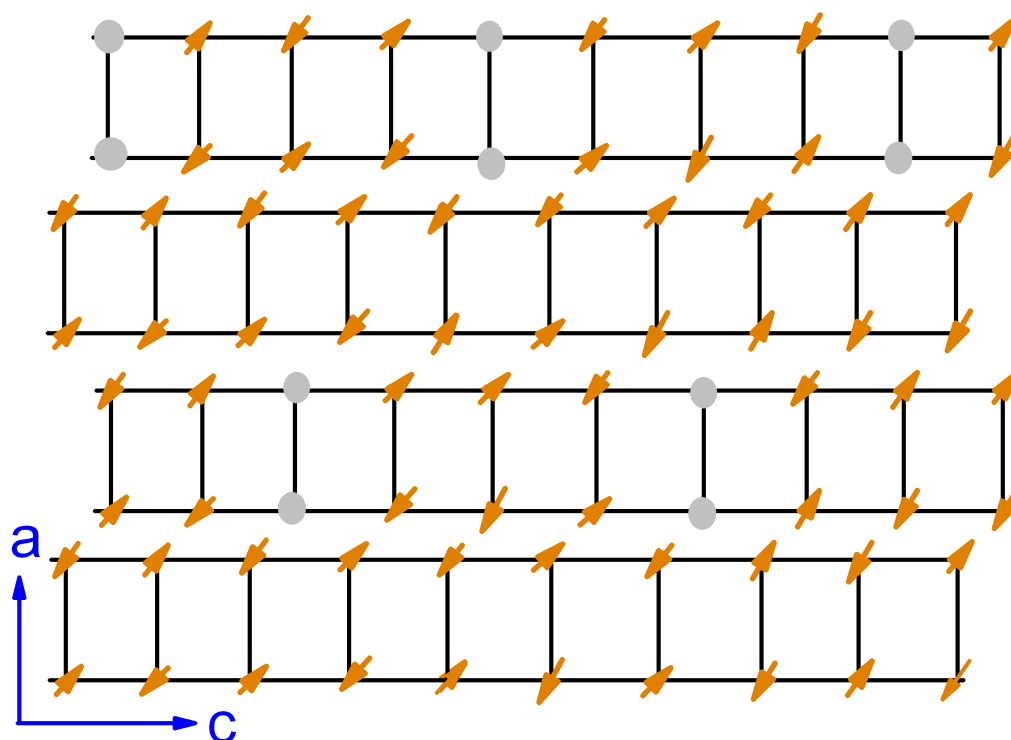
Figure 7.5.5: Formation of charge (hole) rich and charge (hole) poor ladders at low doping induced by Coulombic interaction: Charges (holes) are indicated by the solid grey circles. The antiferromagnetically coupled spins $\frac{1}{2}$ are indicated by the orange arrows.

7.6 Conclusions

We measured the magnetic spectra of the doped cuprate spin-$\frac{1}{2}$ ladders $Sr_{2.5}Ca_{11.5}Cu_{24}O_{41}$ and $Sr_8Ca_6Cu_{24}O_{41}$ and compared them with the spectrum of the undoped ladder $La_4Sr_{10}Cu_{24}O_{41}$ for temperatures below and above the charge ordering temperature of about 60K for $Sr_{2.5}Ca_{11.5}Cu_{24}O_{41}$.

The undoped ladder $La_4Sr_{10}Cu_{24}O_{41}$ is characterized by a gap between spin and charge spectrum. Its triplon (spin) gap is located at $29-30$meV and 28meV at 15K and 150K respectively. The triplon gaps in the doped ladders $Sr_{2.5}Ca_{11.5}Cu_{24}O_{41}$ and $Sr_8Ca_6Cu_{24}O_{41}$ are determined to be 28meV and 31.5meV respectively and 23meV at a temperature of 15K. At a temperature of 150K only for $Sr_8Ca_6Cu_{24}O_{41}$ the triplon gap could be determined to lie a little lower at 30meV.

While the triplons in the undoped ladder are resolution limited [109], the triplons in the doped cases are damped out due to possible collisions of holes and triplons. Additionally the triplon peak in $Sr_8Ca_6Cu_{24}O_{41}$ is split into two peaks with the gap of the second peak at $23meV$. This is in remarkably agreement with the quasiparticle hole-charge gap of $2\Delta_{HC} \sim 24meV$ measured by ARPES [40]. A possible explanation for the splitting is that the Coulombic energy at low doping favours the formation of charge rich and charge poor ladders. The gaps would then be from the two different effective dopings in the system. In conclusion, a key signature of the results is that the energy gaps of magnetic and charged dynamics become the same.

We could identify subgap states extending well below the triplon excitation down to $\sim 8meV$, which is consistent with charge pairing occurring in $Sr_8Ca_6Cu_{24}O_{41}$ and $Sr_{2.5}Ca_{11.5}Cu_{24}O_{41}$ and a singlet magnetic ground state. On heating to above the charge ordering temperature these subgap states collapse resulting in gapless spectra for both doped ladders. In addition the triplon mode decreases in intensity stronger than for the undoped ladder.

Chapter 8

Conclusion and outlook

This thesis contributes to three current issues related to the theoretical and experimental study of the antiferromagnetic spin-$\frac{1}{2}$ ladder. First, a theory at finite temperature for the isolated ladder is developed and experimentally validated. Next, the influence of a neighboring ladder is incorporated gaining information on zero temperature quantum fluctuations. These findings are compared both with further theoretical and with experimental results. Finally, the effect of doping holes into the ladder is measured and the gained data are evaluated. The experimental results thus obtained are qualitatively related to theory. In the following the results obtained in each of these three areas are summed up and interpreted. In addition, in each of these cases, further investigations are proposed.

In this thesis, a theory at finite temperature for the antiferromagnetic spin-$\frac{1}{2}$ ladder has been developed and experimentally validated. Such an antiferromagnetic spin-$\frac{1}{2}$ ladder is realized by the cuprate $La_4Sr_{10}Cu_{24}O_{41}$. The derivation of the model is based on the effective one-triplon dispersion as determined by the PCUT method by Uhrig, Knetter and Schmidt [29, 28, 90, 65]. By a mean field approach the hardcore property of the magnetic excitations is partially incorporated in the model. In this setting the contribution of the conditional excitation due to thermal fluctuations to the one-triplon spectral weight at finite temperature is deduced. It can be incorporated in the theoretical description by vertex corrections. Finally, quantities such as, e.g., the dynamical structure factor are derived from the correspondingly modified spectral weight.

On the theoretical side it could be shown that the modified one-triplon spectral weight including the effect of conditional excitations diminishes for a single ladder with increasing temperature affecting the dynamical structure factor in the expected way.

We compared the calculated spectral weight quantitatively with measured data for the undoped ladder $La_4Sr_{10}Cu_{24}O_{41}$ using inelastic neutron scattering up to temperatures of 150K. This is equivalent to half the spin gap energy. Both theory and experiment exhibit only a weak overall intensity decrease below 150K, but at 150K a significant decrease of about 25% occurs. Within the experimental and theoretical error very good agreement between theory and experiment is found. The effective mean field one-triplon spectral weight is presented for various values $x = \frac{J_\parallel}{J_\perp}$ and $x_{\mathrm{cyc}} = \frac{J_{\mathrm{cyc}}}{J_\perp}$ showing that the best agreement between data and theory at a finite temperature is given for the coupling parameters determined previously from INS data for the dispersion in Ref. [1].

Measurements at temperatures above 150K remain for future work. They will provide further tests for the validity of the developed theory at finite temperature. Further research, both theoretical and experimental, on vertex corrections for other low-dimensional quantum antiferromagnets is eligible, such as for the doped spin ladder $Sr_{2.5}Ca_{11.5}Cu_{24}O_{41}$, where the effect of hole doping on the one-triplon dispersion has to be included. In particular, a challenging project consists in the combination of approaches studying the combined effect of line broadening of the single modes [93, 92, 94] and of the vertex corrections.

While this combined PCUT-mean field approach was applied to the isolated ladder first, it has also been transferred into the case of coupled ladders in a second step. Again preceding computations due to Uhrig and Schmidt [3, 2, 4] have been extended by the partial consideration of the hardcore feature on the mean field level. This has been done for the square lattice as well as for the trellis lattice, which represents the relevant geometry for the copper oxide $La_4Sr_{10}Cu_{24}O_{41}$ studied in this work.

For the square lattice we find that the quantum fluctuations at zero temperature only have a small influence on the critical inter-ladder coupling strength defining the closure of the spin gap. Using the mean field approach the critical inter-ladder coupling is enlarged by only $3 - 4\%$. Thus, we conclude that incorporating quantum fluctuation does not reveal new physical insight for the square lattice.

In the case of the trellis lattice the same approach was applied considering the different

lattice geometry. On the mean field level we find that the spin gap diminishes as a function of inter-ladder coupling x_{inter}, which agrees with the findings in Ref. [4]. For the closure of the gap we find critical inter-ladder couplings enlarged up to 21%.

Extending this approach to finite temperature, we find that the influence of quantum fluctuations diminishes for both lattices. In general, for the same range of values x_{inter} we find that the variability of the corresponding values for the mean field singlet occupation number is larger in case of the square lattice than in the trellis lattice situation. However, the scale for the inter-ladder coupling x_{inter} is larger for the trellis lattice than for the square lattice. At high temperature the result for the isolated ladder is obtained, i.e., for $x_{\text{inter}} = 0$.

Finally at a temperature of 15K and 150K respectively a ferromagnetic inter-ladder coupling of h$J_{\text{inter}} = (-23 \pm 6)$meV and h$J_{\text{inter}} = (-36 \pm 6)$meV respectively could be determined from INS data of $La_4Sr_{10}Cu_{24}O_{41}$ for $x = 1.5$ and $x_{\text{cyc}} = 0.2$ in the way proposed in Ref. [4]. However, hthe error of the interladder coupling x_{inter} is of the order of up to 25%, thus it can only give an indication of the order of the "real" inter-ladder coupling strength.

From the convincing agreement between theory and experiment for the temperature evolution of the isolated ladder one can further conclude that the coupling between neighboring ladders is of lower order, because it has not been incorporated in the temperature theory discussed in the beginning of the conclusions. However, a shift of the energy gap in momentum space as exhibited in the case of the trellis lattice is not captured by the temperature theory. To validate the significance of this effect, however, the inter-ladder coupling has to be considered. Further, depending on the level of precision, on which the theory shall be validated, the inter-ladder coupling may become important. Combining the two-dimensional inter-ladder coupling with the temperature theory for the isolated ladder remains for future works. In the case of improved experimental resolution this approach might be important to capture the physics sufficiently accurately.

Realizations of hole-doped antiferromagnetic spin-$\frac{1}{2}$ ladders can be obtained by substitution of Sr^{2+} by Ca^{2+} as has been done, e.g., in the compounds $Sr_{2.5}Ca_{11.5}Cu_{24}O_{41}$ and $Sr_8Ca_6Cu_{24}O_{41}$. For these compounds INS experiments have been carried out. While for the $Sr_{2.5}Ca_{11.5}Cu_{24}O_{41}$ sample a doping of $\delta = 0.06$ has been measured, the $Sr_8Ca_6Cu_{24}O_{41}$ sample exhibited a doping of $\delta = 0.03$. For these two compounds the

influence of holes in the ladder on magnetic excitation spectra has been experimentally studied with INS. The results have been compared with the findings for the spectrum of the undoped ladder $La_4Sr_{10}Cu_{24}O_{41}$.

While in the spectrum of the undoped ladder $La_4Sr_{10}Cu_{24}O_{41}$ only one peak located at an energy of about $29 - 30$meV can be found, three of them arise in the doped ladders of $Sr_{2.5}Ca_{11.5}Cu_{24}O_{41}$ and $Sr_{2.5}Ca_{11.5}Cu_{24}O_{41}$ at the same momentum. The two additional peaks are situated at lower energies than the first one. The corresponding energy amounts in each case approximately to 23meV and to 8meV. Thus they are referred to as the subgap states. The latter subgap state was already reported by Notbohm [1]. Comparison with the spectrum of the undoped ladder as a reference reveals that the peak at about $29 - 30$meV common to all samples traces back to triplon excitations of the ladder. The corresponding features have been discussed above. Comparison with the undoped ladder $La_4Sr_{10}Cu_{24}O_{41}$ suggests that the additional peaks are a consequence of the presence of holes. In the doped ladders an addtional peak broadening is measured and explained by lifetime effects due to collision of holes and triplons. This is qualitatively supported by the so called resonant valence bond (RVB) theory as well as by the stripe ordering theory. While the peak close to the triplon peak can be explained by a hole-pair captured by triplons, the low-energy peak is found to be consistent with charge pairing and a singlet magnetic ground state. Above the charge ordering temperature of $Sr_{2.5}Ca_{11.5}Cu_{24}O_{41}$ the subgap states collapse and the spectra become gapless with an additional intensity loss in the triplon peak.

However, to gain a more detailed picture about the interactions of magnetic excitations and holes more experiments at different doping levels are required. Finally, the significance of an extension of the theory at finite temperature to doped ladders such as $Sr_{2.5}Ca_{11.5}Cu_{24}O_{41}$ or $Sr_8Ca_6Cu_{24}O_{41}$ has already been mentioned before. Such a theory, describing quantitatively the relevant interactions of holes and triplons and maybe even of phonons might also be able to contribute to the understanding of high-temperature superconducting phenomena that arise for certain members of the cuprate family under suitable conditions.

Bibliography

[1] S. Notbohm. *Spin Dynamics of Quantum Spin-Ladders and Chains*. PhD thesis, University of St Andrews, 2007.

[2] G. S. Uhrig, K. P. Schmidt, and M. Grüninger. Magnetic excitations in bilayer high-temperature superconductors with stripe correlations. *J. Phys. Soc. Jpn.*, 74(Suppl.):86, 2005.

[3] G. S. Uhrig, K. P. Schmidt, and M. Grüninger. Unifying magnons and triplons in stripe-ordered cuprate superconductors. *Phys. Rev. Lett.*, 93:267003, 2004.

[4] K. P. Schmidt and G. S. Uhrig. Two dimensionality of magnetic excitations on the trellis lattice: $(La,Sr,Ca)_{14}Cu_{24}O_{41}$ and $SrCu_2O_3$. *Phys. Rev. B*, 75:224414, 2007.

[5] http://nobelprize.org.

[6] K. M. Shen and J. C. S. Davis. Cuprate high temperature superconductors. *Materials today*, 11(9):14–21, 2009.

[7] J. G. Bednorz and K. A. Müller. Possible high T_c superconductivity in the Ba-La-Cu-O system. *Z. Phys. B*, 64:189, 1986.

[8] M. A. Kastner, R. J. Birgeneau, G. Shirane, and Y. Endoh. Magnetic, transport, and optical properties of monolayer copper oxides. *Rev. Mod. Phys.*, 70(3):897–928, Jul 1998.

[9] T. Vuletić, B. Korin-Hamzić, T. Ivek, S. Tomić, B. Gorshunov, M. Dressel, and J. Akimitsu. The spin-ladder and spin-chain system $(la,y,sr,ca)_{14}cu_{24}o_{41}$: Electronic phases, charge and spin dynamics. *Phys. Rep.*, 428:169, 2006.

[10] D. A. Tennant. Private communications, 2007–2010.

[11] E. Dagotto and T. M. Rice. Surprises on the way from one- to two-dimensional quantum magnets: the ladder materials. *Science*, 271:618, 1996.

[12] P. W. Anderson, G. Baskaran, Z. Zou, and T. Hsu. Resonating–valence-bond theory of phase transitions and superconductivity in La_2CuO_4-based compounds. *Phys. Rev. Lett.*, 58(26):2790–2793, Jun 1987.

[13] C. Weber, K. Haule, and G. Kotliar. Optical weights and waterfalls in doped charge-transfer insulators: A local density approximation and dynamical mean-field theory study of $La_{2-x}Sr_xCuO_4$. *Phys. Rev. B*, 78(13):134519, Oct 2008.

[14] S. A. Kivelson, I. P. Bindloss, E. Fradkin, V. Oganesyan, J. M. Tranquada, A. Kapitulnik, and C. Howald. How to detect fluctuating stripes in the high-temperature superconductors. *Rev. Mod. Phys.*, 75(4):1201–1241, Oct 2003.

[15] A. Luther and V. J. Emery. Backward scattering in the one-dimensional electron gas. *Phys. Rev. Lett.*, 33(10):589–592, Sep 1974.

[16] J. Voit. Spectral properties of luther - emery systems. *J. Phys.: Condens. Matter*, 8(50):779–785, Dez 1996.

[17] M. Vojta and T. Ulbricht. Magnetic excitations in a bond-centered stripe phase: Spin waves far from the semiclassical limit. *Phys. Rev. Lett.*, 93:127002, 2004.

[18] H. Tranquada, J. M.and Woo, T. G. Perring, H. Goka, G. D. Gu, G. Xu, M. Fujita, and Yamada K. Quantum magnetic excitations from stripes in copper oxide superconductors. *Nature*, 429:534–538, June 2004.

[19] M. S. Windt. *Optical Spectroscopy of Spin Ladders*. PhD thesis, Universität zu Köln, Cologne, Germany, 2002.

[20] P. W. Anderson. Antiferromagnetism. Theory of superexchange interaction. *Phys. Rev.*, 79(2):350–356, Jul 1950.

[21] J. B. Goodenough. Theory of the role of covalence in the perovskite-type manganites [La, M(II)]MnO_3. *Phys. Rev.*, 100(2):564–573, Oct 1955.

[22] N. Nücker, M. Merz, C. A. Kuntscher, S. Gerhold, S. Schuppler, R. Neudert, M. S. Golden, J. Fink, D. Schild, S. Stadler, V. Chakarian, J. Freeland, Y. U. Idzerda, K. Conder, M. Uehara, T. Nagata, J. Goto, J. Akimitsu, N. Motoyama, H. Eisaki, S. Uchida, U. Ammerahl, and A. Revcolevschi. Hole distribution in $(Sr,Ca,Y,La)_{14}Cu_{24}O_{41}$ ladder compounds studied by x-ray absorption spectroscopy. *Phys. Rev. B*, 62(21):14384–14392, Dec 2000.

[23] R. S. Eccleston, M. Uehara, J. Akimitsu, H. Eisaki, N. Motoyama, and S. Uchida. Spin dynamics of the spin-ladder dimer-chain material $Sr_{14}Cu_{24}O_{41}$. *Phys. Rev. Lett.*, 81(8):1702–1705, Aug 1998.

[24] Y. Mizuno, T. Tohyama, and S. Maekawa. Electronic states of doped spin ladder $(Sr,Ca)_{14}Cu_{24}O_{41}$. *J. Phys. Soc. Jpn.*, 66(4):937–940, 1997.

[25] C. Hess, C. Baumann, U. Ammerahl, B. Büchner, F. Heidrich-Meisner, W. Brenig, and A. Revcolevschi. Magnon heat transport in $(sr,ca,la)_{14}cu_{24}o_{41}$. *Phys. Rev. B*, 64:184305, 2001.

[26] T. Osafune, N. Motoyama, H. Eisaki, and S. Uchida. Optical study of the $Sr_{14-x}Ca_xCu_{24}O_{41}$ system: Evidence for hole-doped Cu_2O_3 ladders. *Phys. Rev. Lett.*, 78(10):1980–1983, Mar 1997.

[27] T. Nagata, M. Uehara, J. Goto, J. Akimitsu, N. Motoyama, H. Eisaki, S. Uchida, H. Takahashi, T. Nakanishi, and N. Môri. Pressure-induced dimensional crossover and superconductivity in the hole-doped two-leg ladder compound $Sr_{14-x}Ca_xCu_{24}O_{41}$. *Phys. Rev. Lett.*, 81(5):1090–1093, Aug 1998.

[28] C. Knetter, K. P. Schmidt, and G. S. Uhrig. The structure of operators in effective particle-conserving models. *J. Phys. A: Math. Gen.*, 36:7889, 2003.

[29] C. Knetter, K. P. Schmidt, and G. S. Uhrig. High order perturbation theory for spectral densities of multi-particle excitations: $S = 1/2$ two-leg Heisenberg ladder. *Eur. Phys. J. B*, 36:525, 2003.

[30] A. Reischel. *Derivation of Effective Models using Self-Similar Continous Unitary Transformation in Real Space*. PhD thesis, Universität zu Köln, Cologne, Germany, 2006.

[31] S. Gopalan, T. M. Rice, and M. Sigrist. Spin ladders with spin gaps: A description of a class of cuprates. *Phys. Rev. B*, 49(13):8902–8910, 1993.

[32] S. Sachdev and R. N. Bhatt. Bond-operator representation of quantum spins: Mean-field theory of frustrated quantum Heisenberg antiferromagnets. *Phys. Rev. B*, 41(13):9324–9329, 1990.

[33] G. S. Uhrig and B. Normand. Magnetic properties of $(VO)_2P_2O_7$ from frustrated interchain coupling. *Phys. Rev. B*, 58:R14705, 1998.

[34] C. Knetter and G. S. Uhrig. Perturbation theory by flow equations: dimerized and frustrated $S = 1/2$ chain. *Eur. Phys. J. B*, 13:209, 2000.

[35] E. Dagotto, J. Riera, and D. Scalapino. Superconductivity in ladders and coupled planes. *Phys. Rev. B*, 45(10):5744–5747, Mar 1992.

[36] J. A. Riera and S. D. Dalosto. Effects of interladder couplings in the trellis lattice. *Phys. Rev. B*, 63:144431, 2001.

[37] M. Matsumoto, C. Yasuda, S. Todo, and H. Takayama. Ground-state phase diagram of quantum Heisenberg antiferromagnets on the anisotropic dimerized square lattice. *Phys. Rev. B*, 65(1):014407, Nov 2001.

[38] S. Gopalan, T. M. Rice, and M. Sigrist. Spin ladders with spin gaps: A description of a class of cuprates. *Phys. Rev. B*, 49:8901, 1994.

[39] P. W. Anderson. The resonating valence bond state in La_2CuO_4 and superconductivity. *Science mag.*, 1987.

[40] T. Yoshida, X. J. Zhou, Z. Hussain, Z.-X. Shen, A. Fujimori, H. Eisaki, and S. Uchida. Underlying Fermi surface of $Sr_{14-x}Ca_xCu_{24}O_{41}$ in two-dimensional momentum space observed by angle-resolved photoemission spectroscopy. *Phys. Rev. B*, 80(5):052504, Aug 2009.

[41] A. Koitzsch, D. S. Inosov, H. Shiozawa, V. B. Zabolotnyy, S. V. Borisenko, A. Varykhalov, C. Hess, M. Knupfer, U. Ammerahl, A. Revcolevschi, and B. Büchner. Observation of the Fermi surface, the band structure, and their diffraction replicas of $Sr_{14-x}Ca_xCu_{24}O_{41}$ by angle-resolved photoemission spectroscopy. *Phys. Rev. B*, 81(11):113110, Mar 2010.

[42] J. E. Lorenzo, L. P. Regnault, C. Boullier, N. Martin, A. H. Moudden, S. Vanishri, C. Marin, and A. Revcolevschi. Macroscopic quantum coherence of the spin triplet in the spin-ladder compound $Sr_{14}Cu_{24}O_{41}$. *Phys. Rev. Lett.*, 105(9):097202, Aug 2010.

[43] G. L. Squires. *Introduction to the Theory of thermal Neutron Scattering*. Dover Publications, INC., 1996.

[44] S. W. Lovesey. *Theory of Neutron Scattering from Condensed Matter*. Oxford University Press, 1987.

[45] G. Shirane, S. M. Shapiro, and J. M. Tranquada. *Neutron Scattering with a Triple-Axis Spectrometer*. Cambridge University Press, 2002.

[46] B. Lake. Lecture on neutron scattering, 2008.

[47] Canberra Company. www.canberra.com/literature/936.asp.

[48] U. Ammerahl, G. Dhalenne, A. Revcolevschi, J. Berthon, and H. Moudden. Crystal growth and characterization of the spin-ladder compound $(Sr,Ca)_{14}Cu_{24}O_{41}$. *J. Cryst. Growth*, 193:55–60, 1998.

[49] S. Vanishri, C. Marin, H. L. Bhat, B. Salce, D. Braithwaite, and L. P. Regnault. Crystal growth and characterization of the two-leg spin-ladder compound: $Sr_{14}Cu_{24}O_{41}$ and $Sr_2Ca_{12}Cu_{24}O_{41}$. *J. Cryst. Growth*, 2009.

[50] B. J. Kim, H. Koh, E. Rotenberg, S.-J. Oh, H. Eisaki, N. Motoyama, S. Uchida, T. Tohyama, S. Maekawa, Z.-X. Shen, and C. Kim. Distinct spinon and holon dispersions in photoemission spectral functions from one-dimensional $SrCuO_2$. *Nature Physics*, 2:397 – 401, 2006.

[51] V. A. Kashurnikov and B. V. Svistunov. Exact diagonalization plus renormalization-group theory: Accurate method for a one-dimensional superfluid-insulator-transition study. *Phys. Rev. B*, 53:11776, 1996.

[52] G. Roux, S. R. White, S. Capponi, A. Läuchli, and D. Poilblanc. Doped two-leg ladder with ring exchange: Exact diagonalization and density matrix renormalization group computations. *Phys. Rev. B*, 72:014523, 2005.

[53] S. Daul and R. M. Noack. Dmrg study of ferromagnetism in a one-dimensional hubbard model. *Z. Phys. B*, 103:293, 1997.

[54] F. Schönfeld. *Untersuchung dimerisierter, frustrierter Heisenbergketten mittels DMRG-Methoden, Dissertation Köln*. Cuvillier Verlag, Göttingen, 1999.

[55] A. Klümper, R. Raupach, and F. Schönfeld. Finite temperature dmrg investigation of the spin-peierls transition in cugeo$_3$. *Phys. Rev. B*, 59:3612, 1999.

[56] C. Knetter. Störungstheorie mit Hilfe von Flußgleichungen angewendet auf dimerisierte Spinmodelle, 1999. Diplomarbeit, Universität zu Köln.

[57] F. J. Wegner. Flow equations for Hamiltonians. *Ann. Physik*, 3:77, 1994.

[58] S. D. Głazek and K. G. Wilson. Renormalization of Hamiltonians. *Phys. Rev. D*, 48:5863, 1993.

[59] S. D. Głazek and K. G. Wilson. Perturbative renormalization group for Hamiltonians. *Phys. Rev. D*, 49:4214, 1994.

[60] S. A. Hamerla, S. Duffe, and G. S. Uhrig. Derivation of the $t - J$ model for finite doping. *Phys. Rev. B*, Aug. 2010.

[61] Christian Knetter. *Perturbative continuous unitary transformations: Spectral properties of low dimensional spin systems*. PhD thesis, Universität zu Köln, Cologne, Germany, 2003.

[62] A. Mielke. Flow equations for band-matrices. *Eur. Phys. J. B*, 5:605, 1998.

[63] T. Fischer, S. Duffe, and G. S. Uhrig. Adapted continuous unitary transformation to treat systems with quasi-particles of finite lifetime. *New J. Phys.*, 12:033048, March 2010.

[64] K. P. Schmidt, C. Knetter, and G. S. Uhrig. Novel extrapolation for strong coupling expansions. *Acta Physica Polonica B*, 34:1481, 2003.

[65] K. P. Schmidt and G. S. Uhrig. Spectral properties of magnetic excitations in cuprate two-leg ladder systems. *Mod. Phys. Lett. B*, 19:1179, 2005.

[66] K. P. Schmidt and G. S. Uhrig. Excitations in one-dimensional $S = 1/2$ quantum antiferromagnets. *Phys. Rev. Lett.*, 90:227204, 2003.

[67] H. J. Schmidt and Y. Kuramoto. Four-spin interaction as an effective interaction in high-t_c copper oxides. *Physica*, C167:263, 1990.

[68] Y. Honda, Y. Kuramoto, and T. Watanabe. Effects of cyclic four-spin exchange on the magnetic properties of the CuO_2 plane. *Phys. Rev. B*, 47:11329, 1993.

[69] E. Müller-Hartmann and A. Reischl. Derivation of effective spin models from a three band model for CuO_2-planes. *Eur. Phys. J. B*, 28:173, 2002.

[70] A. Reischl, E. Müller-Hartmann, and G. S. Uhrig. Systematic mapping of the Hubbard model to the generalized t-J model. *Phys. Rev. B*, 70:245124, 2004.

[71] S. Brehmer, H.J. Mikeska, M. Müller, N. Nagaosa, and S. Uchida. Effects of biquadratic exchange on the spectrum of elementary excitations in spin ladders. *Phys. Rev. B*, 60:329, 1999.

[72] Y. Mizuno, T. Tohyama, and S. Maekawa. Magnetic interaction in insulating cuprates. *J. Low Temp. Phys.*, 117:389–393, 1999.

[73] M. Matsuda, K. Katsumata, R. S. Eccleston, S. Brehmer, and H.-J. Mikeska. Magnetic excitations from the $S = 1/2$ two-leg ladders in $La_6Ca_8Cu_{24}O_{41}$. *J. Appl. Phys.*, 87:6271, 2000.

[74] M. Matsuda, K. Katsumata, R. S. Eccleston, S. Brehmer, and H.-J. Mikeska. Magnetic excitations and exchange interactions in the $S = 1/2$ two-leg ladder compound in $La_6Ca_8Cu_{24}O_{41}$. *Phys. Rev. B*, 62:8903, 2000.

[75] A. Gößling, U. Kuhlmann, C. Thomsen A. Löffert, C. Gross, and W. Assmus. Magnetic excitations in $SrCu_2O_3$: A Raman scattering study. *Phys. Rev. B*, 67:052403, 2003.

[76] K. P. Schmidt, C. Knetter, M. Grüninger, and G. S. Uhrig. Charge order induced sharp Raman peak in $Sr_{14}Cu_{24}O_{41}$. *Phys. Rev. Lett.*, 90:167201, 2003.

[77] S. Notbohm, P. Ribeiro, B. Lake, D. A. Tennant, K. P. Schmidt, G. S. Uhrig, C. Hess, R. Klingeler, G. Behr, B. Büchner, M. Reehuis, R. I. Bewley, C. D.

Frost, P. Manuel, and R. S. Eccleston. One- and two-triplon excitations of an ideal spin-ladder. *Phys. Rev. Lett.*, 98:027403, 2007.

[78] A. V. Chubukov. A difference in the properties of one-dimensional antiferromagnets with integer and half-integer spins. *Pis'sma Zh. Eksp. Feor. Fiz.*, 49:108, 1989.

[79] A. V. Chubukov. A difference in the properties of one-dimensional antiferromagnets with integer and half-integer spins. *JETP Lett.*, 49:129, 1989.

[80] S. Sachdev and R. N. Bhatt. Bond-operator representation of quantum spins: Mean-field theory of frustrated quantum Heisenberg antiferromagnets. *Phys. Rev. B*, 41:9323, 1990.

[81] S. Sachdev. Quantum phase transitions of antiferromagnets and the cuprate superconductors. *arXiv:1002.3823v3*, 2010.

[82] T. Barnes, E. Dagotto, J. Riera, and E. S. Swanson. Excitation spectrum of Heisenberg spin ladders. *Phys. Rev. B*, 47:3196, 1993.

[83] M. Greven, R. J. Birgeneau, and U.-J. Wiese. Monte carlo study of correlations in quantum spin ladders. *Phys. Rev. Lett.*, 77:1865, 1996.

[84] D. G. Shelton, A. A. Nersesyan, and A. M. Tsvelik. Antiferromagnetic spin ladders: Crossover between spin $S = 1/2$ and $S = 1$ chains. *Phys. Rev. B*, 53:8521, 1996.

[85] J. Oitmaa, R. R. P. Singh, and Z. Weihong. Quantum spin ladders at $T = 0$ and at high temperatures studied by series expansions. *Phys. Rev. B*, 54:1009, 1996.

[86] O. P. Sushkov and V. N. Kotov. Bound states of magnons in the $S = 1/2$ quantum spin ladder. *Phys. Rev. Lett.*, 81:1941, 1998.

[87] R. Eder. Dynamics of spin ladders. *Phys. Rev. B*, 57:12832, 1998.

[88] C. Jurecka and W. Brenig. Optical absorption of spin ladders. *Phys. Rev. B*, 61:14307, 2000.

[89] S. Trebst, H. Monien, C. J. Hamer, Z. Weihong, and R. R. P. Singh. Strong-coupling expansions for multiparticle excitations: Continuum and bound states. *Phys. Rev. Lett.*, 85:4373, 2000.

[90] C. Knetter, K. P. Schmidt, M. Grüninger, and G. S. Uhrig. Fractional and integer excitations in quantum antiferromagnetic spin $1/2$ ladders. *Phys. Rev. Lett.*, 87:167204, 2001.

[91] K. P. Schmidt, H. Monien, and G. S. Uhrig. Rung-singlet phase of the $S = 1/2$ two-leg spin-ladder with four-spin cyclic exchange. *Phys. Rev. B*, 67:184413, 2003.

[92] F. H. L. Essler and R. M. Konik. Finite-temperature lineshapes in gapped quantum spin chains. *Phys. Rev. B*, 78:100403(R), 2008.

[93] A. J. A. James, F. H. L. Essler, and R. M. Konik. Finite-temperature dynamical structure factor of alternating Heisenberg chains. *Phys. Rev. B*, 78:094411, 2008.

[94] A. J. A. James, W. D. Goetze, and F. H. L. Essler. Finite-temperature dynamical structure factor of the Heisenberg-Ising chain. *Phys. Rev. B*, 79:214408, 2009.

[95] M. Troyer, H. Tsunetsugu, and D. Würtz. Thermodynamics and spin gap of the heisenberg ladder calculated by the look-ahead Lanczos algorithm. *Phys. Rev. B*, 50:13515, 1994.

[96] M. Windt, M. Grüninger, T. Nunner, C. Knetter, K. P. Schmidt, G. S. Uhrig, T. Kopp, A. Freimuth, U. Ammerahl, B. Büchner, and A. Revcolevschi. Observation of two-magnon bound states in the two-leg ladders of $(Ca,La)_{14}Cu_{24}O_{41}$. *Phys. Rev. Lett.*, 87:127002, 2001.

[97] This value corresponds to about 630k for $J = 105.5$mev in order to provide a first quantitative link to experiment. This temperature corresponds to about twice the spin gap found in Ref. [77].

[98] A. Revcolevschi, U. Ammerahl, and G. Dhalenne. Crystal growth of pure and substituted low-dimensionality cuprates $CuGeO_3$, La_2CuO_4, $SrCuO_2$, Sr_2CuO_3 and $Sr_{14}Cu_{24}O_{41}$ by the floating zone and travelling solvent zone methods. *J. Cryst. Growth*, 198:593, 1999.

[99] R. S. Eccleston, M. Azuma, and M. Takano. Neutron-scattering and susceptibility study of spin chains and spin ladders in $(Sr_{0.8}Ca_{0.2})_{14}Cu_{24}O_{41}$. *Phys. Rev. B*, 53:R14721, 1996.

[100] M. Azuma, Z. Hiroi, M. Takano, K. Ishida, and Y. Kitaoka. Observation of a spin gap in $SrCu_2O_3$ comprising spin-$\frac{1}{2}$ quasi-1D two-leg ladders. *Phys. Rev. Lett.*, 73:3463, 1994.

[101] T. S. Nunner, P. Brune, T. Kopp, M. Windt, and M. Grüninger. Cyclic spin exchange in cuprate spin ladders. *Phys. Rev. B*, 66:180404(R), 2002.

[102] Bronstein, Semendjajew, Musiol, and Mühling. *Taschenbuch der Mathematik*. Verlag Harri Deutsch, Frankfurt am Main, 2000.

[103] K. P. Schmidt, A. Gössling, U. Kuhlmann, C. Thomsen, A. Löffert, C. Gross, and W. Assmus. Raman response of magnetic excitations in cuprate ladders and planes. *Phys. Rev. B*, 72:094419, 2005.

[104] I. P. R. Moreira, C. J. Calzado, J.-P. Malrieu, and F. Illas. First-principles periodic calculation of four-body spin terms in high-T_c cuprate superconductors. *Phys. Rev. Lett.*, 97:087003, 2006.

[105] E. Dagotto and T. M. Rice. Surprises on the way from one to two dimensional quantum magnet: the ladder materials. *Science*, 271, Feb 1996.

[106] N. Motoyama, T. Osafune, T. Kakeshita, H. Eisaki, and S. Uchida. Effect of Ca substitution and pressure on the transport and magnetic properties of $Sr_{14}Cu_{24}O_{41}$ with doped two-leg Cu-O ladders. *Phys. Rev. B*, 55(6):R3386–R3389, Feb 1997.

[107] K. Magishi, S. Matsumoto, Y. Kitaoka, K. Ishida, K. Asayama, M. Uehara, T. Nagata, and J. Akimitsu. Spin gap and dynamics in $Sr_{14-x}Ca_xCu_{24}O_{41}$ comprising hole-doped two-leg spin ladders: Cu NMR study on single crystals. *Phys. Rev. B*, 57(18):11533–11544, May 1998.

[108] A. V. Chubukov, D. Pines, and J. Schmalian. The physics of superconductors, conventional and high-T_c superconductors. *Springer*, 1:485–590, 2003.

[109] S. Notbohm. *Spin Dynamics of Quatum Spin-Ladders and Chains*. PhD thesis, University of St Andrews, St Andrews, UK, 2007.

[110] C. Gibson, A. Tennant, B. Lake, M. Reehuis, T. Perring. Scattering experiment undertaken on MAPS at ISIS, Rutherford Appleton Laboratory, UK, Oct 2007.

[111] I. Exius, S. Notbohm, A. Tennant, B. Lake, M. Reehuis, and T. Perring. Scattering experiment undertaken on MAPS at ISIS, Rutherford Appleton Laboratory, UK, June 2008 and Sept 2006.

[112] M. Mihalik, A. Tennant, B. Lake, R. I. Bewley, T. Guidi. Scattering experiment undertaken on MERLIN at ISIS, Rutherford Appleton Laboratory, UK, April 2010.

[113] D. A. Tennant and B. Lake. Private communications, 2007–2010.

[114] G. Blumberg, P. Littlewood, A. Gozar, B. S. Dennis, N. Motoyama, H. Eisaki, and S. Uchida. Sliding density wave in $Sr_{14}Cu_{24}O_{41}$. *Science*, 297:584, 2002.

[115] A. Gozar, G. Blumberg, P. B. Littlewood, B. S. Dennis, N. Motoyama, H. Eisaki, and S. Uchida. Collective density-wave excitations in two-leg $Sr_{14-x}Ca_xCu_{24}O_{41}$ ladders. *Phys. Rev. Lett.*, 91(8):087401, Aug 2003.

[116] B. Gorshunov, P. Haas, T. Rõõm, M. Dressel, T. Vuletic, B. Korin-Hamzic, S. Tomic, J. Akimitsu, and T. Nagata. Charge-density wave formation in $Sr_{14-x}Ca_xCu_{24}O_{41}$. *Phys. Rev. B*, 66:060508, 2002.

[117] P. Abbamonte, G. Blumberg, A. Rusydi, A. Gozar, P. G. Evans, T. Siegrist, L. Venema, H. Eisaki, E. D. Isaacs, and G. A. Sawatzky. Crystallization of charge holes in the spin ladder of $Sr_{14}Cu_{24}O_{41}$. *Nature*, 431:1078, 2004.

[118] A. Rusydi, P. Abbamonte, H. Eisaki, Y. Fujimaki, G. Blumberg, S. Uchida, and G. A. Sawatzky. Quantum melting of the hole crystal in the spin ladder of $Sr_{14-x}Ca_xCu_{24}O_{41}$. *Phys. Rev. Lett.*, 97:016403, 2006.

[119] T. Nagata, M. Uehara, J. Goto, J. Akimitsu, M. Motoyama, H. Eisaki, S. Uchida, H. Takahashi, T. Nakanishi, and N. Môri. Presssure-induced dimensional crossover and superconductivity in the hole-doped two-leg ladder compound $Sr_{0.4}Ca_{13.6}Cu_{24}O_{41.84}$. *Phys. Rev. Lett.*, 81:1090, 1998.

[120] D. Controzzi and A. M. Tsvelik. Excitation spectrum of doped two-leg ladders: A field theory analysis. *Phys. Rev. B*, 72(3):035110, Jul 2005.

[121] K. Wohlfeld, A. M. Oleś, and G. A. Sawatzky. Charge density wave in $Sr_{14-x}Ca_xCu_{24}O_{41}$. *Phys. Stat. Sol. (b)*, 247:668–670, June 2010.

[122] A. V. Chubukov and M. R. Norman. Dispersion anomalies in cuprate supercon-ductors. *Phys. Rev. B*, 70(17):174505, Nov 2004.

[123] T. M. Rice, M. Troyer, and H. Tsunetsugu. The d-wave resonance valence bond state. *J. Phys. CJem. Solids*, 56(12):1663–1667, 1995.

[124] R. M. Konik, T. M. Rice, and A. M. Tsvelik. Doped spin liquid: Luttinger sum rule and low temperature order. *Phys. Rev. Lett.*, 96(8):086407, Mar 2006.

[125] N. Nücker, M. Merz, C. A. Kuntscher, S. Gerhold, S. Schuppler, R. Neudert, M. S. Golden, J. Fink, D. Schild, S. Stadler, V. Chakarian, J. Freeland, Y. U. Idzerda, K. Conder, M. Uehara, T. Nagata, J. Goto, J. Akimitsu, N. Motoyama, H. Eisaki, S. Uchida, U. Ammerahl, and A. Revcolevschi. Hole distribution in $(Sr,Ca,Y,La)_{14}Cu_{24}O_{41}$. *Phys. Rev. B*, 62:14384, 2000.

[126] M. Arai and H. Tsunetsugu. Electronic structures of $Sr_{14-x}Ca_xCu_{24}O_{41}$. *Phys. Rev. B*, 56(8):R4305–R4308, Aug 1997.

[127] T. F. A. Müller, V. Anisimov, T. M. Rice, I. Dasgupta, and T. Saha-Dasgupta. Electronic structure of ladder cuprates. *Phys. Rev. B*, 57(20):R12655–R12658, May 1998.

[128] L. Balents and M. P. A. Fisher. Delocalization transition via supersymmetry in one dimension. *Phys. Rev. B*, 56(20):12970–12991, Nov 1997.

[129] D. Controzzi and K. Schoutens. On the quasiparticle descritption of $c = 1$ CFTs. *J. Phys. A.*, 37(14):4289, 2004.

[130] M. Troyer, H. Tsunetsugu, and T. M. Rice. Properties of lightly doped t-J two-leg ladders. *Phys. Rev. B*, 53:251, 1996.

Danksagung

An dieser Stelle möchte ich mich bei allen bedanken, die zu dieser Arbeit beigetragen haben.

Meinen Betreuern Herrn Prof. Dr. Götz S. Uhrig und Herrn Prof. Dr. Alan Tennant gilt mein besonderer Dank für die Vergabe des vorliegenden Themas. Nur durch ihr Engagement ist die Kombination aus theoretischer und experimenteller Arbeit für mich möglich geworden. Der entspannte und freundliche Umgang miteinander war für die Gewinnung von Erkenntnissen sehr fruchtbar.

Desweiteren bedanke ich mich herzlich bei Frau Prof. Dr. Bella Lake und Herrn Dr. Kai P. Schmidt für die vielen konstruktiven und kritschen Gespräche, die mich immer wieder in meiner Arbeit motiviert haben. Herrn Dr. Kai P. Schmidt gilt noch ein besonderer Dank, da er mir seine Programme für die PCUT Rechnungen zur Verfügung gestellt hat.

Generell danke ich der ganzen Arbeitsgruppe für die angenehme Arbeitsatmosphäre.

Ein herzlicher Dank gilt Herrn Dr. Matus Mihalik vom Helmholtz-Zentrum-Berlin für den Austausch von Messdaten, welche mit Merlin gemessen wurden.

Simone Hamerla, Gregor Foltin und Peter Karbach danke ich für die sehr herzliche Stimmung im Büro und die vielen witzigen Momente.

Dr. Stefano Pasini danke ich für die Verbesserung meiner Italienisch-Kenntnisse, für die Mitbenutzung seiner *macchinetta del caffé* und für seine Gesellschaft.

Clare Gibson und Dr. Jonathan Morris danke ich für die freundliche Aufnahme während meiner Aufenthalte am Helmholtz-Zentrum in Berlin. Clare danke ich für den Austausch von Messungen am MAPS-Spektrometer.

Dr. Sebastian Duffe, Nils Drescher, Tim Fischer, Dr. Patrick Grete, Jörn Krones, Dr.

Carsten Raas und Daniel Stanek danke ich für ihre Unterstützung und ihr kollegiales Verhalten.